



HAL
open science

Spintronics memory function: materials and device concepts

Ricardo Sousa

► **To cite this version:**

Ricardo Sousa. Spintronics memory function: materials and device concepts. Mesoscopic Systems and Quantum Hall Effect [cond-mat.mes-hall]. Université Grenoble Alpes, 2017. tel-01673315

HAL Id: tel-01673315

<https://cea.hal.science/tel-01673315>

Submitted on 29 Dec 2017

HAL is a multi-disciplinary open access archive for the deposit and dissemination of scientific research documents, whether they are published or not. The documents may come from teaching and research institutions in France or abroad, or from public or private research centers.

L'archive ouverte pluridisciplinaire **HAL**, est destinée au dépôt et à la diffusion de documents scientifiques de niveau recherche, publiés ou non, émanant des établissements d'enseignement et de recherche français ou étrangers, des laboratoires publics ou privés.

MÉMOIRE

Pour obtenir l'

HABILITATION A DIRIGER DES RECHERCHES

Spécialité : **Nano-électronique et nanotechnologies**

Arrêté ministériel : 23 novembre 1988

Présentée par

Ricardo SOUSA

préparée au sein du **Laboratoire SPINTEC UMR 8191 (CEA/CNRS/Univ. Grenoble Alpes)** au **CEA-Grenoble/INAC**,
dans l'**Ecole Doctorale d'Electronique, Electrotechnique, Automatique et Traitement du Signal (EEATS)**

Spintronics memory function : materials and device concepts

Mémoire soutenu publiquement le **4 Mai 2017**,
devant le jury composé de :

Monsieur, Russell Cowburn

Professeur - University of Cambridge, Rapporteur

Monsieur, François Montaigne

Professeur - Université de Lorraine / IJL, Rapporteur

Monsieur, Dafiné Ravelosona

Directeur de Recherches - CNRS / IEF, Rapporteur

Monsieur, Ahmad Bsiesy

Professeur - UGA / EEATS, Examineur

Monsieur, Christophe Muller

Directeur de Recherches - CNRS, Prof. Aix-Marseille Université, Examineur

Monsieur, Ioan Lucian Prejbeanu

Directeur - SPINTEC / CEA – EEATS, Examineur

Monsieur, Alain Schuhl

Professeur - UGA Ecole Doctorale de Physique, Directeur - CNRS / INP, Invité



Contents

1	Introduction	5
1.1	Préambule	5
1.2	Emerging non-volatile memory	7
1.2.1	Magnetic RAM	8
2	A spintronics memory	10
2.1	Introduction	13
2.2	Magnetic random access memory (MRAM)	13
2.2.1	Spin transfer torque (STT)	13
2.3	Thermally assisted MRAM	15
2.3.1	Heating dynamics	17
2.3.2	Exchange bias thermally activated relaxation	19
2.3.3	Thermal barriers	21
2.3.4	Thermal time constants	22
2.3.5	Temperature and interlayer exchange coupling	24
2.3.6	Spin transfer torque writing	26
2.4	Conclusion	28
3	High speed concepts	29
3.1	Introduction	32
3.2	Field induced precession	32
3.3	Spin transfer torque induced precession	33
3.3.1	Orthogonal spin polarizer	34
3.3.2	STT precessional switching	37
3.3.3	Deterministic switching	40
3.4	Tunnel barrier breakdown	41
3.4.1	Breakdown mechanisms	42
3.4.2	Noise measurement correlation	45
3.5	Conclusion	46
4	Scaling to high density: perpendicular anisotropy	48
4.1	Introduction	50
4.2	Spin transfer torque and perpendicular anisotropy	50
4.2.1	Thermal stability	52
4.2.2	Materials for perpendicular anisotropy	53

4.2.3	Magnetic tunnel junction integration	54
4.2.4	Spin transfer torque switching	58
4.2.5	Field-voltage phase diagrams	59
4.3	Perpendicular anisotropy: thermally assisted writing	60
4.3.1	Thermally induced spin reorientation	61
4.3.2	Perpendicular anisotropy temperature dependence	61
4.3.3	Thermally induced spin reorientation switching	62
4.4	Conclusion	63
5	Perspectives et conclusion	65
5.1	Perspectives	65
5.1.1	Scalabilité et roadmap MRAM	65
5.1.2	Écriture femtoseconde	67
5.1.3	Intégration CMOS et circuits hybrides	68
5.2	Conclusion	69
	Bibliography	70
	Curriculum vitae	80

Chapter 1

Introduction

1.1 Préambule

Mon activité dans le domaine des jonctions tunnel magnétiques a démarrée en 1995 au moment de la découverte de la magnétorésistance tunnel à température ambiante. C'était ma première expérience de recherche dans ce domaine, suite à mes études en Physique Technologique à la Faculté des Sciences de l'Université de Lisbonne au Portugal. En 1997, une bourse de thèse me donne l'opportunité de poursuivre mes études dans le laboratoire Microsystèmes et Nanotechnologies à l'INESC à Lisbonne sous la direction du Professeur Paulo Freitas. Le sujet de ma thèse était l'application des jonctions tunnel magnétiques aux mémoires magnétiques à accès aléatoire (MRAM), de l'anglais Magnetic Random Access Memory. Pendant ma thèse j'ai démontré l'efficacité des recuits thermiques pour augmenter la magnétorésistance tunnel et réalisé les premières cellules intégrées: jonction tunnel et diode en silicium amorphe hydrogéné. Ce moment correspond aussi au début de l'adoption des mémoires non-volatiles type FLASH comme moyen de stockage de données et les MRAM se profilaient comme une technologie émergente alternative plus rapide et endurante. En 2002, je suis arrivé comme Post-Doc boursier Marie Curie, au laboratoire Spintec du CEA-Grenoble/INAC, tout juste crée pour explorer le nouveau domaine de la Spintronique, que j'ai intégré par la suite. A Spintec j'ai participé au développement de cellules MRAM à écriture assistée thermiquement. Ce type de cellule brevetée présentait deux avantages majeurs : une seule direction de champ magnétique était nécessaire pour sélectionner la cellule à écrire dans une matrice, et en même temps une plus grande stabilité des états programmés était obtenue. Nous avons réussi à faire la preuve de ce concept, avec l'intégration de matériaux anti-ferromagnétiques dans la couche de stockage de la jonction tunnel et la maîtrise de la résistivité de la barrière tunnel pour produire une augmentation de température compatible avec le déblocage et la réorientation de l'aimantation. Ce travail été réalisé dans le cadre du projet Européen NEXT, dont la qualité a été reconnue par la sélection comme finaliste du prix Descartes en 2006. Ces résultats et brevets déposés ont contribué à la création de la start-up Crocus Technology cette même année.

Dans le cadre d'un programme commun de collaboration avec Crocus Technology, j'ai codirigé 5 thèses (1 CFR et 4 Cifre) liées pour l'essentiel à des études visant établir et améliorer la technologie d'écriture par assistance thermique. Pour diminuer la puissance nécessaire au chauffage, nous avons étudié le mécanisme de chauffage et ses effets dynamiques sur le déblocage de la couche

de stockage (thèse de Lucien Lombard), ainsi que les contraintes imposées par la géométrie et les matériaux sur l'efficacité de chauffage (thèse d'Erwan Gapihan). Nous avons démontré qu'une réduction de la puissance consommée à l'écriture encore plus importante est possible en combinant l'effet de chauffage du courant à un effet de transfert de spin compatible avec l'écriture assisté thermiquement. Il devient alors possible de commuter la couche de stockage sans aucun champ magnétique (thèse de Jérémy Hérault) ou avec un champ magnétique réduit (thèse d'Antoine Chavent) représentant une réduction de 30% de la puissance nécessaire pour générer le champ. Pendant ces deux thèses nous avons aussi étudié la dynamique du retournement en temps réel et démontré que la stabilité de l'état écrit pendant l'impulsion de chauffage limite la probabilité finale de la commutation. Finalement, et encore dans le cadre de la collaboration avec Crocus Technology, nous avons aussi démontré un concept de cellule mémoire à lecture auto-référencée utilisant le champ dipolaire de la couche de lecture pour écrire la couche de stockage. Pour ce type de mémoire il est possible de réduire la taille latérale des plots à 45nm sans trop augmenter la consommation (thèse de Quentin Stainer). Ce type de cellule permet aussi la réalisation de fonctions logiques type XOR et un stockage multi-bit. Une sélection de ces résultats est présentée dans le chapitre 2, notamment sur les questions liées au chauffage et les méthodes pour déterminer la température à l'intérieur du pilier.

Au cours de différents projets autour des mémoires magnétiques, j'ai aussi eu l'occasion d'aborder la question de la vitesse de commutation de l'aimantation. Cette vitesse ultime est limitée par la fréquence de précession de l'aimantation autour d'un champ magnétique, typiquement quelques GHz, ce qui correspond à un temps d'écriture inférieur à la nanoseconde. A la fin de ma thèse, j'avais réalisé des échantillons pour permettre l'observation ces retournements balistiques par l'application d'une impulsion de champ magnétique en collaboration avec l'Institut d'Electronique Fondamentale (IEF). A Spintec nous avons étudié la possibilité de réaliser des cellules à commutation précessionnelle permettant d'adresser des applications mémoire non-volatile du type cache rapide (thèse de Maria Marins de Castro Souza) sans appliquer de champ magnétique. Ceci devenait possible grâce à l'utilisation d'un courant polarisé en spin perpendiculaire au plan de la couche de stockage. La collaboration avec l'IEF a été renouée pour étudier la commutation en temps réel et démontrer des temps de commutation ultimes proches de 100ps. La solution pour réaliser le retournement précessionnel de façon déterministe a été résolue par l'analyse des conditions nécessaires à la précession et à la stabilité (thèse de Bertrand Lacoste). Ceci a ensuite été démontré expérimentalement en utilisant des formes de plot elliptiques avec des facteurs de forme autour de 4:1. Les conditions pour un retournement précessionnel ou par transfert de spin imposent parfois des tensions élevées appliquées pendant des temps courts et la fiabilité au claquage de la barrière tunnel apparaît comme le facteur limitant. Nous avons étudié les mécanismes de claquage des barrières MgO et démontré une corrélation qualitative entre un niveau de bruit électrique élevé et une fiabilité réduite (thèse de Selma Amara). Le chapitre 3 concerne ces deux sujets, qui sont liés par la nécessité d'appliquer des impulsions courtes mais d'amplitude relativement élevée pour réaliser une commutation précessionnelle.

La réduction des nœuds technologiques impose actuellement à une cellule MRAM d'être stable à des dimensions latérales inférieures à 30nm et de viser à l'avenir un diamètre de 10nm. L'utilisation de cellules à anisotropie perpendiculaire, où l'aimantation est orthogonale à la surface de dépôt s'est imposée comme la solution pour la réalisation de cellules mémoire à diamètre

inférieur à 40nm. J'ai contribué aux études pour réaliser des jonctions tunnel à anisotropie perpendiculaire et leur utilisation dans des cellules mémoire. Ceci a été abordé dans le cadre des projets ANR Ultimate et Excalyb que j'ai aussi coordonnés. D'abord nous avons pu démontrer que l'anisotropie perpendiculaire interfaciale, à l'interface de la barrière tunnel et l'électrode magnétique est particulièrement adaptée à la réalisation de ces cellules (thèse de Lavinia Nistor). Des développements au niveau de l'optimisation des matériaux visant l'augmentation de l'anisotropie et de la magnétorésistance tunnel ont été ensuite réalisés (thèse de Léa Cuchet). En parallèle nous avons démontré qu'une écriture par transfert de spin de cellules à anisotropie perpendiculaire, peut aussi être combinée avec le chauffage de la cellule pour réduire sa stabilité à l'écriture (thèse de Sebastien Bandiera). Tous ces résultats obtenus avec des cellules à anisotropie perpendiculaire sont décrits dans le chapitre 4.

Remerciements

Les travaux présentés dans ce manuscrit sont le fruit des recherches d'un groupe de collègues passionnés. Face au risque d'oublier quelqu'un, je veux remercier collectivement mes co-auteurs et collègues qui se reconnaissent dans ces résultats et tous ceux qui y ont contribué dans leurs fonctions à Spintec, au CEA et à Crocus Technology, je leur témoigne mon immense gratitude. Je remercie en particulier les directeurs de thèse qui m'ont fait confiance pour co-encadrer leurs étudiants: Bernard Diény, Ursula Ebels, Lucian Prejbeanu, Bernard Rodmacq et Alain Schuhl. Pour l'envie de partager leur savoir avec des jeunes chercheurs qui se sont construits tout au long d'une thèse, ou de plusieurs dans mon cas, je leur en suis profondément reconnaissant.

1.2 Emerging non-volatile memory

The 21st century has started with a renewed interest in non volatile memory for data storage. Hard disk drives (HDD), the recent standard for non-volatile data storage, are slowly being displaced from its former central role in personal computing into archival applications in data centers. For data storage, the solid state non volatile FLASH technology is becoming the new standard, from its early debut in mobile devices for music storage, until its recent adoption in desktop computers and even data centers. However there is still a large gap between non-volatile FLASH and volatile DRAM and SRAM memory performance. A number of emerging non volatile memories are aiming at bridging this gap. Some of the most promising ones are resistive memories, for which the bit value is encoded in the cell resistance, using different underlying physical principles [1,2]. This manuscript will cover magnetic random access memories (MRAM), but Phase Change [3] (PCRAM) and Resistive RAM (RRAM) memory, are the two other emerging technologies targeting similar application opportunities [2]. In PCRAM and RRAM cell resistance changes are 3 to 5 orders of magnitude [4], while for MRAM, resistance change is measured in hundreds of %. This is not necessarily a handicap as long as the 1σ resistance dispersion value of the high and low resistance states is only a fraction of the total resistance change, which is typically the case with $\Delta R > 10 - 20\sigma$ [5].

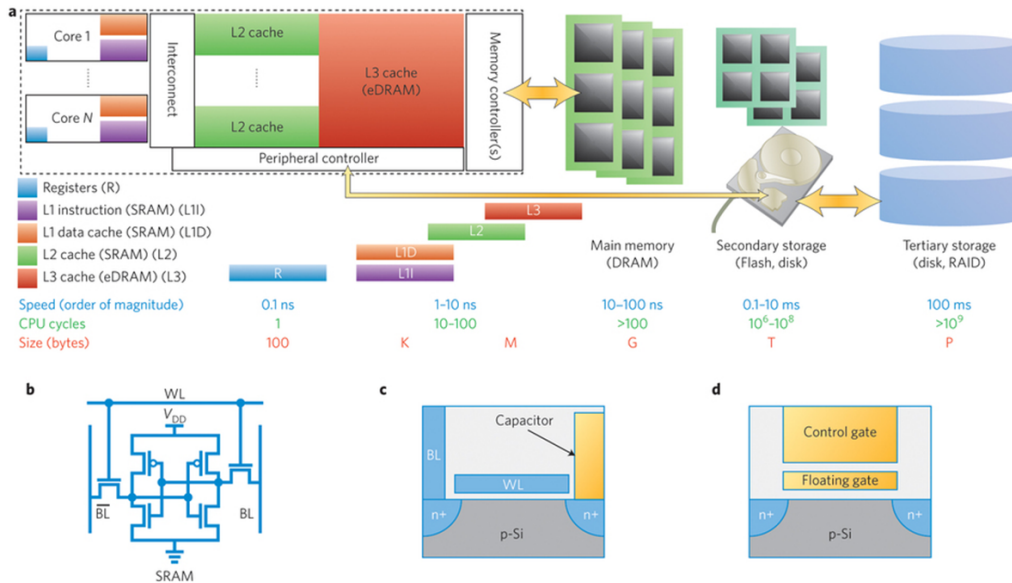


Figure 1.1 – Memory hierarchy and mainstream CMOS memory technologies: SRAM, DRAM and FLASH. [6]

1.2.1 Magnetic RAM

Different magnetic random access memory (MRAM) concepts will be described in this manuscript and their limitations reviewed. As a non-volatile memory seeking adoption the initial step is to bridge the gap between the established CMOS standards of slow/non-volatile FLASH and fast/volatile DRAM/SRAM. Presently, there are several gaps to bridge, but the most important ones are the write access time ($100 - 300\mu s$ vs $1 - 50ns$), number of write cycles (10^5 vs unlimited) and retention (10 years at $55^\circ C$ vs $0-64ms$). As a memory technology, MRAM is often pitched against mainstream memory that are used as standalone memory standards. It is difficult for a new technology to be a direct replacement of a more mature one, since the basic economics are all against the new entrant in terms of investment, learning curve and yield improvement. This is the case for all emerging non-volatile technologies. Perhaps the best opportunity for MRAM as a non-volatile technology is vying to become the standard choice for embedded non-volatile technology.

Embedded MRAM does not seek to replace high density non-volatile memory and, for embedded applications, the cell density and size are less demanding than for standalone memory. There are a number of benefits to use non-volatile memory as MRAM in embedded applications. Presently saving data to external non-volatile memory modules comes with a performance loss, because of the additional input-output communication layers. Using embedded solutions allows for product specific designs, additional performance and security. It also acts as a differentiation element in custom designs. Direct comparison with embedded FLASH, shows that eFLASH requires more additional mask levels (6-8) and integration process complexity, because of special transistors and gate oxides. It is also restricted by high voltage operation and suffers from limited endurance [8]. Finally, since it is not an actual random access memory, it is not really an alternative to eSRAM or eDRAM. In terms of performance embedded MRAM must achieve better than $100ns$ read/write cycles, with application unlimited endurance. It must be compatible with low power

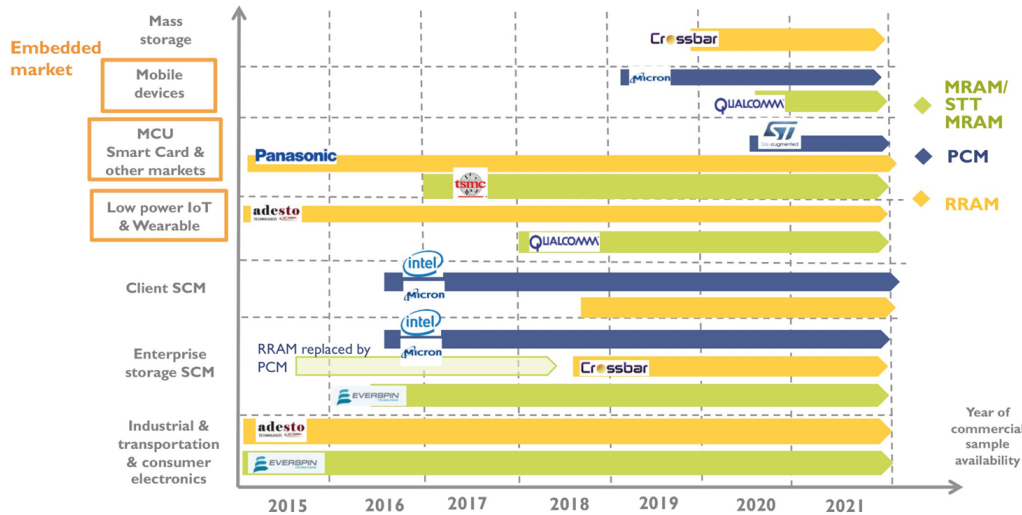


Figure 1.2 – Markets and sample availability for emerging non-volatile memory applications (Source: Yole, July 2016). [7]

logic circuits beyond the 28nm node. Making this breakthrough could be a genuinely disruptive solution with a competitive advantage compared to conventional embedded memories.

This opportunity is confirmed by Everspin’s own statement, presently the sole supplier of MRAM, that half their total unit volume corresponds to embedded applications of non-volatile, fast-write eMRAM memory blocks. Initially their 4Mbit MRAM modules found niche applications as a direct replacement for Flash and battery backed SRAM. The application fields have been expanding to non-volatile data logs and memory software subsystems. These can be frequently updated with no restrictions on the number of data writes in automotive, medical and industrial applications. The same benefits can be used for aerospace and high radiation environment applications since MRAM is tolerant to radiation.

A key advantage for embedded MRAM, is that it can be implemented as a true back-end technology above the final CMOS metal layers. It is also compatible with present CMOS logic while providing versatility across technology nodes. For example, the perpendicular anisotropy MRAM developed for an advanced technology node can be used in more relaxed older nodes of 28, 45 or 65nm. Embedded MRAM can also be used to simplify and increase circuit performance through bit cell design optimization. It also provides for lower cost, in the sense of reducing the number of components required to manage power losses, for example. There are real opportunities for eMRAM to be used as a differentiator because of its unlimited write capability as memory log and upgradable system, all the while presenting no additional static power dissipation. These power saving features could even be extended by the possibility of *instant on/off* capability. As an emerging non-volatile memory technology it has provided a rich environment for the development of different concepts. It has now matured and presently magnetic materials with perpendicular anisotropy represent a path for embedded MRAM [9] down to the 16nm technology node and possibly beyond.

Chapter 2

A spintronics memory

Related Thesis

1. Lucien Lombard, étude de l'extension de la gamme de températures de fonctionnement des Mémoires Magnétiques à Accès Aléatoire Assistées Thermiquement. PhD thesis, Université de Grenoble, 2010.
2. Jérémy Hérault. Mémoire magnétique à écriture par courant polarisé en spin assistée thermiquement. PhD thesis, Université de Grenoble, 2010.
3. Erwan Gapihan, Mémoire magnétique à écriture assistée thermiquement à base de FeMn. PhD thesis, Université de Grenoble, 2010.
4. Antoine Chavent. Réduction du champ d'écriture de mémoires magnétiques à écriture assistée thermiquement à l'aide du couple de transfert de spin. PhD thesis, Université de Grenoble, 2016.

Related Publications

1. S. Bandiera, R. C. Sousa, Y. Dahmane, C. Ducruet, C. Portemont, V. Baltz, S. Auffret, I. L. Prejbeanu, and B. Dieny. Comparison of Synthetic Antiferromagnets and Hard Ferromagnets as Reference Layer in Magnetic Tunnel Junctions With Perpendicular Magnetic Anisotropy. *IEEE Magnetics Letters*, 1:3000204–3000204, 2010.
2. S. Cardoso, R. Ferreira, F. Silva, P. P. Freitas, L. V. Melo, R. C. Sousa, O. Redon, M. MacKenzie, and J. N. Chapman. Double-barrier magnetic tunnel junctions with GeSbTe thermal barriers for improved thermally assisted magnetoresistive random access memory cells. *Journal of Applied Physics*, 99(8):08N901, April 2006.
3. A. Chavent, C. Ducruet, C. Portemont, C. Creuzet, L. Vila, J. Alvarez-Hérault, R. C. Sousa, I. L. Prejbeanu, and B. Dieny. Controlled pulse shape cooling in planar TAS-STT-MRAM for improved writeability. In *2015 IEEE Magnetics Conference (INTERMAG)*, pages 1–1, May 2015.
4. A. Chavent, C. Ducruet, C. Portemont, C. Creuzet, L. Vila, J. Alvarez-Hérault, R. C. Sousa, I. L. Prejbeanu, and B. Dieny. Influence of cooling rate in planar thermally assisted magnetic random access memory: Improved writeability due to spin-transfer-torque influence. *Applied Physics Letters*, 107(11):112403, September 2015.
5. A. Chavent, C. Ducruet, C. Portemont, L. Vila, J. Alvarez-Hérault, R. Sousa, I. L. Prejbeanu, and B. Dieny. Steady State and Dynamics of Joule Heating in Magnetic Tunnel Junctions Observed via the Temperature Dependence of RKKY Coupling. *Physical Review Applied*, 6(3):034003, September 2016.
6. B. Dieny, R. Sousa, S. Bandiera, M. Castro Souza, S. Auffret, B. Rodmacq, J. P. Nozieres, J. Hérault, E. Gapihan, I. L. Prejbeanu, C. Ducruet, C. Portemont, K. Mackay, and B. Cambou. Extended scalability and functionalities of MRAM based on thermally assisted writing. In *2011 International Electron Devices Meeting*, pages 1.3.1–1.3.4, December 2011.
7. B. Dieny, R. Sousa, G. Prenat, and U. Ebels. Spin-dependent phenomena and their implementation in spintronic devices. In *International Symposium on VLSI Technology, Systems and Applications, 2008. VLSI-TSA 2008*, pages 70–71, April 2008.

8. B. Dieny, R.c. Sousa, J. Herault, C. Papusoi, G. Prenat, U. Ebels, D. Houssameddine, B. Rodmacq, S. Auffret, L.d. Buda-Prejbeanu, M.c. Cyrille, B. Delaet, O. Redon, C. Ducruet, J.-P. Nozieres, and I.I. Prejbeanu. Spin-transfer effect and its use in spintronic components. *International Journal of Nanotechnology*, 7(4-8):591–614, January 2010.
9. E. Gapihan, J. Héroult, R. C. Sousa, Y. Dahmane, B. Dieny, L. Vila, I. L. Prejbeanu, C. Ducruet, C. Portemont, K. Mackay, and J. P. Nozières. Heating asymmetry induced by tunneling current flow in magnetic tunnel junctions. *Applied Physics Letters*, 100(20):202410, May 2012.
10. E. Gapihan, R. C. Sousa, J. Herault, C. Papusoi, M. T. Delaye, B. Dieny, I. L. Prejbeanu, C. Ducruet, C. Portemont, K. Mackay, and J. P. Nozieres. FeMn Exchange Biased Storage Layer for Thermally Assisted MRAM. *IEEE Transactions on Magnetism*, 46(6):2486–2488, June 2010.
11. J. Héroult, R. C. Sousa, C. Ducruet, B. Dieny, Y. Conraux, C. Portemont, K. Mackay, I. L. Prejbeanu, B. Delaët, M. C. Cyrille, and O. Redon. Nanosecond magnetic switching of ferromagnet-antiferromagnet bilayers in thermally assisted magnetic random access memory. *Journal of Applied Physics*, 106(1):014505, July 2009.
12. M. Kerekes, R. C. Sousa, I. L. Prejbeanu, O. Redon, U. Ebels, C. Baraduc, B. Dieny, J.-P. Nozières, P. P. Freitas, and P. Xavier. Dynamic heating in submicron size magnetic tunnel junctions with exchange biased storage layer. *Journal of Applied Physics*, 97(10):10P501, May 2005.
13. L. Lombard, E. Gapihan, R. C. Sousa, Y. Dahmane, Y. Conraux, C. Portemont, C. Ducruet, C. Papusoi, I. L. Prejbeanu, J. P. Nozières, B. Dieny, and A. Schuhl. IrMn and FeMn blocking temperature dependence on heating pulse width. *Journal of Applied Physics*, 107(9):09D728, May 2010.
14. C. Papusoi, Y. Conraux, I. L. Prejbeanu, R. Sousa, and B. Dieny. Switching field dependence on heating pulse duration in thermally assisted magnetic random access memories. *Journal of Magnetism and Magnetic Materials*, 321(16):2467–2471, August 2009.
15. C. Papusoi, B. Delaët, B. Rodmacq, D. Houssameddine, J.-P. Michel, U. Ebels, R. C. Sousa, L. Buda-Prejbeanu, and B. Dieny. 100 ps precessional spin-transfer switching of a planar magnetic random access memory cell with perpendicular spin polarizer. *Applied Physics Letters*, 95(7):072506, August 2009.
16. C. Papusoi, R. Sousa, J. Herault, I. L. Prejbeanu, and B. Dieny. Probing fast heating in magnetic tunnel junction structures with exchange bias. *New Journal of Physics*, 10(10):103006, 2008.
17. C. Papusoi, R. C. Sousa, B. Dieny, I. L. Prejbeanu, Y. Conraux, K. Mackay, and J. P. Nozières. Reversing exchange bias in thermally assisted magnetic random access memory cell by electric current heating pulses. *Journal of Applied Physics*, 104(1):013915, July 2008.
18. I. L. Prejbeanu, S. Bandiera, J. Alvarez-Héroult, R. C. Sousa, B. Dieny, and J.-P. Nozières. Thermally assisted MRAMs: ultimate scalability and logic functionalities. *Journal of Physics D: Applied Physics*, 46(7):074002, 2013.
19. I. L. Prejbeanu, M. Kerekes, R. C. Sousa, H. Sibuet, O. Redon, B. Dieny, and J. P. Nozières. Thermally assisted MRAM. *Journal of Physics: Condensed Matter*, 19(16):165218, 2007.
20. I. L. Prejbeanu, W. Kula, K. Ounadjela, R. C. Sousa, O. Redon, B. Dieny, and J. P. Nozieres. Thermally assisted switching in exchange-biased storage layer magnetic tunnel junctions. *IEEE Transactions on Magnetism*, 40(4):2625–2627, July 2004.
21. I. L. Prejbeanu, R. C. Sousa, B. Dieny, J. P. Nozieres, S. Bandiera, and K. Mackay. Magnetic logic functionalities and scalability of thermally assisted MRAMs. In *2013 IEEE Faible Tension Faible Consommation (FTFC)*, pages 1–1, June 2013.
22. I. L. Prejbeanu, R. C. Sousa, B. Dieny, J. P. Nozières, S. Bandiera, J. Alvarez-Héroult, Q. Stainer, L. Lombard, C. Ducruet, Y. Conraux, and K. Mackay. Scalability and logic functionalities of TA-MRAMs. In *New Circuits and Systems Conference (NEWCAS), 2013 IEEE 11th International*, pages 1–4, June 2013.
23. R. C. Sousa, M. Kerekes, I. L. Prejbeanu, O. Redon, B. Dieny, J. P. Nozières, and P. P. Freitas. Crossover in heating regimes of thermally assisted magnetic memories. *Journal of Applied Physics*, 99(8):08N904, April 2006.
24. R. C. Sousa, I. L. Prejbeanu, D. Stanescu, B. Rodmacq, O. Redon, B. Dieny, Jianguo Wang, and P. P. Freitas. Tunneling hot spots and heating in magnetic tunnel junctions. *Journal of Applied Physics*, 95(11):6783–6785, June 2004.
25. Ricardo C. Sousa and I. Lucian Prejbeanu. Non-volatile magnetic random access memories (MRAM). *Comptes Rendus Physique*, 6(9):1013–1021, November 2005.
26. Q. Stainer, L. Lombard, K. Mackay, D. Lee, S. Bandiera, C. Portemont, C. Creuzet, R. C. Sousa, and B. Dieny. Self-referenced multi-bit thermally assisted magnetic random access memories. *Applied Physics Letters*, 105(3):032405, July 2014.

27. Q. Stainer, L. Lombard, K. Mackay, R. C. Sousa, I. L. Prejbeanu, and B. Dieny. MRAM with soft reference layer: In-stack combination of memory and logic functions. In *2013 5th IEEE International Memory Workshop*, pages 84–87, May 2013.

Related Patents

1. R. Sousa, B. Dieny, and O. Redon, "MRAM with high current density," Patent EP1 580 760 (A1), Sep., 2005.
2. B. Dieny, R. Sousa, and D. Stanesco, "Magnetic Tunnel Junction Device and Writing/Reading Method for Said Device," Patent EP1 671 330 (A1) Abstract of corresponding document: FR2 860 910 (A1), Jun., 2006.
3. J.-P. Nozieres, B. Dieny, O. Redon, R. Sousa, and I.-L. Prejbeanu, "Magnetic Memory with a Magnetic Tunnel Junction Written in a Thermally Assisted Manner, and Method for Writing the Same," Patent EP1 719 135 (A1) Abstract of corresponding document: FR2 866 750 (A1), Nov., 2006.
4. I. L. Prejbeanu and R. Sousa, "Magnetic tunnel junction comprising a polarizing layer," Patent EP2 477 227 (A1), Jul., 2012.
5. B. Dieny, J. Moritz, and R. Sousa, "Magnetic Device Having Heat-Assisted Writing," Patent EP2 622 605 (A1) Abstract of corresponding document: WO2 012 042 178 (A1), Aug., 2013.
6. I. L. Prejbeanu and R. Sousa, "MRAM Cell and Method for Writing to the Mram Cell Using a Thermally Assisted Write Operation with a Reduced Field Current," Patent EP2 615 610 (A1), Jul., 2013.
7. B. Dieny and R. Sousa, "Magnetic device with thermally assisted writing," Patent EP2 685 458 (A1), Jan., 2014.

2.1 Introduction

The possibility to use the electron spin as an additional degree of freedom in conventional electronic devices has been referred to as the field of ‘Spintronics’. In that sense, all devices that use magneto-resistance effects to sense a magnetic field such as magnetic sensors or hard disk read heads, can indeed be considered as spintronic devices. A magnetic tunnel junction relying on its tunnel magneto-resistance to code a bit state in the magnetization direction of the free layer is also a spintronic device. However, the initial proposal of MRAM, setting the magnetization direction of the storage layer would happen using two orthogonal magnetic fields to selectively write a single bit in a cell matrix. The discovery that the magnetization direction can be set using the spin polarized electron current [10–12] in an effect referred to as spin transfer torque (STT), represented the breakthrough discovery for a true spintronic memory.

2.2 Magnetic random access memory (MRAM)

In the realizations discussed in this manuscript, a magnetic random access memory element consists of two magnetic electrodes separated by a tunnel barrier, a magnetic tunnel junction. As the unpolarized electron current passes through the reference layer element, transmitted electrons become spin polarized through a torque exerted by the local magnetization. This spin polarization and the magnetization direction of the second electrode modulate the electron tunneling probability, giving rise to the tunnel magneto-resistance (TMR) effect. We find the analog of this effect in optics for light transmission through a polarizer-analyzer setup. In a magnetic tunnel junction, maximum (minimum) tunneling probability and low (high) resistance corresponds to parallel (antiparallel) electrode magnetizations. These two resistance states determine the maximum $TMR = (R_{AP} - R_P)/R_P$ also defined in terms of the electrodes spin polarization $P_{1,2}$ in Jullière’s model [13] as $TMR = 2P_1P_2/(1 - P_1P_2)$. The resistance of the tunnel junction $R(\theta) = R_p + \frac{\Delta R}{2} (1 - \cos \theta)$ provides a read-out of the relative angle θ between the two magnetizations. The memory element resistance change is maximum when the storage layer has stable states that can be either parallel or antiparallel to the reference magnetization direction.

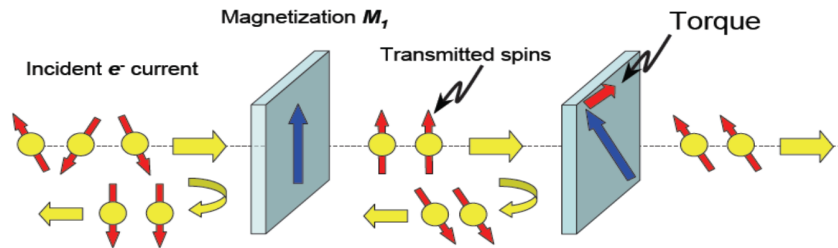


Figure 2.1 – Spin polarization of the electron current by a first magnetic layer and spin torque transfer on the second magnetic layer.

2.2.1 Spin transfer torque (STT)

Spin transfer torque represents the reciprocal effect of spin polarization by the local magnetization. Spin polarized electrons arriving at the second electrode, will again align in the direction

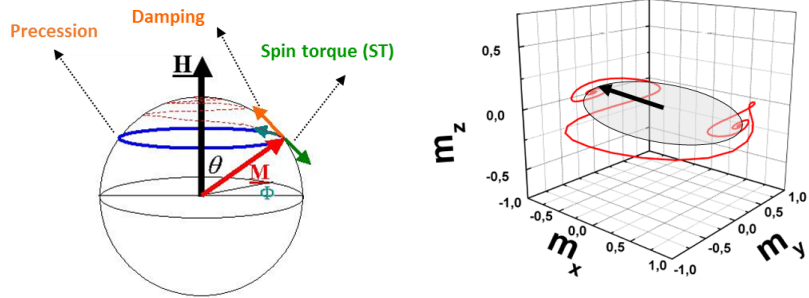
of its magnetization, but in doing so they transfer a torque to the local magnetization. This process can lead to the reversal of the electrode magnetization when the current reaches a critical limit. The reversal of the magnetization is often simplified by a coherent rotation model of a single 'macrospin' element assuming that the local magnetization rotates coherently as single block. The Landau-Lifshitz-Gilbert equation (LLGS) including the Slonczewski spin torque term [10] can then be used to follow the magnetization dynamics $\frac{d\vec{M}}{dt}$

$$\frac{d\vec{M}}{dt} = -\gamma\vec{M} \times \vec{H}_{eff} + \frac{\alpha}{M_s}\vec{M} \times \frac{d\vec{M}}{dt} + \gamma \left[a_{||}\vec{M} \times (\vec{M} \times \vec{P}) + b_{\perp}\vec{M} \times \vec{P} \right] \quad (2.1)$$

$$\vec{H}_{eff} = \vec{H} + \vec{H}_{dem} + \vec{H}_k \quad (2.2)$$

$$a_{||} = \frac{\hbar}{2e} \frac{\eta I}{M_s^2} \quad (2.3)$$

γ is the gyromagnetic ratio, M_s is the saturation magnetization, \vec{M} and \vec{P} magnetization and electron spin polarization vectors. The effective field \vec{H}_{eff} corresponds to the sum of the anisotropy field H_k , the applied field H including dipolar coupling from the reference layer and the \vec{H}_{dem} demagnetizing field. The torques acting on the magnetization result from this effective field, a phenomenological Gilbert damping torque and two spin transfer torque terms: called 'damping like' for the $a_{||}$ pre-factor and 'field like' for the b_{\perp} pre-factor. These first three terms are illustrated in Fig. 2.2(a), the first one describes a precession of the magnetization around the \vec{H}_{eff} direction, the Gilbert term dampens the precession amplitude forcing the alinement of the magnetization along the \vec{H}_{eff} direction. The effect of the spin torque $a_{||}$ 'damping like' term depends on the sign of the spin polarization current. For reversal by spin torque, this term opposes the Gilbert damping, amplifying the magnetization precession amplitude. Analysis of the in-plane geometry neglecting the 'field like' term $b_{\perp} = 0$, shows that the critical current density for magnetization precession amplification and reversal can be calculated as [14]



(a) Torques acting on the magnetization and (b) Magnetization reversal by spin transfer torque for in-plane anisotropy magnetization.

$$j_c^{in-plane} = \frac{2e}{\hbar} \frac{\alpha}{\eta} \mu_0 M_s t \left(\frac{M_s}{2} + H_k + H \right) \quad (2.4)$$

$$j_c^{in-plane} \approx \frac{e}{\hbar} \frac{\alpha}{\eta} \mu_0 M_s^2 t \quad (2.5)$$

since for the in-plane geometry the demagnetizing field value $\mu_0 M_s$ is typically $> 1.4 T$, i.e.

much higher than the the in-plane anisotropy field $\mu_0 H_k$, we can see that the critical current is mainly dominated by the demagnetizing field itself, as seen from equation 2.5. As a consequence, the thermal stability of in-plane cells is disconnected from the STT critical current. For in-plane cells, shape anisotropy defines the anisotropy field in terms of the demagnetizing factors $n_{x,y}$ which can be approximated [15] as the ratio of thickness t to width w and length l :

$$\mu_0 H_k = \mu_0 M_s \frac{t}{w} (n_y - n_x) \approx \mu_0 M_s \frac{t}{w} \left(1 - \frac{w}{l}\right) \quad (2.6)$$

$$(2.7)$$

The estimated anisotropy value for an aspect ratio of 3 and 50nm short axis and $t = 2.5nm$ will be 533Oe, but at these dimensions it will represent less than 5% of the demagnetizing field value, even for aspect ratios up to 10. The energy barrier due to shape anisotropy is $E_b = K_{eff}V = \frac{\mu_0 H_k M_s}{2} V$. For a single bit, the value of the barrier height required to retain the magnetization direction, i.e. stored information, during time t_m is $\frac{E_b}{k_B T} = \log\left(\frac{t_m}{\tau_0}\right)$. For 10 year retention and a single bit the requires ratio is $\frac{E_b}{k_B T} = \log(3.154 \cdot 10^8 / 1 \cdot 10^{-9}) \approx 40$. Not considering any error code correction, assuming N bits while requiring a given bit error rate BER , the energy barrier requirement increases to $\frac{E_b}{k_B T} = \log\left(\frac{N}{BER} \frac{t_m}{\tau_0}\right)$ [16]. Therefore, the thermal stability will significantly increase just by increasing the memory block size or choosing more stringent bit error rate conditions.

2.3 Thermally assisted MRAM

Initial work at Spintec concentrated on the demonstration of a thermally assisted MRAM concept, first using magnetic field and then using spin transfer torque to reverse the magnetization. This chapter focus on some aspects of this effort, briefly reviewing the concept demonstrations and focusing on the characterization of the cell temperature and its dynamics upon heating. Two PhD thesis involving the development of anti-ferromagnetic materials¹ and temperature effects² focussed on field written thermally assisted MRAM, then using spin transfer torque alone³ and finally optimizing the cell for combined field and STT switching⁴.

Thermally assisted switching (TAS-MRAM) was patented and developed at Spintec to solve some of the issues of initial MRAM concepts using field switching to write the bit state. The initial Stoner–Wohlfarth field switching approach proved too sensitive to deviations from the nominal cell geometry and reproducibility of the micro-magnetic switching so that write field windows over a large bit matrix were narrow or non-existing. This issue was solved by a ‘toggle’ switching proposed by Savtchenko [5, 17], but writing still involved a sequence of fields generated by two separated field lines to rotate the magnetization of a synthetic ferrimagnet.

For the proposed thermally assisted MRAM [18] cell approach, the tunnel junction stack was

¹Erwan Gapihan, Mémoire magnétique à écriture assistée thermiquement à base de FeMn. PhD thesis, Université de Grenoble, 2010.

²Lucien Lombard, étude de l’extension de la gamme de températures de fonctionnement des Mémoires Magnétiques à Accès Aléatoire Assistées Thermiquement. PhD thesis, Université de Grenoble, 2010.

³Jérémy Hérault. Mémoire magnétique à écriture par courant polarisé en spin assistée thermiquement. PhD thesis, Université de Grenoble, 2010.

⁴Antoine Chavent. Réduction du champ d’écriture de mémoires magnétiques à écriture assistée thermiquement à l’aide du couple de transfert de spin. PhD thesis, Université de Grenoble, 2016.

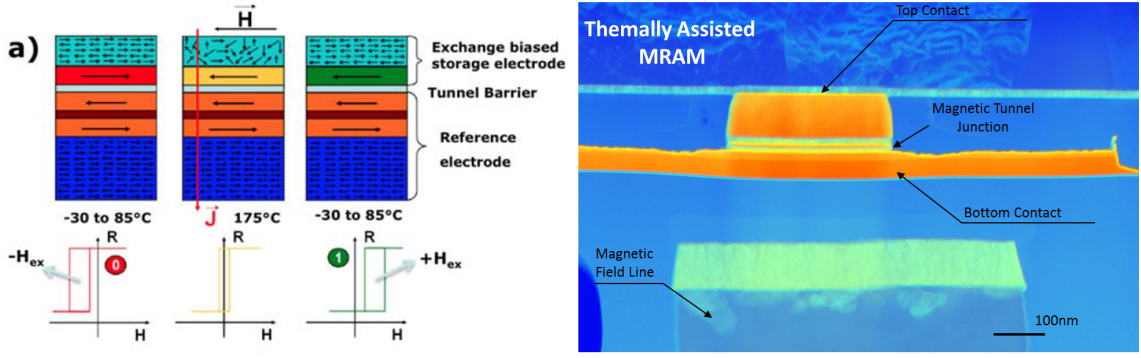


Figure 2.2 – (a) Thermally assisted writing with in-plane exchange biased storage layer. (b) Cross section of thermally assisted MRAM cell.

modified using coupling between an antiferromagnet (AF) and a ferromagnetic (FM) layer to fix the storage layer magnetization direction in the operating temperature window. The write procedure involves heating the junction above the storage layer blocking temperature and cooling down under magnetic field generated by a single field line. The reference and the storage layer were exchange biased by antiferromagnets having very different blocking temperatures T_b . The reference layer used $PtMn$ with $T_b = 350^\circ\text{C}$, while for storage layer $IrMn$ and $FeMn$ were used, with blocking temperatures around 210°C and 140°C .

This presented advantages over other field written cells, in that the write selectivity relies on the selected cell being heated by the cell current flow eliminating addressing errors. Another advantage was that the exchange bias anisotropy of the storage layer defines the thermal stability and data retention. It is then determined by the exchange bias energy from the exchange constant J_{eb} and storage layer magnetization, and not only by the shape anisotropy as for other in-plane cell geometries. This approach provides significant improvements on bit thermal stability, write selectivity and power consumption related to the field generation in MRAM. The energy barrier of thermally assisted MRAM is defined by the shape anisotropy and the exchange bias on the storage layer as

$$E_b \approx 2\pi M_s^2 \left(\frac{l}{w} - 1 \right) \left(\frac{t}{l} \right) + \frac{J_{eb} M_s^2}{t} \left(1 - \frac{T}{T_b} \right) \quad (2.8)$$

where T_b is the blocking temperature of the antiferromagnet pinning the storage layer. This equation shows the gain in thermal stability of thermally assisted MRAM cell at room temperature, since there is now an additional exchange bias term, that only vanishes close to the blocking temperature. As opposed to other field written cells, it becomes possible to disconnect the write field, defined by shape anisotropy, from the thermal stability and have switching fields as low as $20Oe$ [19], that would otherwise result in unstable cells. Cell scaling to smaller dimensions is not limited by shape anisotropy, rather by the possibility to exchange bias small nanomagnets, which will itself be limited by the number and size of antiferromagnetic grains in a single element [20,21].

Initial demonstrations of this concept were realized using $IrMn$ exchange bias and a typical cell stack similar to that described in Fig. 2.3(a). This figure clearly demonstrates the thermally

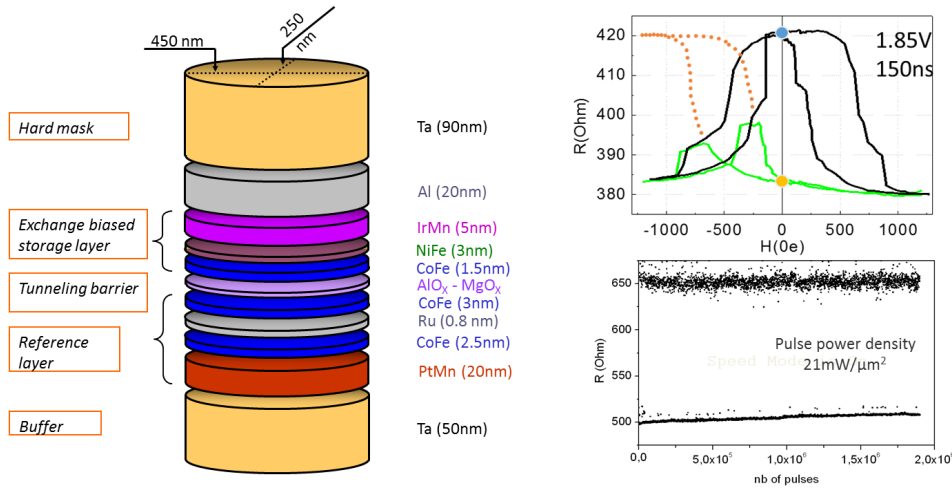


Figure 2.3 – Typical thermally assisted MRAM stack having a reference layer exchange biased by *PtMn* and storage layer with *IrMn* as exchange bias layer. Quasi-static hysteresis loops measured on a junction after setting the storage layer pinning direction by applying a voltage pulse. Demonstration of write pulse repeatability in thermally assisted MRAM.

assisted MRAM cell operation using pulses of 150ns . The hysteresis loops obtained after applying 1.85V pulses for heating, corresponding to a heating power density of $96\text{mW}/\mu\text{m}^2$, and a temperature increase of 160°C from static measurements. The field direction is reversed by a $\pm 200\text{Oe}$ field from one pulse to next, resulting in reversed storage layer pinning direction, which is parallel or antiparallel to the reference layer magnetization direction. In the first case we obtain a low resistance state at zero applied field, while in the second case a high resistance state is measured. Repeated measurements up to 10^6 applied pulses show the reproducibility of the writing and pinning process, the high resistance state revealing a slightly higher dispersion of the final set state [22].

2.3.1 Heating dynamics

After this initial demonstration, we investigated ways to characterize the heating dynamics and the various factors associated with the heating efficiency. Initial observations of heating due to current conduction in a tunnel junction had already been realized using liquid crystal film as a temperature sensor [23] during a study of tunnel barrier breakdown. Localized heating was observed at the breakdown sites of the tunnel junction, but the temperature increase was only a few degrees.

The demonstration of writing an exchange biased storage layer from the temperature increase by the current flow through the tunnel junction to unblock its direction, showed that the direct heating process can be efficient [18, 24]. It also meant that for a short period of time heating up to hundreds of degrees was taking place inside the tunnel junction. Lets first look at the heat diffusion equation which in the 1D case can be written as

$$c_p \rho_m \frac{dT}{dt} - \left[k \frac{d^2T}{dx^2} \right] = \frac{Q}{dt} \quad (2.9)$$

where the variables have the following correspondence: c_p specific heat capacity, ρ_m mass

density, T temperature, t time, k thermal conductivity, x stack position and $\frac{Q}{dt}$ the total heat dissipated per unit of time. In the present case of tunnel junctions the Joule heating contribution from the electrical resistivity can be neglected compared to the dominant contribution from the energy loss by the tunneling electrons. Using the electrical power we can write $\frac{Q}{dt} = V * I = P$, which can be also expressed as a surface power density in terms of the tunnel junction resistance area product ($R \times A$) and the current density j . Assuming the simple case of a uniform material in a 1D geometry with cross section A equation 2.9 can be written as

$$c_p \rho_m \frac{dT}{dt} - k \frac{dT}{dx} = \frac{P}{A} = R \times A j^2 \quad (2.10)$$

The steady state solution is obtained for $\frac{dT}{dt} = 0$ and defines the equilibrium temperature rise as $\Delta T = \frac{P L}{k}$, L being the thickness of the layer considered. The other limit case is that of the initial temperature rise, when $\frac{dT}{dx} = 0$, the slope of the temperature rise is then given by $\frac{dT}{dt} = \frac{P}{A} \frac{1}{c_p \rho_m}$. For the cooling phase, when the power is zero, the temperature evolution can be determined from $(T_i - T_0)$, while the temperature rise to reach the steady state temperature T_f from T_0 can be written as follows

$$T(t) = (T_i - T_0) \exp \left[-t \frac{k}{c_p \rho_m L} \right] + T_0 \quad (\text{cooling}) \quad (2.11)$$

$$T(t) = (T_f - T_0) \left[1 - \exp \left(-t \frac{k}{c_p \rho_m L} \right) \right] + T_0 \quad (\text{heating}) \quad (2.12)$$

Since generally the system is complex and cannot be defined analytically directly from the material parameters, we can write a more general form of the heating equation grouping the material parameters in a thermal time constant τ , keeping the same exponential temperature rise/decay:

$$T(t) = (T_f - T_0) \left[1 - \exp \left(-\frac{t}{\tau} \right) \right] + T_0 \quad (2.13)$$

Since the power density in the tunnel junction is $\frac{P}{A} = R \times A j^2$, where $R \times A$ is the tunnel junction resistance area product and j^2 the current density, the temperature increase can be defined in terms of a proportionality constant a_T in $K/(mW \mu m^{-2})$ such that $(T_f - T_0) = P/A a_T$. This simple 1D case can be used to gain a physical understanding of the underlying heating dynamics however, accurate simulations of the temperature rise in a given system need to rely on numerical solutions of the heat diffusion equation using finite element solvers [25].

Simulations of the full tunnel junction stack in a 3D geometry were carried out using the finite element FEMLAB solver, as shown in Fig. 2.4. For the simulation it was assumed that there is no sidewall heat diffusion. The geometry and the dimensions used were a top Al lead of $9 \mu m$ length, $6 \mu m$ width and $0.3 \mu m$ thick. The bottom lead had shorter width $3 \mu m$, a thickness of $0.15 \mu m$ and both leads are thermalized at the sidewalls and wafer surface for the bottom lead. Material parameters used for the simulations are shown in table 2.1 at the end of this section. The power density dependence on the applied pulse width was measured and is shown Fig. 2.4, using as a threshold an exchange field of zero, obtained from an initialized state under a reverse

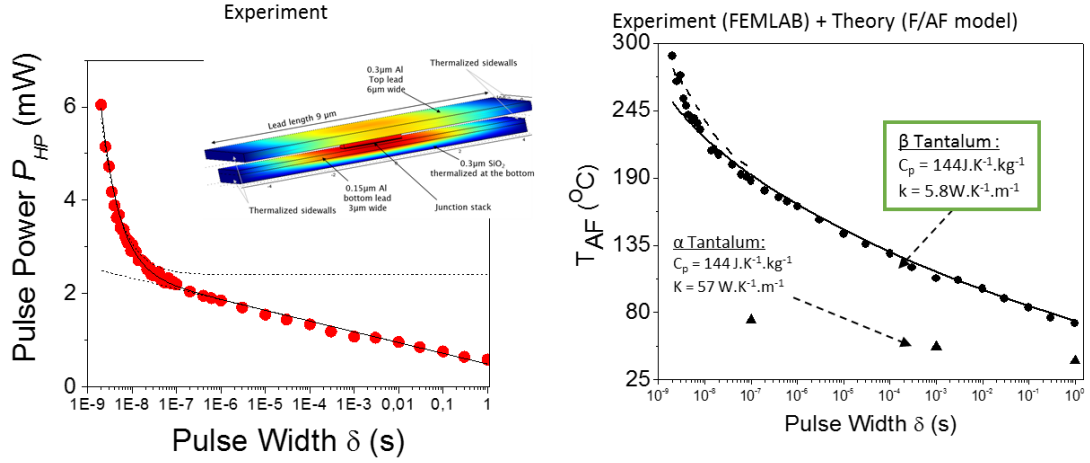


Figure 2.4 – (a) Experimental measurement of heating power density as function of pulse width. FEMLAB simulation geometry in inset. (b) Calculation of temperature increase using experimental power density as input in simulation.

magnetic field. This corresponds to the typical conditions of blocking temperature measurements. The blocking temperature was then calculated using the FEMLAB to solve the heat diffusion equation including the device geometry and all the stack layers. This approach assumed that the experimental power of the heating pulse was converted into heat in the tunnel barrier, allowing a direct input of the heat source term in the heat diffusion equation. The simulation shows the impact of the value of thermal conductivity for Ta in the structure. The $\beta - Ta$ has a thermal conductivity of $5.7 W(mK)^{-1}$, which is 10 times lower than the $\alpha - Ta$ phase. The low thermal conductivity $\beta - Ta$ layers at the bottom and top of the junction contribute to the retention of heat. The tetragonal $\beta - Ta$ was confirmed by X-ray diffraction data and also by the high electrical resistivity of $170 \mu\Omega cm$.

2.3.2 Exchange bias thermally activated relaxation

A clear increase of the pulse power density is observed for the exchange bias to become zero upon heating, that is linear with the logarithm of the pulse width. This points to a Néel-Brown [26] model of thermal relaxation that resembles an Arrhenius thermal activation law [27]. We can write that switching during time t is defined by an energy barrier and an attempt frequency $1/\tau_0$, such that

$$t = \tau_0 \exp\left(\frac{E_b}{k_B T}\right) \quad (2.14)$$

In the present case the barrier is reduced upon heating, since there is a threshold temperature T for writing, and using the equivalence between temperature and power density P we can write that the barrier is reduced as

$$t = \tau_0 \exp\left[\frac{E_b}{k_B T} \left(1 - \frac{P}{P_0}\right)\right] \quad (2.15)$$

By setting the attempt time $\tau_0 = 1 ns$ the power density P_0 will be the density, or equivalently

temperature, required to write within 1ns. It then follows that the the write power density as function of time can be written as

$$P(t) = P_0 \left[1 - \frac{k_B T}{E_b} \ln \left(\frac{t}{\tau_0} \right) \right] \quad (2.16)$$

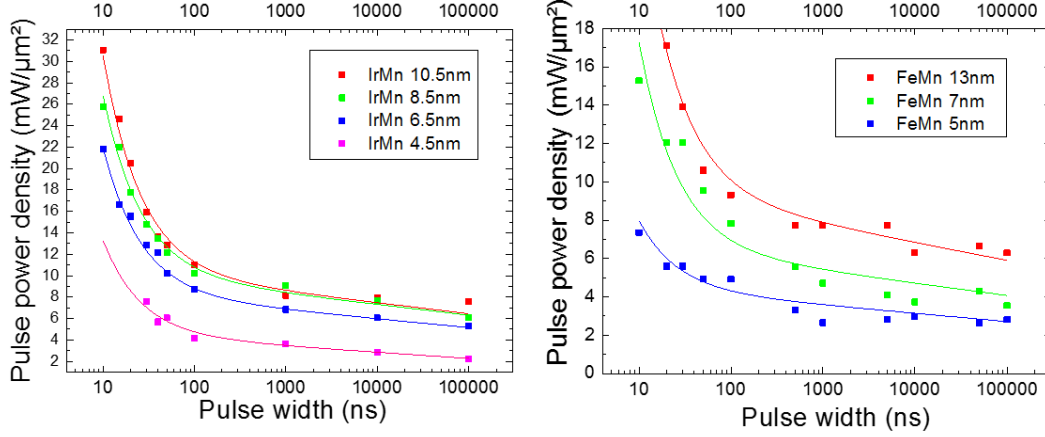


Figure 2.5 – Write power density for *IrMn* (a) and *FeMn* (b) exchange biased *CoFe2nm/NiFe3nm* layers vs the applied heating pulse width. The solid lines are fits with equation 2.18.

To illustrate the write power density dependence on pulse width, we compare data obtained for two antiferromagnets, $Ir_{20}Mn_{80}$ and $Fe_{50}Mn_{50}$ in Fig. 2.5 [28]. The power density shows a linear increase when plotted versus pulse width in a log scale, as is expected from equation 2.16. In the time region, from 100ns to DC, the system has time to reach the steady state temperature and we can use the switching threshold of the exchange bias layer to calculate the temperature rise in the system from the current flow through the junction. It is possible to use the *powerdensity – temperature* equivalence at long time scales, to then estimate the temperature rise in the junction at shorter pulse widths, the antiferromagnetic layer essentially used as a local thermometer. This was realized using a sample heating stage to determine temperature:powerdensity ratio for *IrMn* samples, $23 K/(mW/\mu m^2)$, and $15 K/(mW/\mu m^2)$ in the case of *FeMn* samples. These conversion factors depend on the actual layer stack and geometry, and in the case of *IrMn* included thermal barrier layers for heat confinement. Below 100ns there is a strong increase of the power density required to relax the exchange bias direction. The temperature rise calculated from equation 2.13, shows that the thermal time constant τ_{therm} limits the temperature rise at short pulse widths. We can determine the power density $P(t)$ necessary to reach the same final temperature T_f corresponding to a steady state power density P_f as t approaches zero. We can then write

$$P(t) = P_f \left[1 - \exp \left(-\frac{t}{\tau_{therm}} \right) \right]^{-1} \approx P_f \frac{\tau_{therm}}{t} \quad (2.17)$$

noting in the approximation that $\lim_{t \rightarrow 0} 1 - \exp \left(-\frac{t}{\tau_{therm}} \right) = \frac{t}{\tau_{therm}}$. Therefore in the initial non-equilibrium transitional regime there is an additional factor $\frac{\tau_{therm}}{t}$ increasing the required power

density. This simply states that to provide the same energy to the system in a shorter time t , the required power density increases as $1/t$. This is equivalent to what is commonly referred to as the ‘precessional regime’ [29] in spin transfer torque driven magnetization reversal, where the same amount of torque has to be provided by a constant number of charges in a shorter time, therefore increasing the critical current density as $1/t$ [30]. We can now write the full expression used to fit data in Fig. 2.5 in both steady state thermally activated and non-equilibrium regimes as

$$P(t) \approx P_0 \left(1 + \frac{\tau_{therm}}{t}\right) \left[1 - \frac{k_B T}{E_b} \ln\left(\frac{t}{\tau_0}\right)\right] \quad (2.18)$$

The energy barrier of the exchange bias relaxation and the system thermal time constant can be estimated by fitting the data. In this discussion, we only considered the thermal point of view, but the applied field also plays a role when setting the magnetization direction with a magnetic field during the pulse. In that case the energy barrier in equation 2.15 is modified by a magnetic field related term $\left(1 - \frac{H}{H_k}\right)^n$, where $n \in [1, 2]$ defines the magnetization reversal mode. Therefore, in writing experiments the increase in power will also be defined by the dynamic coercivity of the ferromagnetic layer [31] coupled to the antiferromagnetic grains. The dynamic coercivity contribution will vanish once the Néel temperature of the antiferromagnetic material is reached. Another word of caution is not to convert the power density in the non-equilibrium regime to a calculated temperature using the same conversion factor of the steady state regime. This calculation would lead to temperatures of $400 - 600^\circ\text{C}$ that are in fact never attained, since at short pulse widths the system has no time to reach steady state.

Table 2.1 – Material parameters used in finite element thermal simulations.

Material	Resistivity [$\mu\Omega$ cm]	Therm. Cond. [W (m K) $^{-1}$]	Density [g cm $^{-3}$]	Heat Cap. [J (kg K) $^{-1}$]
α -Ta	13.1	5.8	16.6	144
β -Ta	154	58	16.6	144
Cu	2.7	401	8.96	384
Al	3.7	237	2.7	897
Co	5.8	100	8.9	421
Ru	7.4	117	12.1	238
AlO $_x$	-	37	3.9	794
MgO $_x$	-	7	3.6	1466
SiO $_2$	-	1.4	2.2	733
Ni $_{80}$ Fe $_{20}$	18	88	8.7	401
Co $_{80}$ Fe $_{20}$	12.4	82	7.9	446
Ir $_{20}$ Mn $_{80}$	147	35.6	10.3	409
Pt $_{30}$ Mn $_{70}$	147	26.9	11.6	375

2.3.3 Thermal barriers

The results from using different antiferromagnets showed that it is possible to reduce the write power density using a lower blocking temperature material like *FeMn*. It also has the additional benefit of having a lower Néel temperature, which limits the power density increase in the non-equilibrium short pulse limit. A second possibility to optimize the heating efficiency of the cell is to insert a low thermal conductivity material in the cell stack to confine the heat to the junction volume. This would ideally be coupled to the use of low thermal conductivity insulators to

prevent lateral heat loss. This idea was patented and tested in our cells. The choice was to use a chalcogenide phase change material $Ge_{20}Sb_{24}Te_{56}$ (GST) that combines a thermal conductivity below $1.5W/m/K$ [32], while being electrically conducting in its crystalline phase, typically adding $3 - 5\Omega\mu^2$ to the junction. Incorporating $20nm$ GST did not affect surface roughness $0.3nm$ below the tunnel barrier.

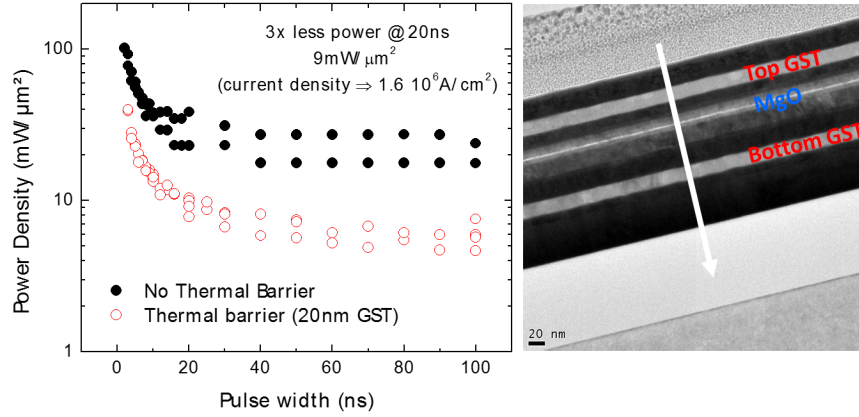


Figure 2.6 – Write power density dependence on pulse width in steady state and non-equilibrium ranges obtained for thermally assisted MRAM cells with and without GeSbTe thermal barriers.

Samples with and without thermal barriers were compared for pulse writing, clearly showing the higher heating efficiency of stacks having a thermal barrier as is reflected by the reduction of write power density by up to a factor of 3 as seen in Fig. 2.6 [33]. For pulse widths of $15 - 20ns$ the write power density was below $10mW/\mu m^2$ corresponding to a current density of $1.6 \cdot 10^6 A/cm^2$. The higher heating efficiency comes at the cost of increasing the thermal time constant of the system, as seen from equation 2.12, since the thermal time constant is directly proportional to the thermal conductivity k . This is observed in our data, since the power density increase associated with the non-equilibrium regime starts around $60ns$ instead of $30ns$ for samples without thermal barriers.

2.3.4 Thermal time constants

A procedure to determine the thermal time constant of the system was also developed, using the temperature cooling at the end of the applied pulse. The cooling dynamics was investigated by a procedure involving the application of a two-pulse sequence [34]. The first pulse of constant amplitude and width is used to pre-heat the junction, while a second pulse of width t_2 and variable amplitude is applied at different time delays t_d . The second pulse is used to probe the heating of the junction due to the first pulse and to determine, the temperature to which the junction has cooled to, at a time equal to t_d . The experiment can be more easily understood from Fig. 2.7.

To illustrate the measurement procedure we assume that the cooling process is described by an exponential temperature decay with $T(t) = T_0 + \Delta T (\exp[-t/\tau])$, where τ is the characteristic thermal time constant. The temperature rise is assumed to have the same characteristic time τ , leading to a temperature rise $T(t) = T_0 + \Delta T (1 - \exp[-t/\tau])$. In the time interval where the cooling of the first pulse and the heating of the second pulse takes place, the temperature $T(t)$ can

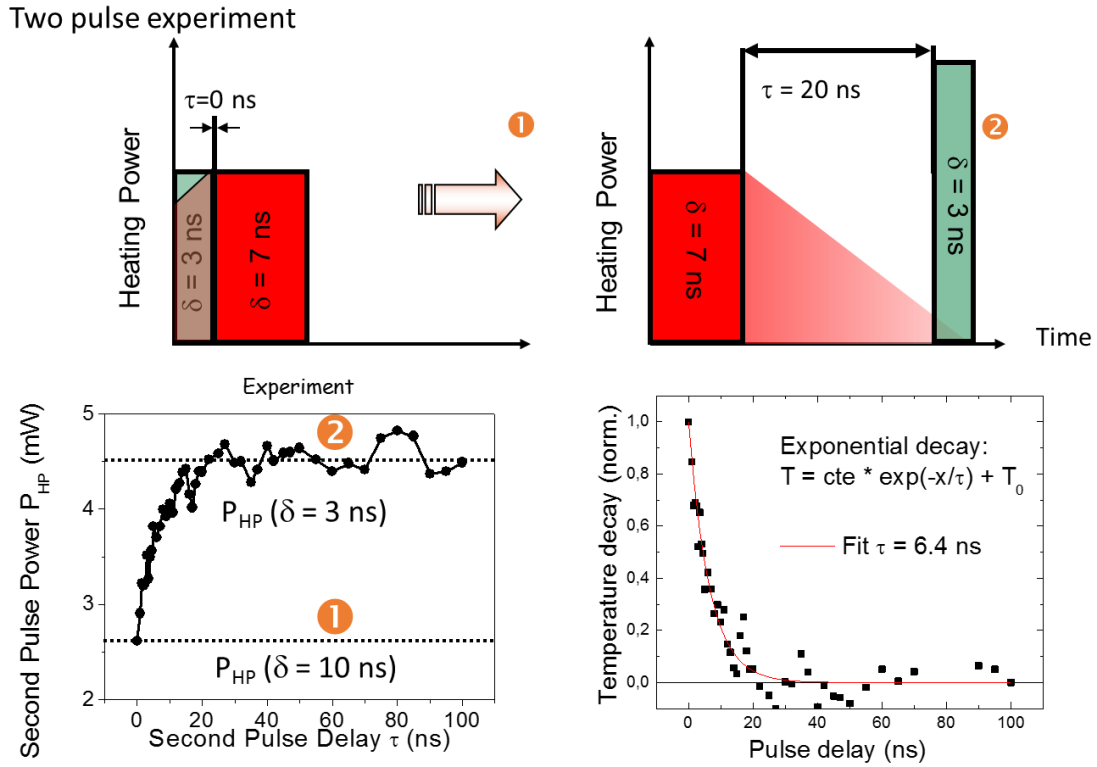


Figure 2.7 – Determining the system thermal time constant τ_{therm} with a two pulse experiment using a time delay to compare power density levels of consecutive and isolated pulses. The power density evolution is normalized and fitted to a temperature decay model to determine τ_{therm} .

be calculated as:

$$\begin{aligned}
 T(t) &= T_1(t) \exp[-t/\tau] + \Delta T_2 (1 - \exp[-(t - t_2)/\tau]) + T_0 \\
 T_1(t) &= \Delta T_1 (1 - \exp[-t_1/\tau])
 \end{aligned}
 \tag{2.19}$$

where t_1 is the time at which the first heating pulse is terminated and t_2 the start of the second heating pulse, while T_1 is the temperature at the end of pulse 1. Equation 2.19 states that the final temperature T is equal to the temperature rise of the second pulse plus the the temperature to which the system would have cooled down to, at $t = t_2 + \delta + t_w$, where δ is a waiting time and t_w the second pulse width. By increasing the waiting time δ and adjusting the power of the second pulse, i.e. the temperature rise ΔT_2 , to reach the same blocking temperature it is possible to access the time evolution of $T_1 \exp[-t/\tau]$ and therefore the characteristic time τ . A first heating pulse of $7ns$ followed by a second heating pulse of $3ns$ were used. The amplitude of the second pulse will vary between two limits. The lower limit is equal to the pulse amplitude necessary to switch with a pulse of $10ns$. In this case there is no cooling after the first pulse and the temperature at the end of the two pulse sequence calculated from equation 2.19 is equivalent to the temperature rise from a $10ns$ pulse of the same amplitude. The upper limit is the case where the system has completely cooled down from the initial temperature rise of the $7ns$ pulse. The $3ns$ pulse will require the same amplitude as when applied isolated. The heating experiments were performed at short pulse

widths to prevent heating of the current leads. The power P_δ applied during the second pulse for a waiting time δ can be plotted using a normalized power value $P = (P_3 - P_\delta)/(P_3 - P_{10})$. In this case the power of the second pulse varies between the two power limits P_{10} and P_3 , corresponding to a single isolated $3ns$ pulse, when the waiting time is long enough for the system temperature to decrease to the room temperature. The data fitted to $P = \exp[-\delta/\tau]$ shows a characteristic time $\tau = 6.4ns$. This means that at a time of $20ns \approx 3 \tau$ the second pulse can be considered as independent of the first one.

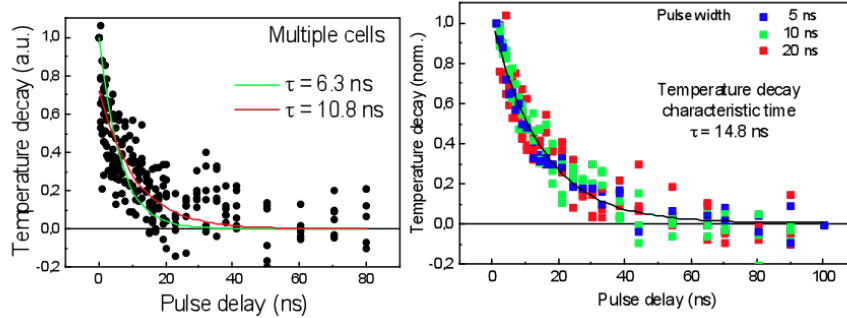


Figure 2.8 – Thermal time constants from temperature decay with and without thermal barriers.

The cooling of samples with thermal barriers was also measured in a similar two pulse temperature decay experiment. A sequence of 20 pulses was applied with varying cooling delays. The high number of pulses was used to increase averaging and statistical significance. At the same time the experiment was realized applying 5, 10 and $20ns$ pulse widths. The normalized temperature evolution is plotted in Fig. 2.8, showing that the measured cooling is in fact independent of the actual pulse width and depends only on the delay between heating pulses. Fitting the temperature decay, we determine a thermal time constant $\tau = 14.8ns$. Measurements on multiple cells without thermal barriers show a value range of $\tau = 5 - 11ns$, corresponding to a speed gain factor 2 – 3 over thermal barrier systems. The cell geometry and the stack can be optimized to balance the gain of lower heating power density versus the slower heating/cooling dynamics. The main advantage of using a thermal barrier is the design possibility it opens, in terms of adjusting the write power density requirement to a given transistor length. The transistor size determines the maximum available write current, which together with the supply voltage and junction area limits the maximum available power density for the cell design.

2.3.5 Temperature and interlayer exchange coupling

The method of determining the temperature through the exchange bias coupling of the anti-ferromagnetic layer is limited to magnetic stacks including some antiferromagnet. This is very common for in-plane anisotropy stacks, but not so for perpendicular anisotropy stacks. A more general way to determine the local cell temperature could use the temperature dependence of interlayer exchange coupling between two ferromagnetic layers through a non-magnetic spacer. It is generally referred to as RKKY coupling and the temperature dependence of the RKKY coupling was described by Bruno [35] as:

$$J_{rkkY}(T) = J_{rkkY}(0) \frac{T/T_b}{\sinh(T/T_b)} \quad (2.20)$$

which is an almost linear temperature dependence in a range from T_0 to $2T_0$, corresponding to intermediate values of $J_{rkkY} \approx 0.85 - 0.55 J_{rkkY}(0)$. Extrapolating this linear region defines a vanishing RKKY coupling at $3.5T_0$. Depending on the spacer thickness the coupling constant J_{rkkY} can be positive or negative, and for this latter case the system energy is lower when the two magnetizations are aligned in anti-parallel direction in a so called synthetic anti-ferromagnetic (SAF) structure [36]. From the analysis of the system energy two characteristic instability points appear at the spin-flop H_{sf} and saturation H_{sat} fields:

$$H_{sf} = \pm \frac{J_{rkkY}|M_1 - M_2|}{\mu_0 M_1 M_2} \quad H_{sat} = \pm \frac{J_{rkkY}(M_1 + M_2)}{\mu_0 M_1 M_2} \quad (2.21)$$

One possible SAF hysteresis cycle showing spin-flop and saturation fields of a in-plane anisotropy structure is shown in Fig. 2.9(a). By choosing the magnetic layer with higher moment, away from the tunnel barrier, it is possible to obtain a high magnetization rotation angle going through the spin flop field. Quasi-static hysteresis loop measurements at increasing bias voltage V can then be correlated to hysteresis loops at increasing substrate temperature. The correlation between power density and temperature can then be made similarly as for exchange bias layers. The main difference between exchange bias and RKKY based temperature measurements is that, exchange bias allowed for resistance measurements after a pulse had been applied, while RKKY requires the measurement to be realized under applied pulse voltage since the rotation of magnetization due to spin-flop is reversible and not observable in the remanent state.

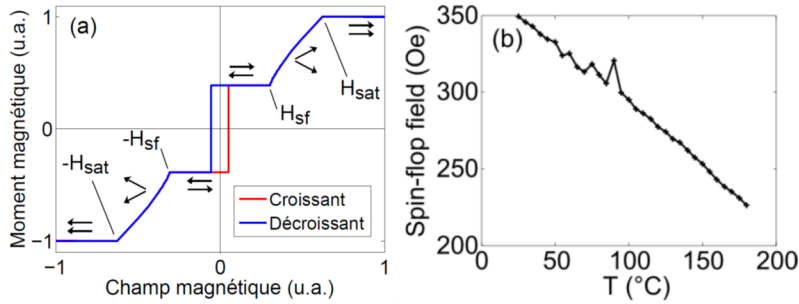


Figure 2.9 – (a) Illustration of magnetization alignment in SAF coupled ferromagnets, where the spin-flop field H_{sf} was used as a local thermometer. (b) Linear dependence of H_{sf} is obtained as function of the substrate temperature T , and (not shown here) also as function of the power density ($\propto V^2$) [37].

The potential for temperature measurements was then confirmed using the RKKY temperature dependence to measure a thermal time constant of $\tau = 3ns$ in thermally assisted MRAM cells without thermal barriers using oscilloscope based real time measurements [37]. The results also confirm the validity of the linear approximation for the RKKY temperature dependence, with RKKY vanishing at 500K for the 0.9nm Ru spacer used.

2.3.6 Spin transfer torque writing

The next stage of evolution for thermally assisted writing MRAM was to use spin transfer torque to set the storage layer magnetization direction. Magnetic field writing requires current flow in a metal line generating less than $10\text{Oe}/mA$, even when using field concentration with magnetic cladding layers. The current to generate the magnetic field, is responsible for most of the cell write power consumption. Higher efficiency can be obtained if the same current can be used to generate the temperature increase and to reverse the storage layer direction by spin transfer torque. A first requirement is to adjust the $R \times A$ of the tunnel barrier to heat the storage layer beyond the antiferromagnet blocking temperature. Then the current density must be higher than the critical current density for STT switching.

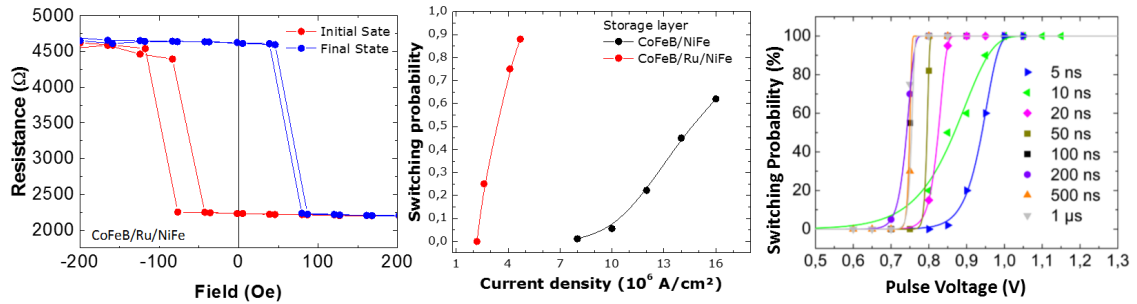


Figure 2.10 – (a) Demonstration of thermally assisted STT writing of exchange biased SAF layer $CoFeB2/Ru0.8/NiFe1.5/IrMn6.5nm$. (b) Decrease of critical current density using SAF layer compared to $CoFeB2/NiFe3/IrMn6.5nm$ storage. (c) Write voltage increase in the precessional limit.

This working principle was demonstrated first with a $CoFe/NiFe/IrMn$ exchange biased storage layer. It was then further optimized using an SAF structure $CoFe/Ru/NiFe/IrMn$ to obtain simultaneously large exchange bias and low coercivity fields, as illustrated in Fig. 2.10. It clearly shows that the exchange bias direction of the storage layer is defined by the current polarity, with unique resistance values measured in the remanent state at zero field. The STT current density of $1.110^7 A/cm^2$ of the first $CoFe/NiFe$ is a large value, because the $5.5nm$ thick storage layer has a high demagnetizing field value. This demagnetizing field is reduced by using the SAF structure and by the lower magnetic moment of thinner $NiFe$, resulting in lower current density levels that have also been attributed to a lower effective volume caused by spin accumulation at the $CoFeB/Ru$ interface [38].

Similarly to the previously discussed relaxation of exchange bias, STT switching is also a thermally activated process. This behavior is again the result of the energy barrier between equilibrium states being reduced by the spin transfer torque current by a factor equal to $(1 - \frac{I}{I_c})$, I_c being the STT critical current. Equation 2.15, and expressions derived from it, can be written similarly for STT switching by replacing power density P by current I , the new driving force for switching being the spin polarized current [39]. As observed from Fig. 2.10 (c), when approaching pulse widths close and below $t = 10ns$, the STT switching current increases as $1/t$, corresponding to a transition from a thermally activated regime to a precessional regime, i.e. limited by the magnetization precession.

Magnetization precession

As can be seen from the LLGS equation 2.1, when the magnetization \vec{M} and spin polarization \vec{P} are co-linear, there is no torque to drive the reversal. The reversal process requires an initial angle between \vec{M} and \vec{P} . This angle can result from an initial misalignment, micromagnetic deviations from co-linearity or fluctuations of the magnetization direction above 0K. This process can be observed by following the magnetization reversal process in real-time measurements, as will be discussed in the next chapter.

As was the case in our cells, it can also be observed as a modulation of the reversal probability. Using MRAM cells with high-bandwidth transmission layout, it was possible to follow the current flow through the pillar in real-time using an oscilloscope. The individual reversal traces from parallel to antiparallel state can be observed in Fig. 2.11(b). From all the individual traces, it is then possible to plot the cumulative switching probability as a function of time. Results from two different tunnel junctions, show that switching events are more frequent at distinct time intervals.

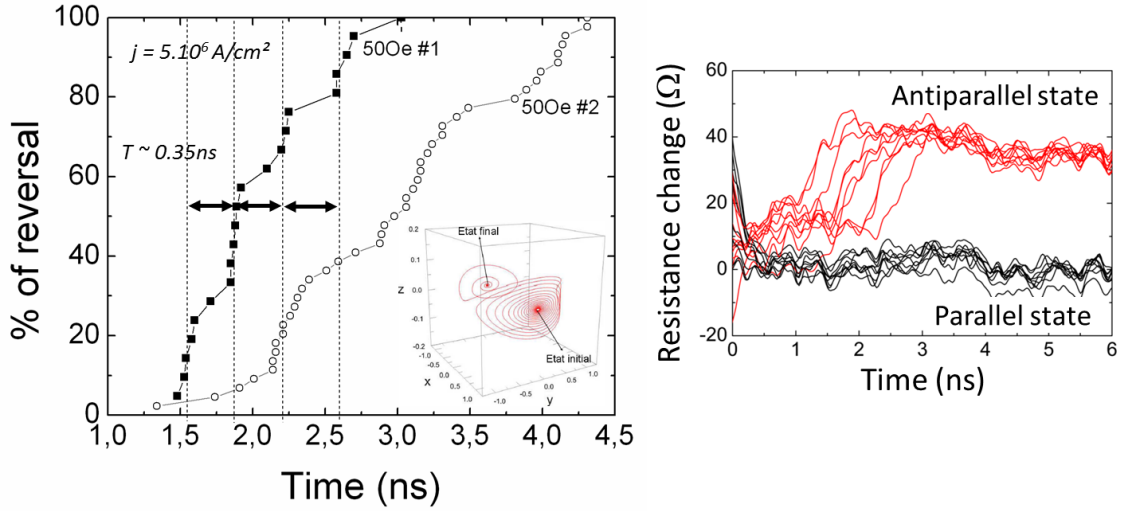


Figure 2.11 – (a) Switching probability steps in precessional switching regime due to the the precessional motion of the magnetization induced by spin transfer torque prior to reversal. (b) Real-time data switching events showing distinct high probability switching times as seen from pulse overlap of different reversal events.

Macrospin simulations can be used to explain this behavior as resulting from the initial precession of the magnetization. Spin transfer torque gradually increases magnetization precession angle, but the magnetization angle is larger as it crosses the layer growth plane, as shown in the inset of Fig. 2.11(a). Probability is highest for magnetization reversal to occur at those positions. The precession frequency can be estimated from the ferromagnetic resonance (FMR) frequency f_{FMR} calculated from Kittel's formula [40] as

$$f_{FMR} = \frac{\gamma}{2\pi} \sqrt{[H + (n_y - n_z)4\pi M_s] [H + (n_x - n_y)4\pi M_s]} \quad (2.22)$$

where H is the applied field, $n_{x,y,z}$ the demagnetizing factors, $4\pi M_s$ the saturation magnetization, and γ the gyromagnetic ratio. Using approximate values of $n_{x,y} \approx t/w_{x,y}$ for the in plane components and $n_z = 1 - n_x - n_y$ for the out of plane component, with t being the free layer thickness and $w_{x,y}$ the lateral widths of the cell, we calculate a precession frequency of 1.5GHz corresponding to a 0.33ns half-precession time. This is close to the 0.35ns half-precession time

observed in the experimental data. However, the precession frequency depends on the effective field, which will vary with cell-to-cell dispersions. This leads to significant variations in the observed precession frequency as seen on data from a second cell having the same nominal dimensions.

2.4 Conclusion

The working principle of thermally assisted MRAM cells with exchange biased storage layer was demonstrated for magnetic field writing, spin transfer torque writing, or a combination of both. This solution reduces the power consumption compared to other field written MRAM cell types requiring two magnetic field lines. It has been recently applied by Crocus Technology to realize, magnetic sensors that can be programmed by setting the direction of the exchange biased storage layer after fabrication. Setting the exchange bias layer direction is a thermally activated process, where the required power density increases as $\log(t)$ with decreasing pulse width. At time scales below $20ns$, comparable or shorter than the cell thermal time constant, the power density requirement increases faster, as $1/t$.

Using these models it is possible to estimate the temperature rise inside the cell stack, starting from a reference measurement in static conditions. The interlayer exchange coupling effect through a Ru spacer could also be used to the same end, in a real-time measurement. Since synthetic antiferromagnets with Ru are widely used, it could be more easily applied to other types of devices. Thermal barriers of low thermal conductivity can be used to increase the heating efficiency of the cell, reducing the power required to heat by a factor of 3. Full advantage of heat confinement by thermal barriers can only be obtained at longer write pulse widths, because of the resulting higher thermal time constants. It can also be argued that using shorter pulse widths is still the best way to reduce the total write energy, however for a fixed pulse width, thermal barriers effectively reduce the write energy compared to systems without them. Writing with combined spin transfer torque and heating effects can be realized by adjusting the $R \times A$ product to the current and power density levels required for switching. In spin transfer torque switching, the magnetization precession upon reversal can result in a modulation of the switching probability. The stochastic nature of the initial angle triggering the spin transfer torque reversal sets a lower limit for STT switching in the 1-10ns pulse width range.

Chapter 3

High speed concepts

Related Thesis

Precessional switching

1. Maria Marins de Castro Souza. Commutation précessionnelle de mémoire magnétique avec polariseur à anisotropie perpendiculaire. PhD thesis, Université de Grenoble, 2011.
2. Bertrand Lacoste. Mastering the influence of thermal fluctuations on the magnetization switching dynamics of spintronic devices. PhD thesis, Université de Grenoble, 2013.

Tunnel barrier breakdown

1. J. Alvarez-Hérault. Mémoire magnétique à écriture par courant polarisé en spin assistée thermiquement. PhD thesis, Université de Grenoble, 2010.
2. S. Amara. Etude de fiabilité des jonctions tunnel magnétiques pour applications à forte densité de courant. PhD thesis, Université de Grenoble, 2012.

Related Publications

1. S. Amara, H. Bea, R. C. Sousa, and B. Dieny. Barrier Breakdown Mechanisms in MgO-Based Magnetic Tunnel Junctions under Pulsed Conditions. In *2012 4th IEEE International Memory Workshop*, pages 1–4, May 2012.
2. S. Amara, R. C. Sousa, H. Bea, C. Baraduc, and B. Dieny. Barrier Breakdown Mechanisms in MgO-Based Magnetic Tunnel Junctions and Correlation With Low-Frequency Noise. *IEEE Transactions on Magnetics*, 48(11):4340–4343, November 2012.
3. S. Amara-Dababi, H. Béa, R. C. Sousa, C. Baraduc, and B. Dieny. Correlation between write endurance and electrical low frequency noise in MgO based magnetic tunnel junctions. *Applied Physics Letters*, 102(5):052404, February 2013.
4. S. Amara-Dababi, H. Bea, R. Sousa, K. Mackay, and B. Dieny. Modelling of time-dependent dielectric barrier breakdown mechanisms in MgO-based magnetic tunnel junctions. *Journal of Physics D: Applied Physics*, 45(29):295002, 2012.
5. S. Amara-Dababi, H. Bea, R. C. Sousa, C. Baraduc, K. MacKay, and B. Dieny. Barrier breakdown mechanisms in MgO-based magnetic tunnel junctions under pulsed conditions and correlation with low-frequency noise. volume 8461, pages 84610G–84610G–11, 2012.
6. S. Amara-Dababi, R. C. Sousa, M. Chshiev, H. Béa, J. Alvarez-Hérault, L. Lombard, I. L. Prejbeanu, K. Mackay, and B. Dieny. Charge trapping-detrapping mechanism of barrier breakdown in MgO magnetic tunnel junctions. *Applied Physics Letters*, 99(8):083501, August 2011.

7. S. Amara-Dababi, R.C. Sousa, H. Béa, C. Baraduc, K. Mackay, and B. Dieny. Breakdown mechanisms in MgO based magnetic tunnel junctions and correlation with low frequency noise. *Microelectronics Reliability*, 53(9-11):1239–1242, September 2013.
8. S. Bandiera, R. C. Sousa, B. Rodmacq, and B. Dieny. Enhancement of perpendicular magnetic anisotropy through reduction of Co-Pt interdiffusion in (Co/Pt) multilayers. *Applied Physics Letters*, 100(14):142410, April 2012.
9. E. Gapihan, J. Hérault, R. C. Sousa, Y. Dahmane, B. Dieny, L. Vila, I. L. Prejbeanu, C. Ducruet, C. Portemont, K. Mackay, and J. P. Nozières. Heating asymmetry induced by tunneling current flow in magnetic tunnel junctions. *Applied Physics Letters*, 100(20):202410, May 2012.
10. M. M. de Castro, B. Lacoste, R. C. Sousa, T. Devolder, L. D. Buda-Prejbeanu, A. Chavent, A. Mejdoubi, S. Auffret, U. Ebels, C. Ducruet, I. L. Prjbeanu, L. Vila, B. Rodmacq, and B. Dieny. Sub-Nanosecond Precessional Switching in a MRAM Cell with a Perpendicular Polarizer. In *2012 4th IEEE International Memory Workshop*, pages 1–4, May 2012.
11. M. Marins de Castro, R. C. Sousa, S. Bandiera, C. Ducruet, A. Chavent, S. Auffret, C. Papusoi, I. L. Prejbeanu, C. Portemont, L. Vila, U. Ebels, B. Rodmacq, and B. Dieny. Precessional spin-transfer switching in a magnetic tunnel junction with a synthetic antiferromagnetic perpendicular polarizer. *Journal of Applied Physics*, 111(7):07C912, April 2012.
12. J. Hérault, R. C. Sousa, C. Ducruet, B. Dieny, Y. Conraux, C. Portemont, K. Mackay, I. L. Prejbeanu, B. Delaët, M. C. Cyrille, and O. Redon. Nanosecond magnetic switching of ferromagnet-antiferromagnet bilayers in thermally assisted magnetic random access memory. *Journal of Applied Physics*, 106(1):014505, July 2009.
13. B. Lacoste, M. Marins de Castro, R. C. Sousa, I. L. Prejbeanu, L. D. Buda-Prejbeanu, S. Auffret, U. Ebels, B. Rodmacq, and B. Dieny. Control of Sub-Nanosecond Precessional Magnetic Switching in STT-MRAM Cells for SRAM Applications. In *2016 IEEE 8th International Memory Workshop (IMW)*, pages 1–4, May 2016.
14. B. Lacoste, M. Marins de Castro, T. Devolder, R. C. Sousa, L. D. Buda-Prejbeanu, S. Auffret, U. Ebels, C. Ducruet, I. L. Prejbeanu, L. Vila, B. Rodmacq, and B. Dieny. Modulating spin transfer torque switching dynamics with two orthogonal spin-polarizers by varying the cell aspect ratio. *Physical Review B*, 90(22):224404, December 2014.
15. C. Papusoi, B. Delaët, B. Rodmacq, D. Houssameddine, J.-P. Michel, U. Ebels, R. C. Sousa, L. Buda-Prejbeanu, and B. Dieny. 100 ps precessional spin-transfer switching of a planar magnetic random access memory cell with perpendicular spin polarizer. *Applied Physics Letters*, 95(7):072506, August 2009.
16. Ioan Lucian Prejbeanu, Sebastien Bandiera, Ricardo Sousa, and Bernard Dieny. MRAM Concepts for Sub-Nanosecond Switching and Ultimate Scalability. *Advances in Science and Technology*, 95:126–135, October 2014.
17. H. W. Schumacher, C. Chappert, P. Crozat, R. C. Sousa, P. P. Freitas, J. Miltat, J. Fassbender, and B. Hillebrands. Phase Coherent Precessional Magnetization Reversal in Microscopic Spin Valve Elements. *Physical Review Letters*, 90(1), January 2003.
18. H. W. Schumacher, C. Chappert, T. Devolder, R. C. Sousa, and P. P. Freitas. Bias field dependence of current-induced precessional magnetization reversal. *Journal of Magnetism and Magnetic Materials*, 286:362–365, February 2005.
19. H. W. Schumacher, C. Chappert, R. C. Sousa, and P. P. Freitas. Current-induced precessional magnetization reversal. *Applied Physics Letters*, 83(11):2205–2207, September 2003.
20. H. W. Schumacher, C. Chappert, R. C. Sousa, and P. P. Freitas. Asymmetry of the effective bit addressing times in ultrafast MRAM write operation. *IEEE Transactions on Magnetics*, 41(10):2649–2651, October 2005.
21. H. W. Schumacher, C. Chappert, R. C. Sousa, and P. P. Freitas. Effective bit addressing times for precessional switching of magnetic memory cells. *Journal of Applied Physics*, 97(12):123907, June 2005.
22. H. W. Schumacher, C. Chappert, R. C. Sousa, P. P. Freitas, and J. Miltat. Quasiballistic Magnetization Reversal. *Physical Review Letters*, 90(1):017204, January 2003.
23. H. W. Schumacher, C. Chappert, R. C. Sousa, P. P. Freitas, J. Miltat, and J. Ferré. Precessional switching of the magnetization in microscopic magnetic tunnel junctions (invited). *Journal of Applied Physics*, 93(10):7290–7294, May 2003.
24. R. C. Sousa, S. Bandiera, M. Marins de Castro, B. Lacoste, L. San-Emeterio-Alvarez, L. Nistor, S. Auffret, U. Ebels, C. Ducruet, I. L. Prejbeanu, L. Vila, B. Rodmacq, and B. Dieny. MRAM concepts for sub-nanosecond precessional switching and sub-20nm cell scaling. In *2013 International Semiconductor Conference Dresden - Grenoble (ISCDG)*, pages 1–3, September 2013.

25. M. M. C. Souza, R. C. Sousa, C. Ducruet, S. Auffret, and B. Dieny. Metallic Mg insertion in rf deposited MgO barrier. *Journal of Applied Physics*, 107(9):09C702, May 2010.
26. A. Vaysset, C. Papusoi, L. D. Buda-Prejbeanu, S. Bandiera, M. Marins de Castro, Y. Dahmane, J.-C. Toussaint, U. Ebels, S. Auffret, R. Sousa, L. Vila, and B. Dieny. Improved coherence of ultrafast spin-transfer-driven precessional switching with synthetic antiferromagnet perpendicular polarizer. *Applied Physics Letters*, 98(24):242511, June 2011.

Related Patents

1. J. Alvarez-Herault, I. L. Prejbeanu, and R. Sousa, "Method for writing to a Random Access Memory (MRAM) Cell with improved MRAM Cell Lifespan," Patent EP2 672 487 (A1), Dec., 2013.
2. B. Dieny, R. Sousa, B. Lacoste, and T. Devolder, "Magnetic Device with Spin Polarisation," Patent EP3 026 721 (A1), Jun., 2016.
3. B. Dieny, C. Papusoi, U. Ebels, D. Houssameddine, L. Buda-Prejbeanu, and R. Sousa, "Magnetic Memory Device with Spin Polarisation, and Method for Using Same," Patent EP2 436 035 (A1) Abstract of corresponding document: WO2 010 136 527 (A1), Apr., 2012.

3.1 Introduction

This chapter will be devoted to different approaches for writing at switching times less than one nanosecond. Coherent precessional switching offers the possibility of achieving a magnetization reversal in sub-*ns* time scales. The results obtained on two types of precessional cells will be reviewed. In the first one, short magnetic field pulses are applied to cause the magnetization leave the film plane and then precess around the demagnetizing field perpendicular direction, while in the second case a perpendicular polarizer is used to achieve the same result through spin transfer torque with no applied magnetic field.

3.2 Field induced precession

Precessional switching [41,42] represents the fundamental ultra-fast limit of induced magnetization reversal. This first demonstration of field induced precessional switching in an MRAM cell provides an understanding of the magnetization trajectory during the reversal process that also applies to the latter demonstration of spin transfer torque induced precession.

The experimental evidence of precessional switching presented in Fig. 3.1 was obtained in micron size magnetic elements, first using spin-valves and later magnetic tunnel junctions. Precessional switching is obtained by applying a short field pulse along the in-plane hard axis direction, along the cell short lateral dimension [43]. The field pulse is created by current flow through a field line above the cell. The RF design layout allows for transmitted pulses with 45ps rise and 100ps fall times (20%–80%), generating a magnetic field up to about 200Oe. There is no spin torque to consider, and the LLG equation describes the magnetization \vec{M} trajectory. When the field pulse is first applied a torque acting on the magnetization is maximum since \vec{M} and \vec{H}_{Eff} are at a right angle to each other. This torque leads \vec{M} to rotate out of the film plane, which creates a strong demagnetizing field \vec{H}_D orthogonal to the plane along the z-direction. This field \vec{H}_D will then exert a torque on \vec{M} , inducing a fast quasi-in-plane rotation of \vec{M} . By terminating the field pulse close to the half precession we obtain a quasiballistic magnetization switching [44]. For pulse widths that correspond to a full precession there is no switching, even though the magnetization has indeed precessed around the same field \vec{H}_D . One interesting characteristic is that the applied field direction can be the same to obtain a reversal independently of the initial magnetization direction.

Reliable coherent magnetization reversal requires high field pulses, revealing the limitations of micron-size elements that tend to break into multi-domain states for low fields or after multiple precessions considerably decreasing the switching reliability. It is interesting to remark that despite requiring 100Oe field pulses corresponding to relatively large 10 – 20mA currents, the total pulse energy for switching is well below 100pJ and as small as 15pJ. This reduction of write energy is obtained because of the very short field pulse lengths below 200ps, corresponding to a 100 times reduction of the pulse width compared to field writing concepts of the previous chapter. This is also possible because the initial alignment of the hard axis field pulse and the magnetization produces maximum torque immediately from the pulse onset. This ballistic switching demonstration shows the possibility for ultra-fast and low power MRAM cells with possible clock rates in the GHz range.

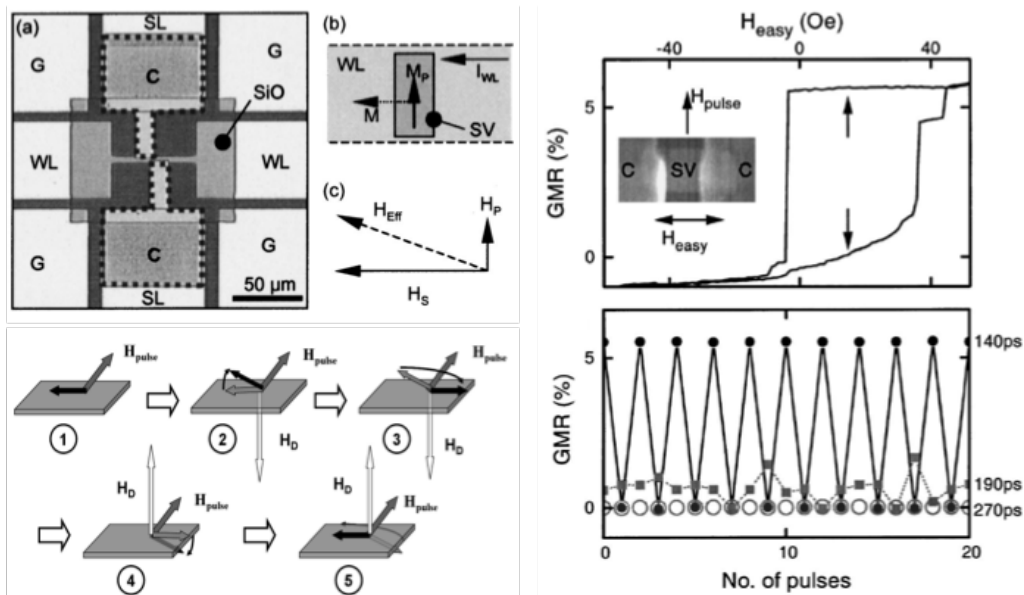


Figure 3.1 – (a-c) High bandwidth cell structure with isolated current line to generate field pulse along the hard axis direction. (d) Illustration of precessional switching step sequence 1 to 5 induced by a hard axis field pulse. (e) Hysteresis loop of spin-valve element and precessional switching demonstration applying consecutive pulses of 140ps.

3.3 Spin transfer torque induced precession

The realization of ultra-fast precessional switching MRAM cells based on spin transfer torque was the subject of two PhD thesis at Spintec. The first one covered the demonstration of the concept and the material integration in a tunnel junction ¹, while the second concentrated on the analysis of the different spin torque contributions to achieve the conditions for deterministic precessional switching ².

The basis of the MRAM cell concept for spin transfer torque induced precessional switching starts by adding a polarizer with perpendicular anisotropy to a conventional in-plane anisotropy STT-MRAM cell. The proposed magnetic tunnel junction consists of three magnetic elements shown in Fig. 3.2. A reference layer with fixed in-plane magnetization direction, a polarizer with out-of-plane anisotropy direction and an in-plane storage layer between the reference layer and the polarizer. All elements are separated by non-magnetic elements, either tunnel barriers or metallic layers. The combined action of the spin-transfer torque on the storage layer can be analyzed by looking at the influence of the perpendicular polarizer and the reference layer separately.

The spin polarized current from the polarizer induces a torque that forces the storage magnetization out of the layer plane [45]. The resulting demagnetizing field then induces a precession of the free layer around the demagnetizing field z-direction. This situation is completely analogous to the discussed field induced precessional switching and also related to spin transfer torque oscillators. The main difference to spin torque oscillators being that they require this out-of-plane precession to be stable under DC current conditions. The STT precessional switching proceeds similarly as for magnetic field induced switching. By controlling the pulse width it is possible to

¹Maria Marins de Castro Souza. Commutation précessionnelle de mémoire magnétique avec polariseur à anisotropie perpendiculaire. PhD thesis, Université de Grenoble, 2011.

²Bertrand Lacoste. Mastering the influence of thermal fluctuations on the magnetization switching dynamics of spintronic devices. PhD thesis, Université de Grenoble, 2013.

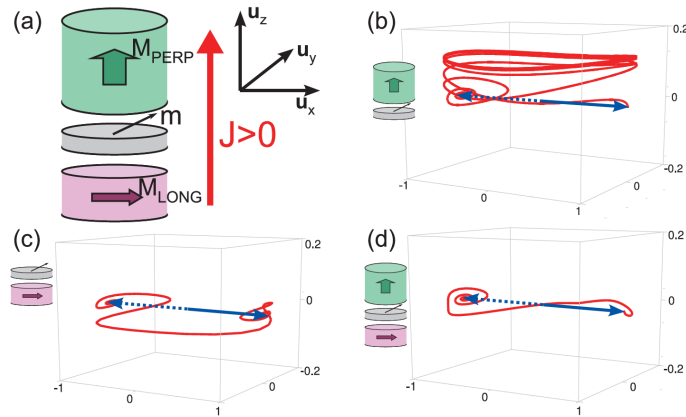


Figure 3.2 – (a) Geometry of a nanopillar with an elliptical cross section. Magnetization dynamics during the reversal of the storage layer in three configurations: with a perpendicular polarizer only (b), with an in-plane reference layer only (c), and with both polarizing layers (d). The magnetization is initially in parallel alignment (solid blue arrow) and switches to antiparallel alignment (dotted blue arrow).

stop the magnetization trajectory at a half-precession such that it relaxes towards the parallel or antiparallel equilibrium state. As before, the precessional switching process to write the parallel or antiparallel state can be realized with the same current polarity for sub- ns pulse widths.

The role of the spin transfer torque current from the reference layer is of second order in this initial implementation of STT precessional switching. At the start of the applied current pulse, the magnetization directions of the reference and storage layer are close to co-linear. Since the spin torque is the vector product of these two magnetizations, it remains close to zero on time scales up to $1ns$, as was already shown in thermally assisted cells written by STT. It is only magnetization fluctuations from this co-linear direction that initiate the STT reversal. Once initiated, the switching itself lasts much less than a nanosecond, however the initial randomness acts as a limit to the total switching speed. The stochastic reversal process can lead to long incubation times [46]. This becomes especially limiting when error rates lower than 10^{-4} are required, such as for fast MRAM applications, since the pulse width has to be chosen such that the error rate is respected even in worst case conditions.

3.3.1 Orthogonal spin polarizer

The integration of a perpendicular polarizer in an in-plane magnetic tunnel junction presents the main advantage of maximizing spin transfer torque from the onset of the pulse, suppressing the stochasticity of the switching and allowing for gains in the total switching energy as for field induced precessional switching.

Co/Pt multilayers for perpendicular polarizer

The first requirement was the development of perpendicular anisotropy hard layers to set the direction of the perpendicular polarizer. Experience in *Co/Pt* multilayers already existed at Spintec [47,48], but the integration of these materials in magnetic tunnel junctions requires the control of different crystallographic structures in the same stack [49]. In this multilayer approach we developed perpendicular anisotropy electrodes using *Co/Pt* or *Co/Pd* multilayers to obtain a reference layer with perpendicular anisotropy. The origin of the perpendicular anisotropy is the

strong spin-orbit coupling between orbital magnetic moment and the intrinsic spin magnetic moment [50]. This link to the crystal structure axes, in $Co/(Pt/Pd)$ multilayers results in an easy axis direction perpendicular to the growth plane of the layers, and perpendicular anisotropy energies of the order of 10^7erg.cm^{-3} .

These studies also showed that the interfacial anisotropy in the Co/Pt and Co/Pd multilayers is asymmetric. The anisotropy induced at the lower interface is at least an order of magnitude larger than that induced at the upper interface [51]. Interdiffusion occurring at the upper interface strongly degrades the anisotropy of the Co/Pt multilayers, and it can be reduced by inserting one or two atomic layers of copper, since Co and Cu are immiscible [52]. The interface anisotropy for the Co/Pd system was 1.2erg.cm^{-2} , while for the Co/Pt system it reached 1.8erg.cm^{-2} . The choice for perpendicular polarizer was to start from a Co/Pt multilayer stack, below the in-plane storage layer.

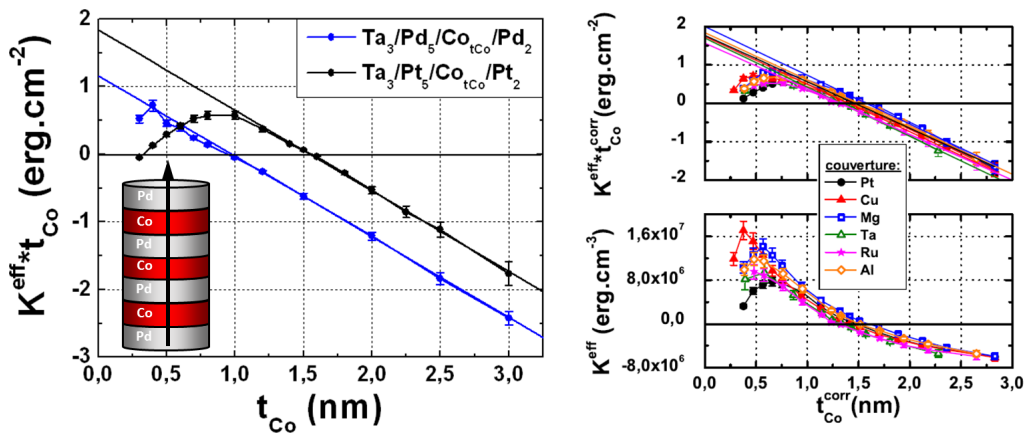


Figure 3.3 – (a) Interface anisotropy of Co/Pd and Co/Pt multilayers as function of Co thickness. Measurements of interface and volume anisotropy for cap layer X in $Ta_3/Pt_5/Co_{t_{Co}}/X/Pt_2nm$ stack.

Synthetic antiferromagnetic (SAF) perpendicular polarizer

The perpendicular polarizer, is also responsible for generating a large dipolar field that cannot be neglected in precessional switching, since it will modify the effective field on the storage layer magnetization. Micromagnetic simulations were carried out to demonstrate the effect of the stray field on the precessional motion [53]. It is possible to reduce the dipolar field of the perpendicular polarizer using RKKY coupling through a Ru layer, as was already the case for in-plane anisotropy layers. The effect of SAF and single-layer polarizers is shown in Fig. 3.4 (a-b) in the two phase diagrams for precessional switching. The switching probability is calculated as a function of pulse width and current density, black corresponds to a final state equal to the initial state, white represents switching and gray corresponds to a vortex state. This vortex state is not a global energy minimum, so that when current is stopped thermal fluctuations will make the system reach one of the two equilibrium states, parallel or antiparallel, with equal probability.

The mentioned vortex state appears at high current density after a few precession cycles, meaning that the coherence of the storage magnetization dynamics is strongly affected for the case of a non-SAF polarizer. Using an SAF perpendicular polarizer reduces the dipolar field and the coherence of the precessional motion of the storage layer magnetization is strongly enhanced.

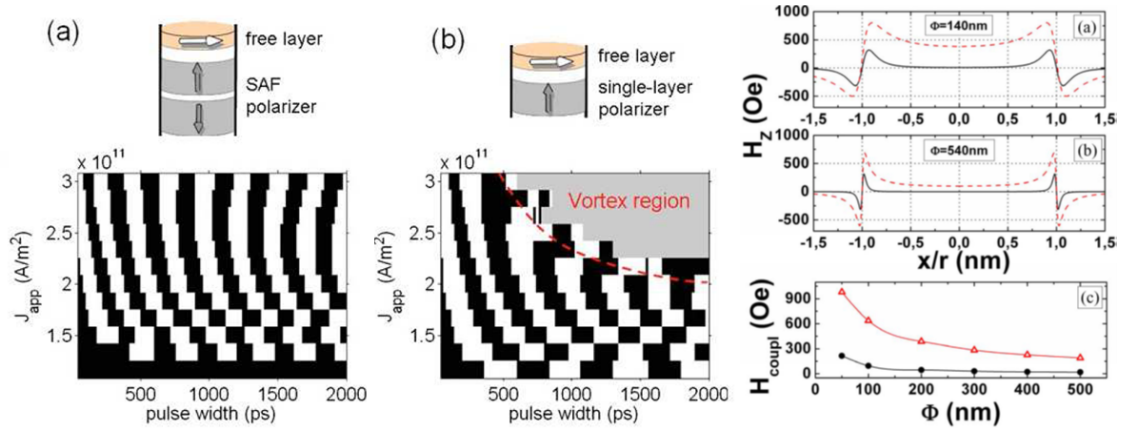


Figure 3.4 – Micromagnetic simulations of precessional switching probability with SAF-polarizer (a) and single-layer polarizer (b), with alternating non-switching (black) and switching (white) regions, the gray region corresponding to vortex formation. (c) Top: Calculation of stray field H_z of SAF (black continuous line) and single layer (red dashed line) along pillar lateral dimension for a 140nm and 540nm diameter. Calculated stray field H_{coupl} of SAF (black dots) and single layer polarizer (red triangles) vs. pillar diameter.

The overall behavior is close to macrospin for the whole pulse duration, improving the switching reproducibility.

Calculations confirmed the reduction of stray field by the SAF polarizer resulting from the opposing magnetization directions. However, since the center of the two magnetic layers does not coincide, they only partially cancel each other, the sidewall edges presenting high dipolar fields compared to the center. As the pillar size is reduced it requires adjusting both contributions to minimize the dipolar interaction [54]. These calculations were also confirmed experimentally on perpendicular anisotropy cells, showing a reduction of the storage layer offset field.

SAF perpendicular polarizer integration

The integration of a perpendicular polarizer below the in-plane anisotropy magnetic tunnel junction was realized starting from two possible options. The first was to separate the perpendicular polarizer structure with a tunnel barrier. The main difficulty of this approach was achieving a sufficiently low RxA product so that the current density was compatible with the threshold required for STT precessional switching. At that time, achieving RxA values around $10\Omega\mu m^2$ was not possible without direct coupling of the storage and polarizer layers. Increasing the barrier thickness allowed for decoupling, but the resulting RxA values were around $100\Omega\mu m^2$. Given these limitations, a solution was found by using a Cu spacer layer between the polarizer and the storage layer.

This created integration problems related to the influence of the crystal growth plane during the tunnel junction annealing process. Copper grown on Ta crystallizes in a face-centered cubic fcc structure with a (111) orientation. During annealing, the initially amorphous $CoFeB$ will crystallize from the (111) template at the copper interface instead of the body centered cubic bcc crystallographic structure, that allows for the spin filtering effect in the MgO barrier. It was possible to maintain a high TMR signal, by introducing a synthetic ferrimagnetic layer in the tunnel junction. The Ru layer acts as a texture breaking layer, separating the fcc phase in the perpendicular polarizer from the bcc phase in the crystallized $CoFe$. The synthetic ferrimagnet storage layer and MgO tunnel barrier showed good magnetic properties, all layers behaving as decoupled. In

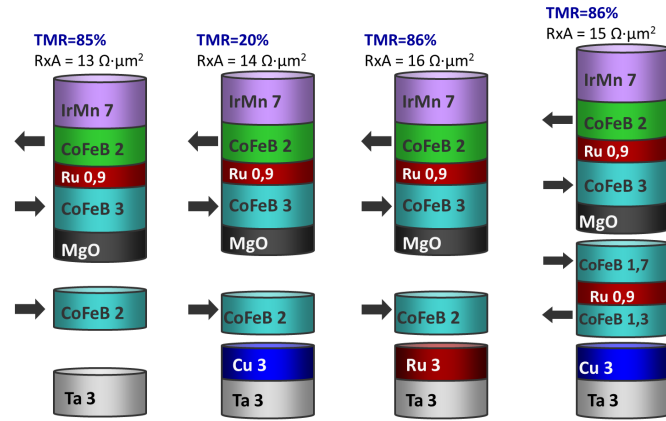


Figure 3.5 – Effect of seed layer on the induced crystallographic structure of the MgO tunnel barrier. The Cu seed induces crystallization of the $CoFeB$ from an fcc template resulting in low TMR. Using a Ru spacer it is possible to realize the structural transition from the fcc seed layer to bcc MgO and full TMR is recovered.

addition, the value of TMR and RxA are the same as those found for a planar junction without a perpendicular polarizer, confirming the successful integration with the MgO tunnel junction.

3.3.2 STT precessional switching

Precessional switching was first verified by measuring the switching probability as function of the applied pulse width, as shown in Fig. 3.6 for an applied pulse amplitude of $1.42V$ corresponding to an average trace of 50 single-shot experiments. Oscillations of the reversal probability are present for both directions of current, and they were observed in the voltage range $1.1 - 1.9V$ corresponding to current densities $7.6 - 12 \cdot 10^6 A/cm^2$. The switching probability oscillation is not a direct proof of precession but, as will be shown from real-time trace measurements, they are indeed the result of the induced precession from the perpendicular polarizer. The high probability peaks correspond to half-precession multiples, and the troughs to multiples of a complete precession. From the damped probability oscillation, it becomes clear that magnetization precession loses coherence over multiple precessions. This is likely due to thermal fluctuations resulting in phase shifts created by small changes in the precession frequency. The full de-coherence time estimated from the initial amplitude decay is $10ns$, however the amplitude will not decrease to zero it will decay to the 50% level.

From switching probability data it is possible to draw a phase diagram of the probability dependence on the pulse duration and the current density. This was done for writing to the antiparallel state for both current directions corresponding to electron flow from or into the perpendicular polarizer, as shown in Fig. 3.7 (a). Qualitatively, the diagrams show switching probability bands similar to those calculated from micromagnetic simulations in Fig. 3.4. Oscillations are also more well defined for positive applied voltages, with a clear first oscillation band and a less well defined second oscillation band. This positive voltage corresponds to an electron flow first through the perpendicular polarizer and into the storage layer. This could result from an asymmetry in the spin polarization for electrons transmitted or reflected by the copper spacer layer, the transmission coefficient of spin polarization being greater than that of reflection.

Since these bands represent high switching probability, it is evident that as the current is increased, close to 100% switching after the first half precession is observed at increasingly shorter

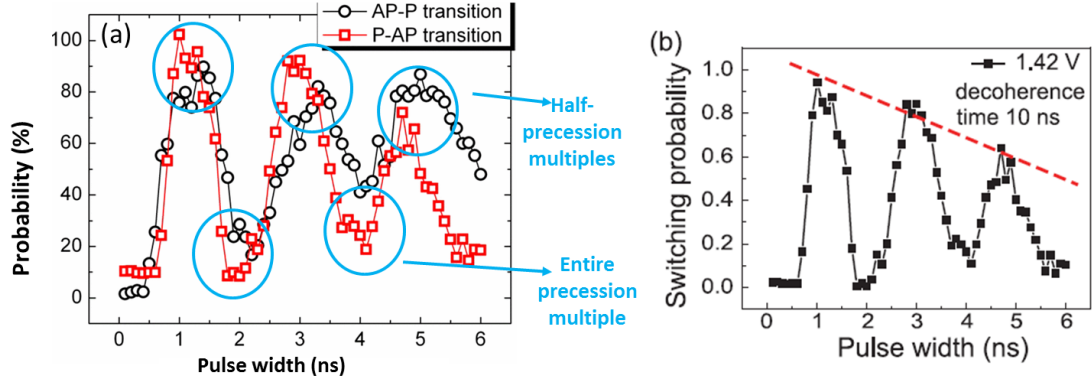


Figure 3.6 – (a) Oscillation of the switching probability for 1.4V pulses applied to switching to the parallel P or the antiparallel AP state. (b) Decay of the switching probability oscillation amplitude due to de-coherence of the induced precession.

times. The pulse width at which the first half precession occurs is plotted in Fig. Fig. 3.7 (a) for different junctions of elliptical shape $80 \times 270nm$ [55]. The continuous lines represent fits to an adiabatic precessional model of the critical current J_c density

$$J_c = J_0 \left[1 + \frac{\tau_{relax}}{t} \ln\left(\frac{\pi/2}{\theta_0}\right) \right] \quad (3.1)$$

where J_0 is the intrinsic critical current density, τ_{relax} a relaxation time, θ_0 the initial angle of the free layer magnetization with respect to the reference layer and t the pulse width. The model seems to apply to the free layer switching, even when the precession is induced by the perpendicular polarizer, suggesting that the actual reversal still depends on the initial free layer angle and a characteristic relaxation time. The devices also show an increase of the precession frequency proportional to the current density as seen in the inset. This is expected in precessional switching, since the storage layer precession is induced by the perpendicular polarizer. From analysis realized for spin torque oscillators using a perpendicular polarizer, the frequency of the out-of-plane precession depends linearly on the applied voltage, and can be calculated as [56]:

$$f_0 = J_c \frac{\hbar}{2e} \frac{\gamma}{2\pi\alpha} \frac{\eta}{M_s t} \quad (3.2)$$

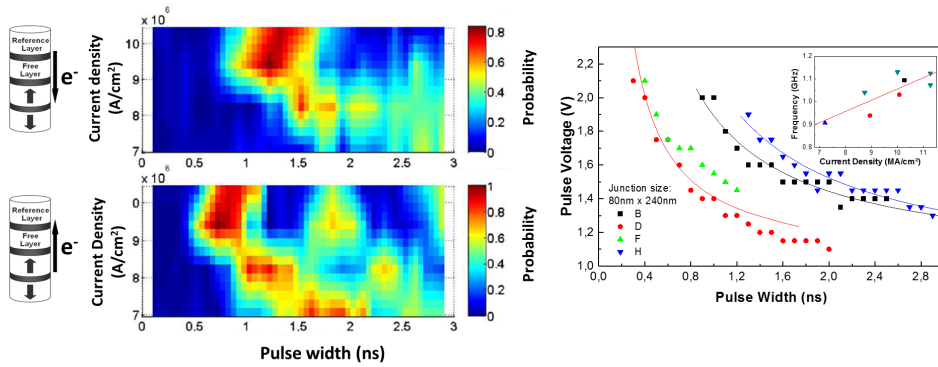
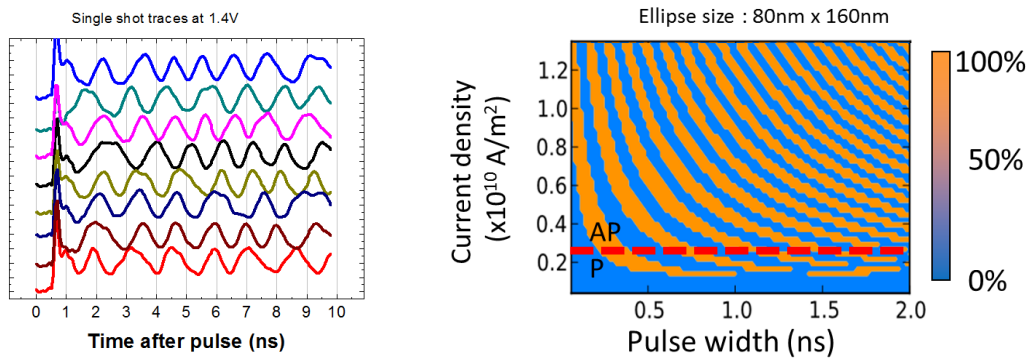


Figure 3.7 – (a) Switching probability of P-AP reversal for electrons flowing *into* and *out-of* the perpendicular polarizer. (b) Position of the first half precession for the P-AP reversal on $80 \times 270nm$ junctions, the inset showing the linear relation between precession frequency and current density.

Since the oscillation frequency increases with the applied current, it results in a frequency blue-shift. Calculation with typical values of saturation magnetization $M_s = 1.2 \cdot 10^6 \text{ A/m}$, $\alpha = 0.01$, $\eta = 0.3$, a volume of $V = 100 \times 100 \times 1 \text{ nm}^3$ and currents of $I = 0.1 \text{ mA}$, i.e. a current density of $1 \cdot 10^6 \text{ A/cm}^2$, result in a frequency f_0 around 2 GHz , corresponding to a switching time half-precession of 250 ps , well below 1 ns .

Real time measurements

Samples with an elliptical cross-section and low aspect ratio (2 : 1) for a nominal size of $160 \times 80 \times 3 \text{ nm}$ were fabricated with a high-bandwidth $\approx 10 \text{ GHz}$ device design layout to obtain single-shot time-resolved measurements of the magnetization reversal. During the application of a 10 ns current pulse, oscillations in each single-shot were observed corresponding to a succession of parallel and anti-parallel states between the free layer and the reference layer. The effect of the perpendicular polarizer is dominant resulting in the precession of the storage layer magnetization. Individual single-shot traces are shown in Fig. 3.8(a) for a 1.4 V pulse. The observed large amplitude oscillation is characteristic of the perpendicular polarizer action. However, after the initial precession oscillations are not very reproducible, showing variations of the precession period in each single-shot trace and even some absent oscillations.



(a) Individual single-shot traces for 1.4 V pulses with 3 GHz low-pass filter applied. (b) Final state phase diagram from macrospin simulations, starting from the parallel state (blue).

Figure 3.8 – Low aspect ratio (2 : 1) precessional STT cell.

Macrospin simulations for this cell geometry were realized to plot the state phase diagram versus pulse duration and current density in Fig. 3.8(b). It shows the expected alternating P and AP regions, i.e. alternating switching and non-switching regions. The precession de-coherence cannot be obtained from such a model, since magnetization is treated as a single macrospin, neglecting micromagnetic distortions, and thermal fluctuations were not considered. It again confirms the induced precession above the critical current, showing also a higher precession frequency with increasing current.

These results prove that it is possible to achieve precessional writing under 1 ns using a perpendicular polarizer. For writing to be successful, the pulse width must be timed to stop after a single half reversal because of precession de-coherence at longer time scales. Together with the fact the initial state must be read before writing, it does not completely fulfill the requirements for fast writing in a high-speed MRAM cell.

3.3.3 Deterministic switching

The two precessional switching methods presented above are not deterministic. However it is possible to find a solution to achieve deterministic precessional switching, by analyzing both conditions necessary for precession and STT switching. The storage layer is under the influence of two STT contributions from the perpendicular polarizer and the in-plane reference layer. Tuning the relative amplitude of these contributions provides the possibility for the final state to be determined by the current pulse direction while at the same time reducing the switching stochasticity. The critical current for STT switching of the free layer is recalled as

$$j_c^{long} = \frac{2e}{\hbar} \frac{\alpha}{\eta_{long}} \mu_0 M_s t \left(H_k + \frac{M_s}{2} \right) \approx \frac{2e}{\hbar} \frac{\alpha}{\eta_{long}} \frac{\mu_0 M_s^2 t}{2} \quad (3.3)$$

On the other hand, structures with a perpendicular polarizer as used in spin torque oscillators also exhibit a critical current density, above which precession of the free layer magnetization exists. The critical current density for precession induced by a perpendicular polarizer can be calculated from the study of the equilibrium stability [57,58] and is written as

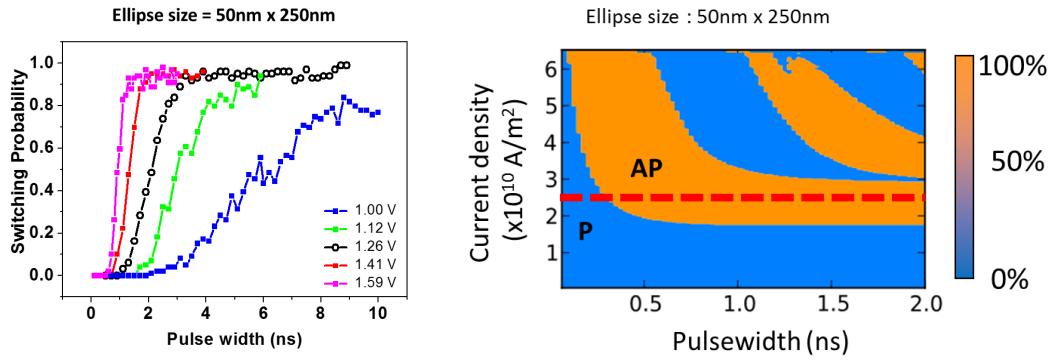
$$j_c^{opp} = \frac{2e}{\hbar} \frac{1}{\eta_{perp}} \mu_0 M_s t \left(\frac{H_k}{2} \right) \quad (3.4)$$

where H_k is the in-plane anisotropy field. Using these two current density thresholds we can set the conditions necessary for direct bipolar precessional switching to be obtained when

$$j_c^{opp} > j > j_c^{long} \leftrightarrow \frac{j_c^{long}}{j_c^{opp}} < 1 \Rightarrow \frac{\eta_{opp}}{\eta_{long}} \frac{\alpha M_s}{H_k} < 1 \quad (3.5)$$

From this condition, it appears that the in-plane anisotropy H_k is the only parameter that does not directly depend on material parameters, and one that can be determined by the elliptical shape and aspect ratio, as shown in equation 2.6. Tunnel junctions fabricated to a higher aspect ratio of 4:1, with nominal size $250 \times 50 \times 3nm^2$, showed a higher in-plane anisotropy field around $125Oe$. In this case the switching probability measurements showed only direct reversal with no sign of precession even as the voltage was increased to $1.6V$. The switching probability versus the pulse width for different voltage pulse amplitudes in the case of cells with a high aspect ratio is shown in Fig. 3.9(a). In contrast to the previous low aspect ratio cell, no oscillations are observed in the switching probability. For sufficiently long pulses, the final state is fully controlled by the current direction independently of the pulse duration. The same increase in precession frequency is obtained, with larger pulse currents resulting in faster reversal. Sub-nanosecond switching was obtained for pulse amplitudes above $1.12V$, corresponding to a current density of $6 \cdot 10^6 A/cm^2$ and a minimum switching energy of $1.5pJ$.

Macrospin simulations for this high aspect ratio cell were realized as shown in the state phase diagram in Fig. 3.9(b). It again shows alternating alternating switching and non-switching regions, however it is now possible to find current levels where only the initial reversal occurs, and the final state is determined by the current polarity. The diagram shows the final state starting



(a) Switching probability confirming deterministic switching above 1.2V pulses. (b) Final state phase diagram from macrospin simulations, starting from the parallel state (blue).

Figure 3.9 – High aspect ratio (4 : 1) precessional STT cell.

from parallel state (blue). For these simulations, the spin polarizations of the reference layer and of the perpendicular polarizer are respectively of $\eta_{long} = 0.3$ and $\eta_{perp} = 0.05$. The anisotropy field was $H_k = 2880e$, with the same previous layer thickness $3nm$. Time-resolved measurements on cells with a perpendicular polarizer [59] confirmed a vanishing incubation time as the applied pulse voltage is increased. However, at high voltage hints of precessional motion start to appear, as is also expected from the phase diagram simulations for a current density values above the range for direct reversal.

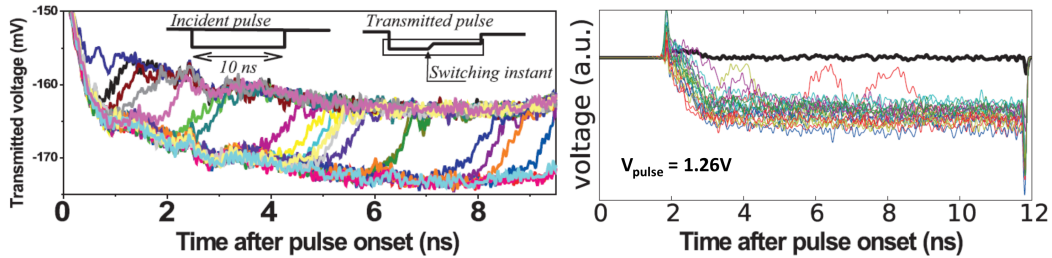


Figure 3.10 – STT switching of MRAM cells in conventional (left) and precessional stacks (right), with comparatively lower stochasticity.

The integration of a perpendicular polarizer in an in-plane tunnel junction MRAM cell allows to realize a bipolar deterministic reversal of the storage layer magnetization. The stochasticity is also reduced, as shown in the comparison on Fig. 3.10, such that it becomes possible to realize reversals in less than $1ns$. This was achieved by increasing the aspect ratio of the cell above 4:1, which at the same time also improves the thermal stability ratio because of the higher anisotropy field. The drawback is the increased footprint of the cell which, for embedded ultra-fast MRAM applications, would still be smaller than equivalent conventional CMOS alternatives.

3.4 Tunnel barrier breakdown

To take full advantage of the precessional switching process, short time pulses of relatively high voltage are required. These high voltages are applied during short times and the breakdown reliability of the tunnel barrier might become a limiting factor for endurance. During the course

of two PhD thesis the magnetic tunnel junction barrier breakdown was investigated looking at the effect of short pulses³ and the repeated application of pulse sequences⁴. This section provides a review of the most important results obtained in these studies.

3.4.1 Breakdown mechanisms

The process involved in tunnel barrier breakdown can be characterized by a Weibull model [60] where the cumulative failure rate $F(t)$ for a total stress time t is described in terms of two parameters η and β .

$$F(t) = 1 - \exp \left[- (t/\eta)^\beta \right] \quad (3.6)$$

The scale parameter η represents the total time required for $[1 - \exp(-1)] = 63.2\%$ of the devices to fail and is directly dependent on test conditions, in particular, the applied voltage. The parameter β reflects the aging mechanism involved and tunnel barrier quality influenced by dispersion in both deposition and process patterning. An example of breakdown characterization is shown in Fig. 3.11 in which the resistance levels of the parallel and anti-parallel states were monitored after each pulse sequence. Resistance levels are stable and breakdown occurs abruptly, and investigations on similar tunnel barriers using high resolution TEM [61] showed that breakdown was associated with localized pinhole defects creating a short through the MgO barrier. The η variation follows an electric field E -model [62] for breakdown where $\log(\eta)$ is proportional to E . This can then be used to extrapolate the expected lifetime at lower voltage pulse conditions and determine the voltage limits for target endurance levels up to 10^{16} write cycles for use as core level memory and 10 year continuous operation.

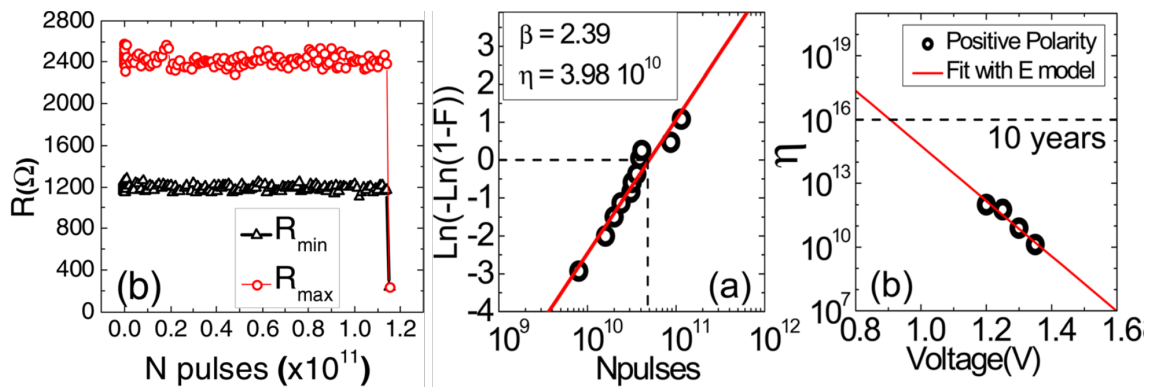


Figure 3.11 – (a) Magnetic tunnel junction R_{min} and R_{max} values vs. number of pulses (100ns and +1.3V). (b) Tunnel barrier failures fitted to Weibull model, plotted on a Weibull scale vs. applied pulse number. (c) Dependence of η with pulse voltage and extrapolation of lifetime assuming an electric field breakdown model.

³J. Alvarez-Hérault. Mémoire magnétique à écriture par courant polarisé en spin assistée thermiquement. PhD thesis, Université de Grenoble, 2010.

⁴S. Amara. Etude de fiabilité des jonctions tunnel magnétiques pour applications à forte densité de courant. PhD thesis, Université de Grenoble, 2012.

Short pulse width

Studies of time-dependent dielectric breakdown can be realized using quasi-static voltage ramps to record the time to breakdown or pulse sequence application and applied to similar magnetic tunnel junction types [63]. The mean time-to-breakdown decreases with temperature [64] showing that the breakdown process is thermally activated and can be correctly described by an Arrhenius model [65] of ion charge trapping in the tunnel oxide barrier. Tunnel barrier breakdown tests were realized on MgO barriers fabricated by plasma oxidation having 65% TMR and $R \times A = 140 \Omega \mu m^2$. They confirmed the equivalence of barrier lifetime obtained from DC voltage and consecutive voltage pulses, when the pulse width is longer than $100ns$. This is shown on Fig. 3.12, with the cumulative barrier failure increasing at the same rate and can be fitted by similar Weibull distribution parameters for $1\mu s$ and $100ns$ pulse widths.

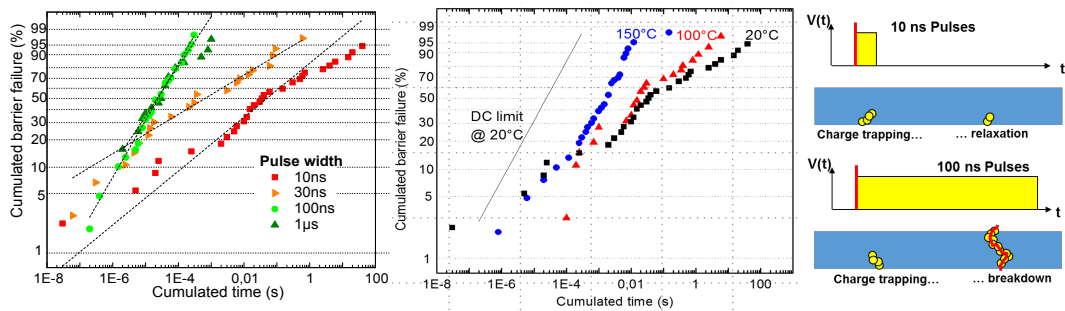


Figure 3.12 – (a) Time-dependent barrier breakdown failure applying constant voltage pulses. (b) Temperature dependence of barrier breakdown for $10ns$ pulses. (c) Illustration of charge trapping relaxation for pulse widths shorter than $100ns$.

At short pulses widths, $10 - 30ns$, a significant increase in lifetime is observed. Since the breakdown is thermally activated, a first possibility to explain the behavior was to verify if a smaller temperature rise for short pulses could be the cause. Measurements at elevated temperatures up to $150^\circ C$ in Fig. 3.12(b) confirmed the thermal activation of the breakdown, but tunnel barrier lifetime was still improved compared to the long pulse limit. A mechanism of relaxation of trapped charges could provide an alternative explanation, with charge trapping propagating progressively in the barrier from the interface where electrons originate [66]. For short pulses, charges remain close to the surface and relax once the current is stopped. Conversely for pulses longer than $100ns$, charge trapping becomes irreversible and once a threshold is reached, the total time under applied voltage becomes the relevant parameter, irrespective of the pulse width.

Pulse sequences

The influence of a delay between consecutive pulses in MgO based tunnel junctions was also investigated. The experiments were performed at a constant pulse width, changing only the delay between pulses. Accelerated breakdown conditions were used with pulse voltage amplitudes of $1 - 1.5V$ corresponding to an electric field of $9 - 14MV/cm$. The results in Fig. 3.13(a-c) show a significant increase in endurance up to 6 orders of magnitude for characteristic intermediate delay times $\tau_0 = 80 - 100ns$ between pulses of $30ns$. The enhancement is observed for both positive and negative voltages, but this endurance peak disappears when pulses of alternating polarity are

used, as seen in Fig. 3.13(a). This cannot be explained simply by heating effects and we developed an interpretation in terms of charging/discharging effects based on qualitative representations of the population of trapped electrons in the barrier as illustrated in Fig. 3.13(d-f).

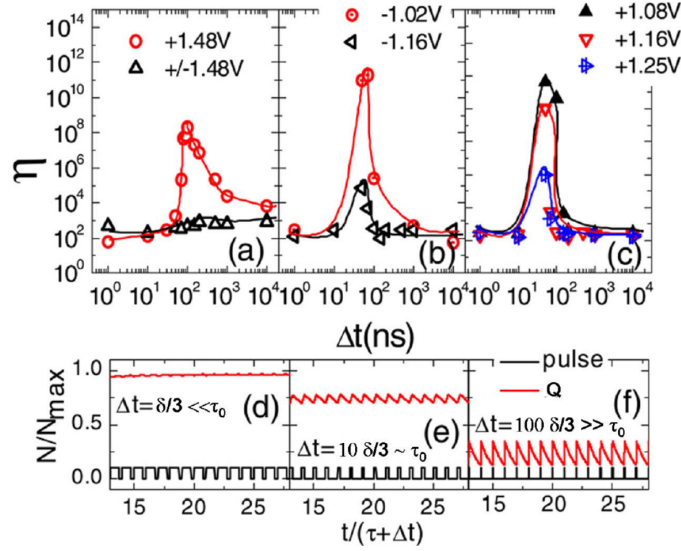


Figure 3.13 – Measurements of η as function of sequential pulse delay for different pulse polarities: positive or bipolar (a), negative (b) and positive (c) for tunnel junctions with $RxA = 30 - 47 \Omega \mu m^2$. (d)-(f) Qualitative representation of trapped electron time variation for cases corresponding to short (d), intermediate (e) and long (f) pulse delays.

The first regime at short pulse delays $\Delta t \ll \tau_0$, corresponds to a continuous increase in the density of trapped electrons, since there is no time for charge relaxation to occur. When an electron gets trapped in the barrier, a screening positive charge appears in the metallic counter-electrode, resulting in a lattice distortion from the electrostatic force between opposite charges estimated to be $10nN$. This stress renders the barrier more fragile, resulting in a reduced endurance. The endurance is also reduced for pulse delays $\Delta t \gg \tau_0$, with enough time for electrons to relax and decreasing the electrostatic force. The barrier is then exposed to an alternating stress favoring atomic mobility that leads to pinhole formation and rapid breakdown. Conditions when $\Delta t \approx \tau_0$ are the most favorable in terms of endurance combining a moderate density of trapped charges and a reduced time modulation of this charge density. Assuming a charge modulation amplitude that is proportional to the applied voltage, the endurance enhancement at $\tau_0 = 100ns$ is expected to decrease for larger voltages, this is indeed confirmed by our data. The proposed mechanism is also consistent with the absence of endurance enhancement for pulses of alternating polarity. In that case electrons are trapped and de-trapped at each alternating pulse independently of the delay Δt , yielding again a strong time-dependent modulation of trapped electron density. These results demonstrate the role played by electron trapping sites in the tunnel barrier breakdown process. They also suggest that higher endurance can be obtained for any delay between pulses in MgO barriers by reducing the number of preexisting traps, originating from defects such as dislocations from the 4.3% lattice mismatch between *CoFe* and *MgO* [67], interstitial defects, *Mg* or *O* vacancies and local inhomogeneity in the oxide tunnel barrier.

3.4.2 Noise measurement correlation

To conclude this section on tunnel junction breakdown, the possibility of using a non-destructive test to predict tunnel junction breakdown was explored by using tunnel junction noise as a measurement parameter. The junction noise, corrected from the background distribution can be measured close to zero bias and generally shows a $1/f$ dependence at low frequency. This is expected for systems containing a large number of noise fluctuators. The $1/f$ noise in tunnel junctions [67,68] can be described using the empirical Hooge formula, equation 3.7, where α is a Hooge-like parameter, γ is the exponent of the $1/f$ noise, R and A are the junction resistance and area, and I is the measurement bias current:

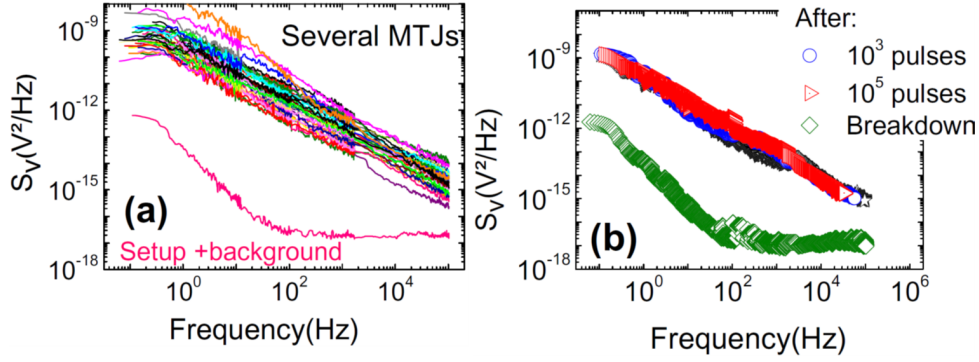
$$S_v = \alpha \frac{V^2}{N f^\gamma} \quad (3.7)$$

$$S_v(V^2/Hz) = \alpha \frac{1}{f^\gamma} \frac{R^2 I^2}{A} \quad (3.8)$$

$$\log(S_v) = -\gamma \log(f) + \log(\alpha) + \log\left(\frac{R^2 I^2}{A}\right) \quad (3.9)$$

It is apparent from equation 3.9 that the most appropriate representation for the noise power density is a log – log plot. In such a scale, a linear fit to the data results in a slope γ defining the type of noise. Fitting noise data shown in Fig. 3.14(a), results in $\gamma \approx 1.05$ confirming the $1/f$ noise type. The Hooge factor α corresponds to the linear fit intercept at $1Hz$, expressed for tunnel junctions in μm^2 units for convenience. Finally, the term $\log(R^2 I^2 / A)$ is a normalization correction, accounting for differences in junction size and bias current. Breakdown tests in accelerated conditions using $1.7V$ pulse sequences were performed, after measuring low frequency noise. Sequences used a pulse width of $30ns$ and a $70ns$ delay between pulses, close to the value maximizing tunnel junction lifetime.

The results on 60 tested junctions in Fig. 3.14(c) shows a broad correlation between tunnel junction endurance and the $1/f$ noise amplitude, Hooge parameter α . Qualitatively, junctions exhibiting low noise prior to the breakdown pulse sequence generally have the largest endurance. This suggests that endurance and noise are both sensitive to electron trapping sites in the barrier. However the dispersion observed in lifetime, ≈ 9 orders of magnitude, is much higher than the 4 orders of magnitude found for the Hooge parameter. A possible explanation is the large voltage difference between noise and breakdown measurements, $36mV$ vs. $1.7V$, leading to a larger number of trapping sites being charged in endurance tests compared to noise measurements [69]. From an endurance perspective, a few of these sites may define the upper limit for the tunnel junction lifetime. However, if only these few defects play a dominant role during oxide breakdown and their activation energy is large, they may not be detected in the noise experiments at low voltage. From a noise point of view, each defect acts as a telegraphic fluctuator with a characteristic dwell time, and a random dwell time distribution yields the $1/f$ noise type. This difference, that a large number of sites contributes to noise characteristics, but only a few are responsible for electrical breakdown, may explain the large scattering of data points in the general trend linking noise and endurance. This argument, suggest a better correlation could perhaps be found by measuring noise at current levels closer to the tunnel junction operating voltage, opening the possibility for it to be used as a predictive tool for tunnel barrier reliability and write endurance.



(a) Tunnel junction noise power density including correction for setup and background noise, (b) measured during the breakdown pulse sequence application.

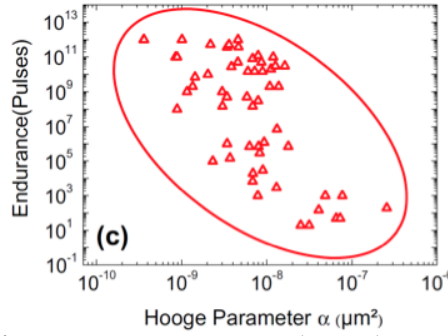


Figure 3.14 – (c) Correlation of noise Hooqe parameter and tunnel junction breakdown pulse endurance.

3.5 Conclusion

It is possible to reverse the magnetization direction with current pulses shorter than $1ns$ by tailoring the pulse timing to favorably exploit the magnetization precessional dynamics. The magnetization precession can be induced by short magnetic field pulses along the cell hard axis, but also by using a perpendicularly spin polarized current into an in-plane anisotropy magnetic layer. A perpendicular anisotropy electrode using Co/Pt multilayers was developed and successfully integrated with in-plane magnetic tunnel junctions. Precessional switching is confirmed by oscillations in the switching probability and from real-time single shot measurements. The first half-precession can be reliably reproduced, but further precessions show significant decoherence times, as short as $10ns$. This reversal process is limited in its application scope, since it critically depends on precise pulse timings. By combining the spin torque contributions of the in-plane reference layer and the perpendicular polarizer, both acting on the storage layer, it is possible to achieve deterministic switching. This was demonstrated using elongated elliptical cells of aspect ratio 4:1, providing a solution to repeatedly write below $1ns$ with the precession stopping after the first half precession. The significant improvement from precessional switching is the reduction of the total energy for writing, because of the short pulse widths. However, the write current density is higher than spin transfer torque switching of other in-plane cells. The relatively high voltage required for switching can cause the tunnel barrier lifetime to decrease below the target endurance limit. A study of tunnel barrier breakdown in magnetic tunnel junctions shows that short pulse widths have positive effect increasing the tunnel junction lifetime, in a process involving a possible relaxation of trapped charges in the tunnel barrier after the pulse is stopped. This assumption of trapped charges was also consistent in explaining significant increases of en-

duration, up to 6 orders of magnitude, when applying pulse sequences of the same polarity with $\approx 70ns$ delays between pulses. The effect disappearing, for both short and long pulse delays and consecutive pulses of opposite polarity. Finally, a possible non-destructive noise measurement showed some correlation to measured endurance. However, it was still too broad to be effectively used, but it suggests possible improvements by measuring noise at higher voltages.

Chapter 4

Scaling to high density: perpendicular anisotropy

Related Thesis

1. Lavinia Nistor. Magnetic tunnel junctions with perpendicular magnetization: anisotropy, magnetoresistance, magnetic coupling and spin transfer torque switching. PhD thesis, Université de Grenoble, 2011.
2. Sébastien Bandiera. Jonctions tunnel magnétiques à anisotropie perpendiculaire et écriture assistée thermique. PhD thesis, Université de Grenoble, 2011.
3. Léa Cuchet. Magnetic and transport properties of single and double perpendicular magnetic tunnel junctions. PhD thesis, Université de Grenoble, 2015.

Related Publications

1. S. Bandiera, R. C. Sousa, S. Auffret, B. Rodmacq, and B. Dieny. Enhancement of perpendicular magnetic anisotropy thanks to Pt insertions in synthetic antiferromagnets. *Applied Physics Letters*, 101(7):072410, August 2012.
2. S. Bandiera, R. C. Sousa, M. Marins de Castro, C. Ducruet, C. Portemont, S. Auffret, L. Vila, I. L. Prejbeanu, B. Rodmacq, and B. Dieny. Spin transfer torque switching assisted by thermally induced anisotropy reorientation in perpendicular magnetic tunnel junctions. *Applied Physics Letters*, 99(20):202507, November 2011.
3. S. Bandiera, R. C. Sousa, Y. Dahmane, C. Ducruet, C. Portemont, V. Baltz, S. Auffret, I. L. Prejbeanu, and B. Dieny. Comparison of Synthetic Antiferromagnets and Hard Ferromagnets as Reference Layer in Magnetic Tunnel Junctions With Perpendicular Magnetic Anisotropy. *IEEE Magnetics Letters*, 1:3000204–3000204, 2010.
4. S. Bandiera, R. C. Sousa, B. Rodmacq, L. Lechevallier, and B. Dieny. Effect of a Cu spacer between Co and Pt layers on the structural and magnetic properties in (Co/Cu/Pt) 5 /Pt type multilayers. *Journal of Physics D: Applied Physics*, 46(48):485003, 2013.
5. L. Cuchet, R. C. Sousa, L. Vila, S. Auffret, B. Rodmacq, and B. Dieny. Field Dependence of Spin-Transfer Torque Switching Current in Perpendicular Magnetic Tunnel Junctions. *IEEE Transactions on Magnetics*, 50(11):1–4, November 2014.
6. Léa Cuchet, Bernard Rodmacq, Stéphane Auffret, Ricardo C. Sousa, and Bernard Dieny. Influence of magnetic electrodes thicknesses on the transport properties of magnetic tunnel junctions with perpendicular anisotropy. *Applied Physics Letters*, 105(5):052408, August 2014.
7. Léa Cuchet, Bernard Rodmacq, Stéphane Auffret, Ricardo C. Sousa, Clarisse Ducruet, and Bernard Dieny. Influence of a Ta spacer on the magnetic and transport properties of perpendicular magnetic tunnel junctions. *Applied Physics Letters*, 103(5):052402, 2013.

8. Léa Cuchet, Bernard Rodmacq, Stéphane Auffret, Ricardo C. Sousa, Ioan L. Prejbeanu, and Bernard Dieny. Perpendicular magnetic tunnel junctions with a synthetic storage or reference layer: A new route towards Pt- and Pd-free junctions. *Scientific Reports*, 6:21246, February 2016.
9. T. Devolder, J.-V. Kim, L. Nistor, R. Sousa, B. Rodmacq, and B. Diény. Exchange stiffness in ultrathin perpendicularly magnetized CoFeB layers determined using the spectroscopy of electrically excited spin waves. *Journal of Applied Physics*, 120(18):183902, November 2016.
10. L. San Emeterio Alvarez, B. Lacoste, B. Rodmacq, L. E. Nistor, M. Pakala, R. C. Sousa, and B. Dieny. Field-current phase diagrams of in-plane spin transfer torque memory cells with low effective magnetization storage layers. *Journal of Applied Physics*, 115(17):17C713, May 2014.
11. R. C. Sousa, S. Bandiera, M. Marins de Castro, B. Lacoste, L. San-Emeterio-Alvarez, L. Nistor, S. Auffret, U. Ebels, C. Ducruet, I. L. Prejbeanu, L. Vila, B. Rodmacq, and B. Dieny. MRAM concepts for sub-nanosecond precessional switching and sub-20nm cell scaling. In *2013 International Semiconductor Conference Dresden - Grenoble (ISCDG)*, pages 1–3, September 2013.
12. M. M. C. Souza, R. C. Sousa, C. Ducruet, S. Auffret, and B. Dieny. Metallic Mg insertion in rf deposited MgO barrier. *Journal of Applied Physics*, 107(9):09C702, May 2010.
13. A. A. Timopheev, R. Sousa, M. Chshiev, L. D. Buda-Prejbeanu, and B. Dieny. Respective influence of in-plane and out-of-plane spin-transfer torques in magnetization switching of perpendicular magnetic tunnel junctions. *Physical Review B*, 92(10):104430, September 2015.
14. A. A. Timopheev, R. Sousa, M. Chshiev, H. T. Nguyen, and B. Dieny. Second order anisotropy contribution in perpendicular magnetic tunnel junctions. *Scientific Reports*, 6:26877, June 2016.
15. L. You, R. C. Sousa, S. Bandiera, B. Rodmacq, and B. Dieny. Co/Ni multilayers with perpendicular anisotropy for spintronic device applications. *Applied Physics Letters*, 100(17):172411, April 2012.

Related Patents

1. I. Joumard and R. Sousa, “Générateur de champ magnétique,” Patent FR1650184, Jan., 2016.

4.1 Introduction

The in-plane anisotropy cells described in the previous chapters, are not compatible with scaling to sub-20nm cell dimensions. For this goal, the source of anisotropy can be neither in-plane shape anisotropy nor exchange bias. For exchange bias in thermally assisted MRAM, the issue is related to the reduced number of grains that scaling implies, leading to increased cell-to-cell dispersion [20, 21]. There is also the issue of generating increasingly larger fields to set the magnetization direction, while at the same time reducing the cross section of the field generating current lines, leading to current densities above the *Cu* line electromigration limit. For in-plane cells written by STT or precessional switching, stability of small cells requires increasingly higher aspect ratios to cope with the reduction of the magnetic volume, which contradicts the small size goal [70]. From that point of view, perpendicular anisotropy would allow small circular shape elements to achieve energy barriers of $70k_B T$ at least in the 20 – 30nm diameter range, and possibly also at smaller dimensions. A second major reason to consider perpendicular anisotropy cells, is that the critical current required to reverse the magnetization is reduced compared to in-plane cells, assuming the same thermal stability factor in both cell types [71].

4.2 Spin transfer torque and perpendicular anisotropy

In the case of a magnetic element with perpendicular anisotropy and cylindrical symmetry, it is possible to separate the reversal magnetization dynamics into a precession term and a reversal component defining the polar angle. Assuming a symmetry axis *z* along the perpendicular anisotropy easy axis direction, the LLGS equation 2.1 can be re-written as

$$\frac{1 + \alpha^2}{\gamma} \frac{d\vec{m}}{dt} = -\vec{m} \times \left[\vec{H}_{eff} - (b_{\perp} + \alpha a_{\parallel}) \vec{p} \right] - \vec{m} \times \left[\vec{m} \times \left(\alpha \vec{H}_{eff} - (a b_{\perp} - a_{\parallel}) \vec{p} \right) \right] \quad (4.1)$$

$$\frac{1 + \alpha^2}{\gamma} \frac{d\vec{m}}{dt} = -\vec{m} \times A\vec{z} - \vec{m} \times (\vec{m} \times B\vec{z}) \quad (4.2)$$

where $\vec{m} = \vec{m}/M_s$ is the unit vector along the free layer magnetization direction, M_s the magnetization saturation, \vec{H}_{eff} the effective field, \vec{p} the unit vector along the reference layer magnetization direction, while a_{\parallel} and b_{\perp} are the in-plane (damping-like) and out-of-plane (field-like) STT coefficients. Two scalar parameters A and B can be introduced in equation 4.2, corresponding to the precession of the magnetization about the symmetry axis *z*, and rotation of the magnetization upon reversal. The value of A defines the magnetization precession frequency, while B corresponds to a change in the polar angle θ . The first term is analogous to a modified ferromagnetic resonance (FMR) condition, with a precession frequency defined by Kittel's easy axis formula as

$$\frac{\omega}{\gamma} = H_{eff} - (b_{\perp} + \alpha a_{\parallel}) \quad (4.3)$$

where ω is the angular frequency of the precession. The second term B reflects the condition necessary for magnetization reversal to occur, i.e. when the value of B changes sign. This corresponds to a switching threshold for the STT-induced reversal defined by

$$\alpha \vec{H}_{eff} + a_{||} - \alpha b_{\perp} = 0 \quad (4.4)$$

A very important consequence is that compared to the in-plane geometry, the influence of the b_{\perp} 'field-like' torque parameter is weighted by the Gilbert damping parameter α , typically 0.02 – 0.001, which significantly reduces the impact of b_{\perp} by up to a factor of 1000. From equation 4.4, setting $\alpha b_{\perp} = 0$, we find the usual perpendicular geometry critical current density for switching, which in the presence of field H is written as

$$j_c^{perp} = \frac{2e}{\hbar} \frac{\alpha}{\eta} \mu_0 M_s t (H_k + H) \quad (4.5)$$

where $a_{||} = \frac{\hbar}{2e} \frac{\eta}{M_s t}$ corresponds to a conversion factor in units of $Oe/(A/cm^{-2})$. One can also notice that this equation defines a simple linear switching boundary with respect to the applied field [72,73]. This equation can be used to draw a state phase diagram as shown in Fig. 4.1, where inside the rhombus-like central region the free layer can be along either of the two equilibrium directions, in parallel P or antiparallel AP alignment with the reference layer direction.

It had been considered to use stability phase diagrams boundaries to study the bias voltage dependence of the b_{\perp} 'field-like' term, however because of the defining equation 4.4 for perpendicular anisotropy MTJ structures the value of b_{\perp} would have to be unphysically much higher than $a_{||}$ for its bias voltage dependence to be experimentally measured as a deviation from the straight line boundary. Our analysis defines a possibility to reveal the influence of the 'field-like' STT term from the frequency of the precession, provided that it could be separated from the nonlinear influence of the oscillation amplitude on the frequency.

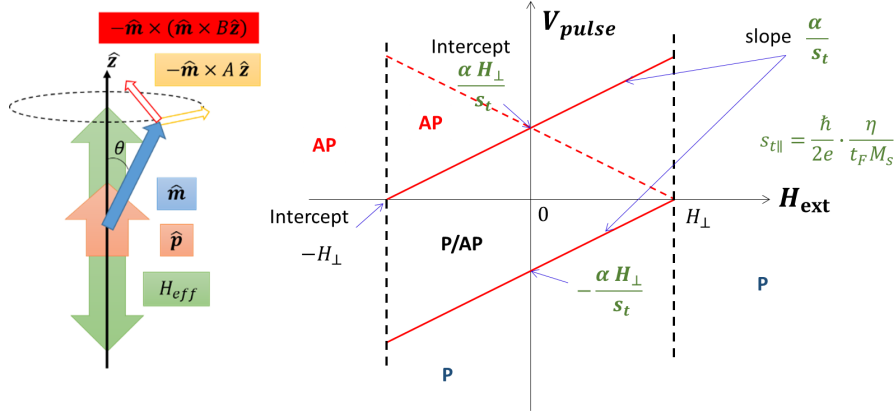


Figure 4.1 – (a) Geometry of a perpendicular anisotropy MTJ with symmetry axis and easy axis direction z . (b) STT Stability phase diagram constructed from Eq. 4.5 assuming $\alpha b_{\perp} = 0$.

From the phase diagram it is possible to extract important parameters. The critical current density, or voltage, for switching is obtained from the intercept of the field-current boundary at zero field, when the free layer offset fields are compensated. Defined more generally, it can be obtained from the crossing point of the two boundaries, positive and symmetric negative boundary, dashed red line in Fig. 4.1. This point represents the field at which it is possible to switch the

free layer with the same positive and negative voltage value, for both the $P \rightarrow AP$ and $AP \rightarrow P$ transitions.

It is also possible to access material related storage layer parameters, like the anisotropy H_k from the intercepts of the boundaries at zero voltage. Also the damping α can be obtained from the boundary slope provided that the value of M_s is known, and the effective spin polarization parameter η is constant, or weakly dependent on the voltage. Spin polarization can then be calculated from TMR as $\eta = \sqrt{TMR/(TMR + 2)}$ according to Jullière's formula assuming identical spin polarization η in both reference and free layer electrodes. For convenience we can write the critical current directly in terms of the thermal stability $\Delta = E_b/k_B T$ in the absence of applied magnetic field H as

$$I_c^{perp} = \frac{4e}{\hbar} \frac{\alpha}{\eta} K_{eff} V \iff I_c^{perp} = \frac{4e}{\hbar} \frac{\alpha}{\eta} \Delta k_B T \quad (4.6)$$

This relation shows that the critical current required to set the free layer magnetization with STT is directly proportional to the thermal stability value. Unlike in-plane anisotropy cells, there is no write current penalty from the demagnetizing field. It also means that the ratio of Δ/I_c can be viewed as a *figure of merit* for STT switching efficiency. It also serves as a reminder to evaluate critical current densities together with the cell thermal stability, since low values of critical current can often be traced back to low thermal stability cells, rather than high spin torque efficiency.

4.2.1 Thermal stability

Several methods can be used to evaluate the cell thermal stability, relying on some assumption for the energy barrier to vary with applied field or current [74–78]. In our measurements we assumed $E_b(H) = E_b(0)(1 - H/H_k)^n$, with $n = 2$ for a coherent rotation model. Applying a linear magnetic field ramp, with an increasing/decreasing field rate R , the thermal stability can be obtained from the coercive field dispersion, or directly from fitting the switching probability $p(H)$ as [79]:

$$p(H) = 1 - \exp \left[-\frac{H_k}{\tau_0 R} \sqrt{\frac{1}{\Delta}} \frac{\sqrt{\pi}}{2} \operatorname{erfc} \left(\sqrt{\frac{1}{\Delta}} \left(1 - \frac{H}{H_k} \right) \right) \right] \quad (4.7)$$

This method has the advantage of allowing to obtain both the thermal stability ratio Δ and the anisotropy value H_k . The consistency of the calculated parameters can then be verified against the measured coercivity value H_c , as in the Néel-Brown thermally activated reversal model where it is defined as

$$H_c = H_k \left[1 - \left[\frac{1}{\Delta} \ln \left(\frac{t_m f_0}{\ln 2} \right) \right]^{1/n} \right] \quad (4.8)$$

t_m being the measurement integration time, while the exponent n depends on the reversal mechanism, with $n = 2$ for coherent rotation. The highest values of Δ and H_k are obtained using $n = 2$, decreasing as $n \rightarrow 1$, with $n = 1.5$ representing a reduction of $\approx 30\%$ compared to those obtained for $n = 2$.

Reliable determination of the thermal stability is an important field, where models will need

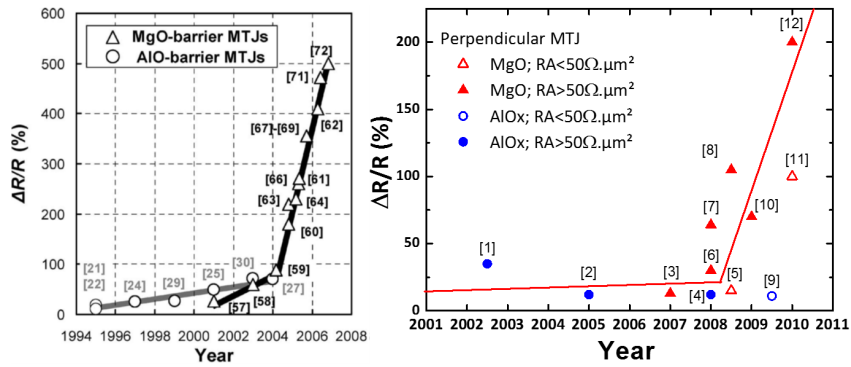


Figure 4.2 – (a) Evolution of TMR for in-plane anisotropy tunnel junctions for amorphous AlO_x tunnel barrier and (001) textured MgO [80]. (b) TMR in perpendicular anisotropy tunnel junctions for AlO_x and MgO tunnel barriers

to include temperature dependence of material parameters, especially perpendicular anisotropy. Other difficulties are associated with the time required to complete tests and the result extrapolation to 10 year thermal stability data, as measured from random single cells to a full Mbit matrix. The present *gold standard* is still the measurement of data errors in a full matrix kept at elevated temperature for hours, days or weeks.

4.2.2 Materials for perpendicular anisotropy

As a starting point for the use of perpendicular anisotropy electrodes in magnetic tunnel junctions the major difficulty resides in the integration of these electrodes with a (001) MgO barrier to obtain the spin filtering effect required for high TMR. This is readily illustrated in Fig. 4.2 from the evolution of the TMR record values observed for in-plane and perpendicular MTJ over the years [80]. The effect of the symmetry based selection of tunneling electrons in MgO , contributing to enhanced spin filtering and large TMR values, was first achieved for in-plane anisotropy samples [81, 82]. Crystallization of the MgO in the (001) texture starting from *bcc* electrodes (*Co*, *Fe* or *CoFe*), or having this crystal structure induced through annealing starting from an amorphous *CoFeB* electrode, as is most commonly the case [49].

Perpendicular anisotropy material candidates for MTJ electrodes initially relied on perpendicular interface anisotropy from spin-orbit interaction, as is the case for *Co/Pt* buffers and multilayer stacks. These multilayers start from a *Pt* buffer that has an *fcc* crystal structure presenting a (111) surface orientation. Because of the large mismatch in the structural symmetry, the MgO rock-salt (001) structure cannot be effectively grown on *fcc* (111) seeding layers.

Our contribution to the development and integration of perpendicular anisotropy materials in magnetic tunnel junctions has spanned 3 PhD thesis. We have been able to demonstrate that perpendicular anisotropy at the ferromagnet-tunnel barrier interface is large enough to define a perpendicular easy axis direction, even without *Pt* buffer layers¹. At the same period we investigated high perpendicular anisotropy materials for the reference electrode and to be used in

¹Lavinia Nistor. Magnetic tunnel junctions with perpendicular magnetization: anisotropy, magnetoresistance, magnetic coupling and spin transfer torque switching. PhD thesis, Université de Grenoble, 2011.

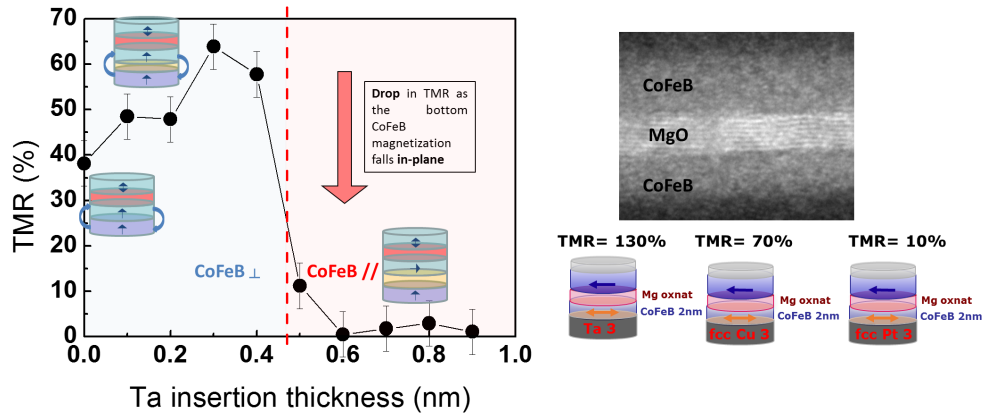


Figure 4.3 – (a) TMR dependence of reference layer Ta insertion in perpendicular anisotropy tunnel junctions. (b) Influence of buffer layer structure on TMR.

thermally assisted perpendicular anisotropy cells² and then specifically on the integration of these electrodes in a magnetic tunnel junction with large tunnel magnetoresistance³. Developments in the optimization of materials to increase anisotropy and TMR are still on-going related to the optimization of the natural oxidation process and tunnel barrier growth and the introduction of refractory materials to increase the resistance to high annealing temperatures.

4.2.3 Magnetic tunnel junction integration

The use of Co/Pt multilayers as a perpendicular polarizer, described in section 3.3.1, has the same requirements as the reference layer of a perpendicular anisotropy tunnel junctions. The issues related to crystal structure compatibility are present, since the Co/Pt multilayer has an fcc structure, resulting in low TMR as shown in Fig. 4.3(b). The equivalent in-plane magnetic tunnel junction grown on Ta , Cu or Pt buffer showed a reduction of TMR from 130% to only 10% in the case of $fcc - Pt$. A solution found to obtain compatible crystal structure growth was to use an insertion of Ta introduced in the magnetic reference electrode of the magnetic tunnel junction. It can effectively decouple the crystallization of the $CoFeB$ layer from that of the adjacent Co/Pt or Co/Pd multilayers. The Ta insertion significantly improves the TMR signal [83]. However, it is necessary for this insertion not to break the magnetic coupling with the multilayer SAF structure. This decoupling is effective for Ta thicknesses above $0.4nm$ and immediately results in lower TMR. This lower TMR is not related to the crystal structure, but to the reduction perpendicular anisotropy in the $FeCoB$ reference electrode, such that its anisotropy becomes oriented in-plane. From magnetic and transport measurements carried out on different structure types, a Ta insertion layer of $0.3nm$ is a good compromise to achieve high TMR while maintaining the magnetic coupling. While in our studies the SAF reference electrode with Co/Pt multilayers and Ta insertion became our standard, it is not the only possibility to achieve a high stability refer-

²Sébastien Bandiera. Jonctions tunnel magnétiques à anisotropie perpendiculaire et écriture assistée thermiquement. PhD thesis, Université de Grenoble, 2011.

³Léa Cuchet. Magnetic and transport properties of single and double perpendicular magnetic tunnel junctions. PhD thesis, Université de Grenoble, 2015.

ence direction. There are other high anisotropy alternatives in Heusler alloy materials with low magnetic moment, also having their own growth and crystal structure integration issues. We also investigated *TbCo* a ferrimagnetic rare earth-transition metal (RE-TM) alloy and *Co/Ni* multilayers.

TbCo alloys are possible reference layer structures with high coercivity and low magnetization, which can be adjusted through the composition. These alloys can be grown by alternating *Tb* and *Co* layer depositions, each layer being thin, typically 0.5nm , to obtain an amorphous alloy [84, 85] with good annealing endurance. The composition must be adjusted according to the annealing temperature and total thickness to compensate for *Tb* diffusion and oxidation. It is possible to obtain perpendicular anisotropy structures with high squareness hysteresis cycles and a coercivity $> 15\text{kOe}$ even after annealing at 300°C . These alloys are more suitable for reference electrodes since a total thickness $\geq 4\text{nm}$ is necessary to obtain perpendicular anisotropy after annealing. This thickness is too large for STT switching and the switching efficiency is expected to be impacted by a large damping associated with strong spin-orbit coupling in the presence of heavy terbium atoms. The *TbCo* composition was optimized for multilayer thicknesses of $(\text{Tb}0.45/\text{Co}0.55)_{\times 20}\text{nm}$. A low saturation magnetization of 100emu cm^{-3} and an effective anisotropy of $\approx 10^6\text{erg cm}^{-3}$, results in 100kOe anisotropy fields, that are hard to measure. Extrapolations from curves in a 20kOe limited range leads to anisotropy values of $1 - 4 \cdot 10^6\text{erg cm}^{-3}$. The integration of a *TbCo* electrode in tunnel junctions to stabilize a *CoFeB* top reference layer resulted in 80% TMR.

Co/Ni multilayers could also be used to achieve high perpendicular magnetic anisotropy electrodes. Unlike RE-TM alloys with poorer chemical stability due to the affinity of the RE elements to form oxygen bonds, *Co/Ni* multilayers could be used in direct interface with the tunnel barrier. However, the crystal symmetry problem of growing an *bcc* – *MgO* on top of the *fcc* – *Co/Ni* magnetic electrode with (111) orientation is the same existing for *Co/Pt* multilayers. Our original study did not address the required texture breaking layers, but looked at the possibility to have top and bottom magnetic electrodes based on *Co/Ni* multilayers [86]. The optimized perpendicular MTJ consisted of a bottom electrode $\text{Pt}20/(\text{Co}0.3/\text{Ni}0.4)_{\times 6}$, a 1.4nm *MgO* tunnel barrier, and $(\text{Co}0.3/\text{Ni}0.4)_{\times 3}/\text{Pt}3\text{nm}$ top electrode. The measured *Co/Ni* saturation magnetization was 670emu cm^{-3} , and the calculated M_s values of these thin *Co* and *Ni* layers are respectively 1060emu cm^{-3} and 280emu cm^{-3} , much smaller than the bulk material values. At the same time we can calculate the different contributions to the total perpendicular anisotropy energy from each interface. The surface anisotropy of the *Co/Ni* interface was $K_s^{\text{Co/Ni}} = 0.19\text{erg cm}^{-2}$, while the contribution of the *Pt/Co* interface in the same stack was much higher $K_s^{\text{Pt/Co}} = 0.88\text{erg cm}^{-2}$. It was possible for the tunnel junction top and bottom electrodes to have clearly different coercivities, 130 and 450Oe respectively. Recently other works [87] demonstrated bottom reference electrodes based on *Co/Ni* multilayers using a *NiCr* buffer to replace the *Pt* buffer and including our proposed *Ta* insertion as a texture breaking layer, to achieve a 165% TMR perpendicular magnetic tunnel junctions.

Ferromagnet/oxide interface anisotropy was shown to favor perpendicular alignment of the anisotropy direction. Early experiments at Spintec showed this phenomenon to be quite gen-

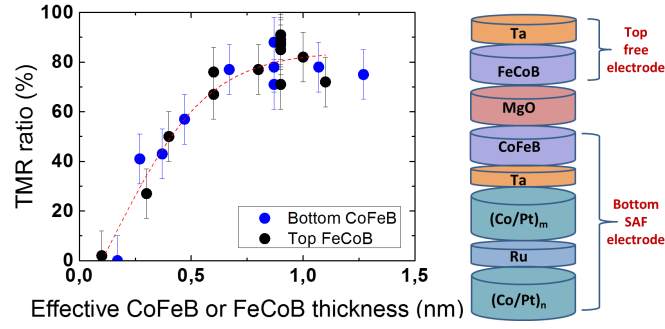


Figure 4.4 – Optimization top and bottom electrode thickness for high of TMR perpendicular MTJ. Top and bottom electrode effective thickness corrected for magnetic *dead layer*.

eral [88], observed for different magnetic transition metals and oxide layers. The perpendicular interface anisotropy of $CoFeB/MgO$ is large enough to stabilize the electrode once patterned [89], this even without the interface anisotropy contribution of a Pt buffer layer. To improve TMR of perpendicular anisotropic magnetic tunnel junctions, the thicknesses of the electrodes on both sides of the MgO tunnel barrier was optimized. We investigated the case of junctions having a Co/Pt multilayer reference electrode, coupled to the bottom $Co_{60}Fe_{20}B_{20}$ reference electrode through a Ta insertion. The top $Fe_{72}Co_{8}B_{20}$ free layer was deposited on the MgO barrier and capped by Ta . Both the top and bottom $CoFeB$ thicknesses were independently modified to evaluate the impact on anisotropy and TMR signal. Measuring the evolution of the magnetization as function of thickness, it was possible to estimate the magnetic *dead layer* of two electrodes. This *dead layer* thickness, below which the material becomes non-magnetic, forms at the $Ta - CoFeB$ interface due to intermixing and diffusion.

Measuring the TMR signal as a function of the effective thickness, shows the same tendency for both electrodes: an increase of TMR followed by saturation maximum value, with the same thickness dependence once the dead layer correction is include [90]. The observed increase and saturation can be interpreted as the thickness required to establish full spin polarization. From Jullière's model, a full spin polarization $\eta_{CoFeB/FeCoB} = 0.4$ is calculated for the reference and free layer electrodes. It can be assumed that the spin polarization depends exponentially on the electrode thickness, such that the electrode spin polarization P_1 is described as

$$P_1 = \eta \left[1 - \exp\left(-\frac{t}{l_c}\right) \right] \quad (4.9)$$

where η is the full spin polarization of the magnetic electrode material, t is the electrode thickness and l_c a characteristic length that defines the relative contribution of interface and bulk spin polarizations. We obtained a fitting value $l_c = 0.4nm$, corresponding to the red fit curve in Fig. 4.4. This short characteristic length l_c emphasizes the interfacial contribution in perpendicular anisotropy tunnel junctions, compared to in-plane junctions where a higher characteristic length $l_c = 0.8nm$ has been measured [91].

Double oxide interface is also a viable solution to increase the perpendicular anisotropy of the storage layer electrode. We demonstrated that the replacement of the Ta capping layer by a

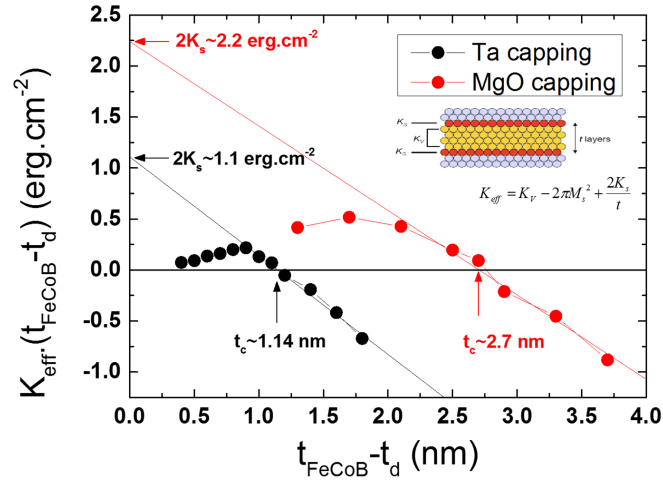


Figure 4.5 – Increasing the perpendicular anisotropy with second *MgO* oxide interface replacing a *Ta* capping layer.

second *MgO* barrier allows for a significant improvement of the perpendicular anisotropy. Using the convention that perpendicular anisotropy corresponds to a positive effective anisotropy K_{eff} , while negative values correspond to in-plane anisotropy, the effective anisotropy can be expressed as

$$K_{eff} = K_v - 2\pi M_s^2 + \frac{K_{s1} + K_{s2}}{t} \quad (4.10)$$

where K_v stands for the volume anisotropy, M_s the saturation magnetization, $K_{s1,s2}$ to the interfacial anisotropies of the bottom and top interfaces and t is the effective magnetic thickness. The increase of perpendicular anisotropy by the oxide capping layer is illustrated in Fig. 4.5 for the case of *MgO/FeCoB/Ta* compared to a composite storage layer *MgO/FeCoB / Ta 0.3nm / FeCoB/MgO*. Assuming that volume anisotropy energy is at least one order of magnitude smaller than the interface anisotropy values [89,92], the slope of the linear trend, corresponds to an M_s value of 1150emu cm^{-3} for the composite layer and 1240emu cm^{-3} for the *FeCoB* with *Ta* cap. The interface anisotropy is obtained from the $K_{eff}t$ intercept. For the *Ta* capped electrode $K_s = 1.1 \text{erg.cm}^{-2}$ and in the case of a double *MgO* interface we find a total interface anisotropy $2K_s = 2.2 \text{erg.cm}^{-2}$, that is twice the value of the single oxide interface and *Ta* capping. This result is particularly interesting for the scaling of the memory cell to smaller dimensions. Using these values to calculate the pillar diameter still maintaining a thermal stability factor $\Delta = K_{eff}/k_B T$ of 70, results in a minimum diameter of 19.6nm , assuming an electrode thickness $t = 1.5 \text{nm}$, $2K_s = 2.2 \text{erg.cm}^{-2}$ and $M_s = 1150 \text{emu cm}^{-3}$. Reducing further the minimum cell dimensions requires higher interface anisotropy values or reducing M_s , since smaller electrode thickness will result in lower TMR values. Setting the 14nm node as target, would require a 20% increase in K_s and reducing M_s by 20%, which seem reasonable values to be achieved from further stack optimizations. However, targeting the 10nm node does not seem feasible with present perpendicular interface anisotropy stacks, since the anisotropy from a single interface would have to be at least $K_s = 2 \text{erg.cm}^{-2}$.

4.2.4 Spin transfer torque switching

Evaluation of MRAM cell concepts requires the actual fabrication of individual test cells, independently of the chosen write method. Providing electrical demonstrations of a working concept was the main objective for the development of a nano-fabrication process allowing the realization of small size magnetic tunnel junction pillars. The chosen path was to use high aspect ratio *Ta* pillars, down to 20nm wide and 100 – 150nm thick, using anisotropic reactive ion etching (RIE). The initial RIE mask is defined by e-beam lithography using a PMMA (polymethyl methacrylate) resist lift-off to set the *Ta* pillar lateral shape and radius. After RIE, the *Ta* pillar serves as a hard mask to pattern the tunnel junction nanomagnet electrodes by ion-beam milling, and also as a contact to the top electrode. The large majority of the ‘proof-of-principle’ demonstrations of the investigated MRAM concepts used some iteration of this nano-fabrication process. The process presently provides the possibility to realize sub-30nm diameter MTJ elements and sub-20nm hard mask pillars.

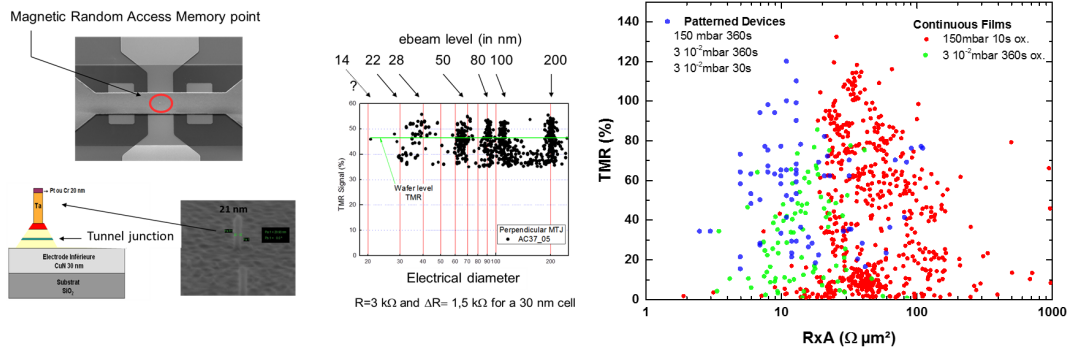


Figure 4.6 – (a) Scanning electron microscope images of MTJ cell geometry and *Ta* hard mask pillar. (b) Patterned tunnel junction TMR measurements at various cell sizes and reference wafer level TMR. (c) TMR and $R \times A$ product of perpendicular anisotropy tunnel junctions, from an ensemble of continuous film and patterned wafers fabricated for cell structure optimizations.

Optimization of TMR has already been alluded to. However, achieving $R \times A$ levels compatible with spin transfer torque and thermally assisted writing is equally important. This control is briefly illustrated in Fig. 4.6(c), where the *MgO* barrier fabricated by natural oxidation shows its sensitivity to the oxygen base pressure and oxidation time. The starting metallic *Mg* thickness also impacts $R \times A$, as well as the perpendicular anisotropy value. The level of $R \times A$ product together with the breakdown voltage V_b define the maximum levels of current density $j_{max} = V_b / (R \times A)$ and power density $p_{max} = V_b^2 / (R \times A)$ that are accessible during electrical tests. Applications of MRAM target low write voltage values of 0.5 – 1.5V. Within this range, significant MTJ cell heating requires typical power density values 10 – 30mW/μm² achievable with $R \times A = 20 - 40 \Omega \mu m^2$. For STT switching critical current densities in the $10^6 A/cm^2$ range, barriers of 5 – 15Ω μm² are needed. When combining both heating and STT effects, the relative importance of each contribution is critically defined by the $R \times A$ level.

4.2.5 Field-voltage phase diagrams

As mentioned in this chapter introduction, the characteristic boundaries of the field-voltage phase diagrams can be used to measure critical current density for STT switching in a cell, as well as providing estimations for material parameters. These field-voltage diagrams are obtained by measuring the cell resistance after applying a current/voltage pulse of 0.1 – 300ns width. Since the switching voltage is not being applied during the resistance measurement, the recorded diagrams do not present typical heating artifacts of quasi-static continuous current sweeps. They also provide the possibility to extrapolate the critical current density for switching, even in cases for which the switching voltage might be higher than the breakdown voltage.

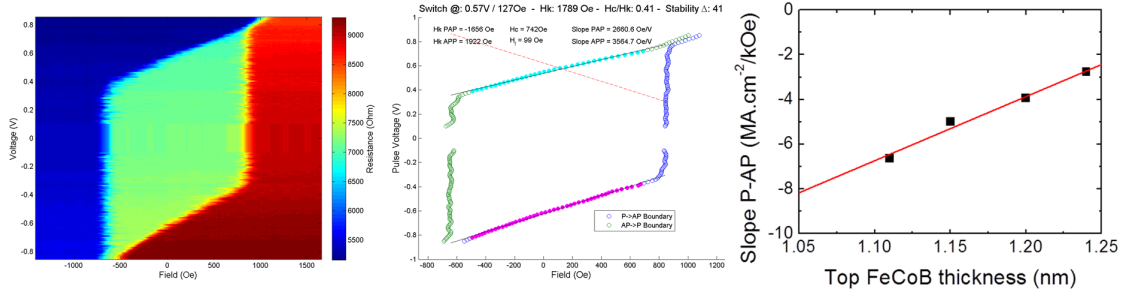


Figure 4.7 – (a) Field-voltage state phase diagram of a perpendicular anisotropy tunnel junction with resistance levels measured after pulse application, the green color represents a bi-stable region where writing is not possible. (b) Analysis of the phase diagram boundaries to extract critical switching voltage, boundary slopes and intercepts. (c) Evolution of the $P \rightarrow AP$ slope as function of $FeCoB$ free layer thickness to estimate the Gilbert damping parameter $\alpha = 0.016$.

This extrapolation is possible from equation 4.5 when the linear field-voltage boundary is revealed, i.e. the pulse voltage amplitude $V > s_t(\pm H_k \mp H_c)$, where s_t is the spin-torque efficiency pre-factor, directly determined from the experimental slope in Oe/V or $Oe/(Acm^{-2})$ units. A systematic study relating state phase diagrams parameter extractions and measurements of the same parameters from magnetic field measurements is still missing. Nevertheless, some initial results reported a storage layer anisotropy field $H_k = 2.8kOe$, that was within $\pm 10\%$ of the $H_k = 2.6kOe$ value obtained by saturating the free layer to an in-plane hard axis [73]. The obtained H_k values are in quite good agreement considering that they are derived from very different physical phenomena: super-paramagnetism and STT switching. In another example, discussed in reference [93], the variation of the field-current density slope was measured for different free layer thicknesses of the same $CoFeB$ electrode. The $P \rightarrow AP$ slope was used to estimate the Gilbert damping parameter. The slope can be expressed as

$$\frac{dj_c}{dH} = \frac{2e}{\hbar} \frac{\alpha}{\eta} \mu_0 M_s t \quad (4.11)$$

The value of the slope should vary linearly with thickness, its magnitude decreasing as the free layer thickness t is increased. This is exactly what was observed, as shown in Fig. 4.7(c). Using the measured value of $M_s = 1300emu/cm^3$ and a spin polarization constant $\eta = 0.3$ estimated from the TMR signal, numerical evaluation leads to a value of $\alpha = 0.016 \pm 0.004$, which is in good agreement with values reported by ferromagnetic resonance methods [94,95] on similar 1 nm thin

layers. These values are generally lower than other reports, which observed a significant increase of α for in-plane anisotropy layers as the thickness is reduced from 10 to 1.5nm [89].

4.3 Perpendicular anisotropy: thermally assisted writing

Similarly to in-plane anisotropy cells, it is also possible to use thermally assisted writing schemes in perpendicular anisotropy systems. One approach is to simply use the temperature dependence of the cell stability when writing. This thermal assistance is expected from the critical switching current dependence of the thermal stability ratio Δ , that is reduced with the increase of thermal energy $k_B T$. It is possible to observe the temperature dependence of the anisotropy in patterned cells, by measuring the coercive field H_c variation as function of temperature. The general trend appears to be linear from room temperature up to 100°C. This can be understood in the case of a thermally activated reversal model. From equation 4.12, we can write $H_c = H_k \left[1 - (k_B T / E_b)^{1/n} \right]$, including the measurement time correction factor in the value of the energy barrier E_b . Quasi-static coercivity measurements with a 1s measurement time require a value of $\Delta = E_b / (k_B T) > 23$, for the magnetization direction not to change during the measurement time, otherwise measured H_c will be zero. We can then write a phenomenological temperature dependence of H_c as:

$$H_c(T) = H_k \left[1 - \left(\frac{T}{T_b} \right)^{1/n} \right] \quad (4.12)$$

where T_b is a blocking temperature [96] defining the transition from ferromagnetic to superparamagnetic like behavior, and $n \in [1, 2]$ defines a magnetization reversal process. Assuming $n = 1$ we obtain a linear dependence of the coercivity with temperature, adding to the intrinsic anisotropy temperature dependence [97]. The behavior is illustrated in Figure 4.8(a), showing the coercivity H_c has a linear temperature dependence that can be extrapolated to define a blocking temperature at which the coercivity field is zero. This blocking temperature increases rapidly with *FeCoB* layer thickness. The data resolution does not allow to clearly estimate n from the temperature dependence. A value $n = 2$ leads to a dependence proportional to \sqrt{T} that would fit data just as well in the limited temperature range.

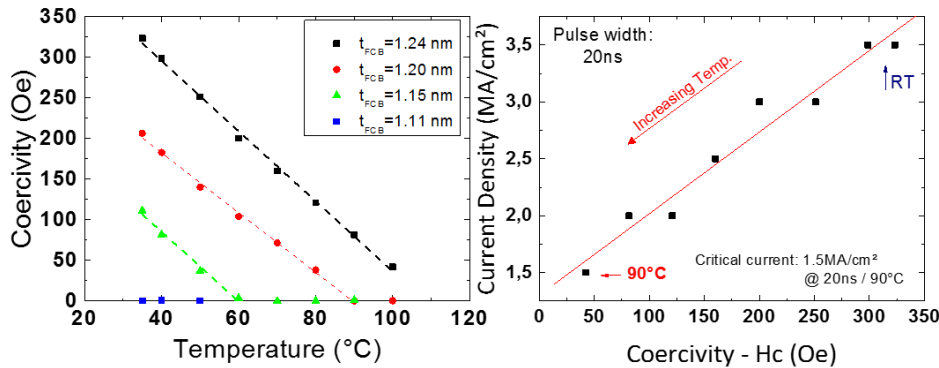


Figure 4.8 – (a) Temperature and linear dependence fits of coercive field in 100nm pillars for varying *FeCoB* top electrode thickness. (b) Reduction of the STT critical current by thermally assisted writing in *MgO/FeCoB/Ta* perpendicular interface anisotropy junctions.

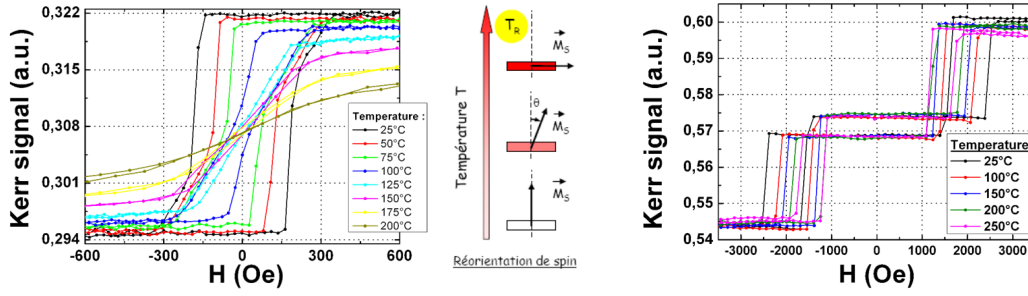
Using temperature to achieve a reduction in critical current density for switching is demonstrated in Figure 4.8(b). The critical current density j_c decreases linearly with the coercive field, resulting from the fact that both H_c and j_c depend linearly on the thermal stability factor Δ . This also explains why j_c is not zero at $H_c = 0$, since at the superparamagnetic limit, depending on the measurement integration time, $\Delta = 20 - 25$ but still not zero. The discussed results were obtained using the substrate holder as an external heating source, but using the self-heating of the cell by the STT current would proceed along the same reasoning. Any actual advantage of the thermally assisted writing represents a trade-off between lower absolute current and higher power density required for the self-heating. These results also show that writing can be optimized by adjusting write voltage levels to the actual device temperature. At the same time, they illustrate the importance of maintaining the level of thermal stability even at the highest temperature of the operating range.

4.3.1 Thermally induced spin reorientation

A more efficient way to exploit thermal assistance in materials with perpendicular magnetic anisotropy is to use more than a single perpendicular anisotropy interface using a multilayer structure. It can then provide very high stability at room temperature with a high temperature dependence to allow writing when heated [97,98]. The principle of this thermally assisted perpendicular anisotropy MRAM writing mode is to use magnetization reorientation with temperature. In materials with perpendicular magnetization, there exists a temperature where magnetization will tilt from perpendicular to in-plane, when the perpendicular anisotropy equals the in-plane anisotropy at an elevated temperature. It is possible to take advantage of this reorientation to decrease the STT critical switching current density. Writing will proceed in a sequence where a current heating pulse is applied, causing a temperature increase of the magnetic tunnel junction to around 150°C. At this temperature, the magnetization of the free layer gradually falls in the plane of the layer. Then the spin-polarized current will induce a precession of the in-plane anisotropy free layer around the perpendicular axis, with a net magnetization direction pointing upwards or downwards depending on the spin-polarized current direction. This situation corresponds to the highest spin transfer torque efficiency, because magnetization and polarization are in an orthogonal configuration. As the current decreases, the perpendicular anisotropy is recovered, stabilizing the storage layer direction upon cooling.

4.3.2 Perpendicular anisotropy temperature dependence

To validate this concept, we first developed a storage layer electrode that loses its perpendicular anisotropy in the 100-150°C temperature range. The hysteresis cycles of the $MgO/CoFeB1.5/Ta0.3/(Co0.2/Pd1.2)_{\times 5}/Pd2nm$ stack measured in perpendicular field by polar Kerr effect as a function of temperature are shown in Fig. 4.9(a). At room temperature the magnetization is perpendicular, the coercive field of the Co/Pd multilayer decreasing with temperature. From 125°C the measured cycles are characteristic of in-plane easy axis direction. The results discussed in reference [99] show that the reorientation temperature can be tuned by the multilayer Co thickness and number of repetitions. The decrease of Co thickness resulting in a rapid decrease of the magnetization with the temperature, associated with a lower Curie temperature, stabilizing above 0.4nm of cobalt.



(a) Illustration of the free layer magnetic reorientation as a function of temperature in a $Pt/Co/MgO$ stack. (b) Synthetic antiferromagnetic reference layer having stable orientation up to at least 250°C .

Figure 4.9 – Polar Kerr hysteresis loops of free and reference layers.

The reference electrode must keep its perpendicular magnetization at the writing temperature to maintain the perpendicular electron spin polarization. The reference layer stack $Pt5/(Co0.5/Pt0.4)_{\times 5}/Co0.5/Ru0.85/Pt0.2/(Co0.5/Pt0.4)_{\times 3}/CoFeB1.5nm$ has a stable perpendicular anisotropy direction up to 250°C . A reduction of the Ru antiferromagnetic coupling is observed, but the antiferromagnetic coupling is still maintained up to 1200Oe fields.

4.3.3 Thermally induced spin reorientation switching

For the actual demonstration of the proposed writing process tunnel junctions integrating the reference and storage layer were fabricated with an MgO barrier of $25\Omega \mu\text{m}^2$ patterned to 110nm diameter cells. The measured thermal stability ratio of this junction was $162k_B T$ at room temperature. The heating effect is clearly observed in the decrease of coercivity as the applied 30ns pulse voltage is increased from 0.4 to 1.1V bringing the coercivity from 1400Oe to under 100Oe . This drop is independent of the voltage polarity, but the current direction defines the final favored state, parallel P for negative voltage and antiparallel AP for positive voltage.

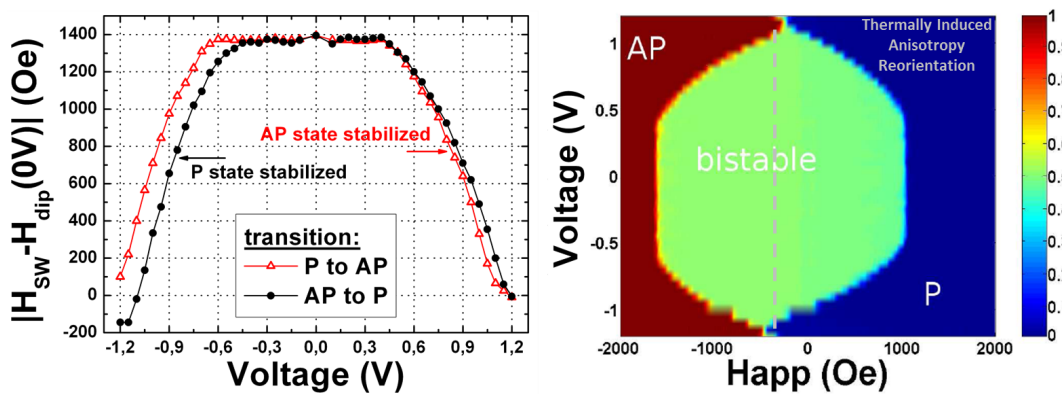
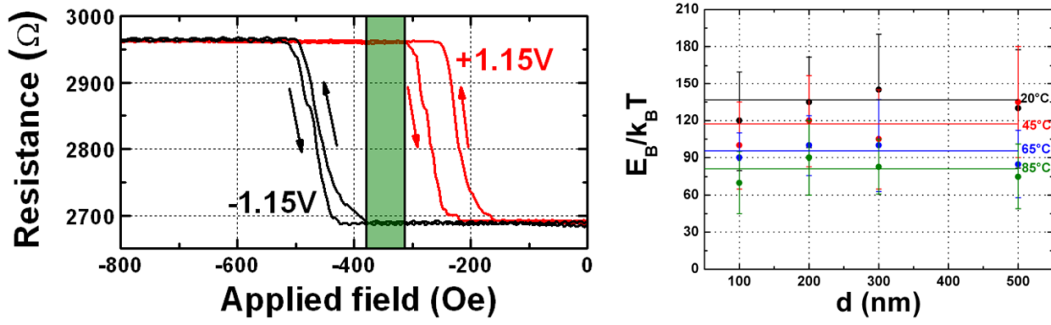


Figure 4.10 – (a) Switching fields as a function of applied pulse voltage in thermally induced reorientation switching. (b) Recorded state phase diagram using normalized resistance levels, the green region corresponding to the bi-stable region where both parallel and antiparallel states are possible.

This is confirmed by the obtained phase diagram, where it also becomes clear that the asymmetry induced by the STT current is small, resulting in a small write window around 1.15V .



(a) MRAM cell operating field window at $\pm 1.15V$ pulses for write pulse widths of $30ns$. (b) Thermal stability ratio Δ as function of temperature and pillar diameter.

Figure 4.11 – Demonstration of thermally induced reorientation switching MRAM cell.

Because of the cell high temperature at writing, the magnetization can fall back into the plane and emerge in either direction upon cooling. This can be controlled by adjusting the heating and STT current levels through the barrier $R \times A$ level. The write voltage window at $\pm 1.15V$ where magnetization direction is set by the voltage polarity corresponds to a current density $j_c = 4.6 \cdot 10^6 A/cm^2$ and a power density $p = 53mW/\mu m^2$, this window is shown more clearly in Fig. 4.11(a). This current density is comparable to that of conventional perpendicular anisotropy cells, despite the expected Gilbert damping $\alpha = 0.15$ of Co/Pd multilayers [100] being one order of magnitude higher than that of $Ta/CoFeB/MgO$. The TMR level of this demonstration cell was only 10% and higher TMR is expected to improve spin torque efficiency and write selectivity. We can calculate the figure of merit that is the ratio Δ/I_c , corresponding to an STT switching efficiency of $1.26k_B T/(\mu A)$. This was one of the highest reported at the time, showing the potential to achieve high stability MRAM writing at reduced current density levels. Optimizing the barrier $R \times A$, reducing the damping of the storage layer and using thermal barriers should further enhance the performance of this writing method.

4.4 Conclusion

Integration of perpendicular anisotropy materials in magnetic tunnel junctions has allowed to extend MRAM to cell diameters below $20nm$. Spin transfer torque reversal in the perpendicular anisotropy geometry is dominated by the damping-like term and is not impacted by a non-zero field-like torque term, which can cause back-hopping writing errors [101] for in-plane anisotropy cells. Field-voltage state phase diagrams show remarkable agreement with simple macrospin models of STT switching. Damping-like term values of several kOe/V result in a low switching voltage dispersion for the typical anisotropy field variations observed on patterned dots. Comparison with in-plane anisotropy cells is even more favorable considering the STT switching efficiency as the ratio of switching critical current and cell thermal stability, the two being directly proportional with no additional contribution from the demagnetizing field, as is the case for the in-plane cell geometry. It is possible to optimize integration of perpendicular anisotropy materials in a tunnel junction with insertion layers to achieve transitions from fcc to bcc crystal structures, that respectively optimize perpendicular anisotropy of the Co/Pt multilayers in the reference electrode and the TMR signal through spin symmetry filtering in the MgO barrier. Perpendicu-

lar anisotropy of $K_s = 1 \text{ erg.cm}^{-2}$ from a single FeCoB/MgO interface, will allow scaling of dual interface storage layers to a sub-20nm diameter. Further scaling will require cell stack improvements to meet 14nm targets and more radical changes at 10nm. Besides high anisotropy, materials will also require low damping values to maintain a low write voltage, which is the reason currently preventing the use of Co/Pt multilayers to add more perpendicular anisotropy interfaces to the storage layer. A thermally assisted writing scheme can also be applied to perpendicular anisotropy cells. At a blocking temperature T_b , defined by the volume and effective anisotropy, the storage layer nanomagnet will behave like superparamagnetic particle along the perpendicular direction. The demagnetizing field will re-orient the easy axis direction in the plane close to this temperature, such that a lower STT current can be used to favor up or down perpendicular re-orientation upon cooling. This approach allows to combine high thermal stability in the operating temperature range and low write currents, leading to large Δ/I_c STT efficiency. From an energy point of view, the total power required for the temperature increase has to be considered, however taking temperature into account is a necessary step for optimized cell writing.

Bibliography

- [1] Myoung-Jae Lee, Seungwu Han, Sang Ho Jeon, Bae Ho Park, Bo Soo Kang, Seung-Eon Ahn, Ki Hwan Kim, Chang Bum Lee, Chang Jung Kim, In-Kyeong Yoo, David H. Seo, Xiang-Shu Li, Jong-Bong Park, Jung-Hyun Lee, and Youngsoo Park. Electrical Manipulation of Nanofilaments in Transition-Metal Oxides for Resistance-Based Memory. *Nano Lett.*, 9(4):1476–1481, April 2009.
- [2] Akihito Sawa. Resistive switching in transition metal oxides. *Materials today*, 11(6):28–36, 2008.
- [3] G. Servalli. A 45nm generation Phase Change Memory technology. In *2009 IEEE International Electron Devices Meeting (IEDM)*, pages 1–4, December 2009.
- [4] Rainer Waser, Regina Dittmann, Georgi Staikov, and Kristof Szot. Redox-Based Resistive Switching Memories and Nanoionic Mechanisms, Prospects, and Challenges. *Adv. Mater.*, 21(25-26):2632–2663, July 2009.
- [5] B. N. Engel, J. Akerman, B. Butcher, R. W. Dave, M. DeHerrera, M. Durlam, G. Grynkewich, J. Janesky, S. V. Pietambaram, N. D. Rizzo, J. M. Slaughter, K. Smith, J. J. Sun, and S. Tehrani. A 4-Mb toggle MRAM based on a novel bit and switching method. *IEEE Transactions on Magnetism*, 41(1):132–136, January 2005.
- [6] H.-S. Philip Wong and Sayeef Salahuddin. Memory leads the way to better computing. *Nat Nano*, 10(3):191–194, March 2015.
- [7] Yole Développement. Emerging non-volatile memory 2016 report, July 2016. http://www.yole.fr/Emerging_NVM_Market.aspx#.WI75N1MX3Po.
- [8] S.H. Kang and K. Lee. Emerging materials and devices in spintronic integrated circuits for energy-smart mobile computing and connectivity. *Acta Materialia*, 61(3):952–973, February 2013.
- [9] Luc Thomas, Guenole Jan, Jian Zhu, Huanlong Liu, Yuan-Jen Lee, Son Le, Ru-Ying Tong, Keyu Pi, Yu-Jen Wang, Dongna Shen, Renren He, Jesmin Haq, Jeffrey Teng, Vinh Lam, Kenlin Huang, Tom Zhong, Terry Torng, and Po-Kang Wang. Perpendicular spin transfer torque magnetic random access memories with high spin torque efficiency and thermal stability for embedded applications (invited). *Journal of Applied Physics*, 115(17):172615, May 2014.

- [10] J.C. Slonczewski. Current-driven excitation of magnetic multilayers. *Journal of Magnetism and Magnetic Materials*, 159(12):L1–L7, 1996.
- [11] L. Berger. Emission of spin waves by a magnetic multilayer traversed by a current. *Physical Review B*, 54(13):9353, 1996.
- [12] J. A. Katine, F. J. Albert, R. A. Buhrman, E. B. Myers, and D. C. Ralph. Current-Driven Magnetization Reversal and Spin-Wave Excitations in Co/Cu/Co Pillars. *Phys. Rev. Lett.*, 84(14):3149–3152, April 2000.
- [13] M. Julliere. Tunneling between ferromagnetic films. *Physics Letters A*, 54(3):225–226, September 1975.
- [14] J. Z. Sun. Spin-current interaction with a monodomain magnetic body: A model study. *Physical Review B*, 62(1):570, 2000.
- [15] Ralph Skomski, G. C. Hadjipanayis, and D. J. Sellmyer. Effective Demagnetizing Factors of Complicated Particle Mixtures. *IEEE Transactions on Magnetism*, 43(6):2956–2958, June 2007.
- [16] Tetsuya Yamamoto, Hiroshi Kano, Yutaka Higo, Kazuhiro Ohba, Tetsuya Mizuguchi, Masanori Hosomi, Kazuhiro Bessho, Minoru Hashimoto, Hiroyuki Ohmori, Takeyuki Sone, Keitaro Endo, Shinya Kubo, Hiroaki Narisawa, Wataru Otsuka, Nobumichi Okazaki, Makoto Motoyoshi, Hajime Nagao, and Tsutomu Sagara. Magnetoresistive random access memory operation error by thermally activated reversal (invited). *Journal of Applied Physics*, 97(10):10P503, May 2005.
- [17] Leonid Savtchenko, Bradley N Engel, Nicholas D Rizzo, Mark F Deherrera, and Jason Allen Janesky. Method of writing to scalable magnetoresistance random access memory element. US Patent 6,545,906, April 8 2003.
- [18] I. L. Prejbeanu, W. Kula, K. Ounadjela, R. C. Sousa, O. Redon, B. Dieny, and J. P. Nozïeres. Thermally assisted switching in exchange-biased storage layer magnetic tunnel junctions. *IEEE Transactions on Magnetism*, 40(4):2625–2627, July 2004.
- [19] E. Gapihan, R. C. Sousa, J. Hérault, C. Papusoi, M. T. Delaye, B. Dieny, I. L. Prejbeanu, C. Ducruet, C. Portemont, K. Mackay, and J. P. Nozïeres. FeMn Exchange Biased Storage Layer for Thermally Assisted MRAM. *IEEE Transactions on Magnetism*, 46(6):2486–2488, June 2010.
- [20] V. Baltz, J. Sort, B. Rodmacq, B. Dieny, and S. Landis. Thermal activation effects on the exchange bias in ferromagnetic-antiferromagnetic nanostructures. *Physical Review B*, 72(10), September 2005.
- [21] G. Vallejo-Fernandez and J. N. Chapman. Size effects in submicron exchange bias square elements. *Applied Physics Letters*, 94(26):262508, June 2009.
- [22] M. Kerekes, R. C. Sousa, I. L. Prejbeanu, O. Redon, U. Ebels, C. Baraduc, B. Dieny, J.-P. Nozïeres, P. P. Freitas, and P. Xavier. Dynamic heating in submicron size magnetic tunnel junctions with exchange biased storage layer. *Journal of Applied Physics*, 97(10):10P501, May 2005.

- [23] W. Oepts, H. J. Verhagen, W. J. M. de Jonge, and R. Coehoorn. Dielectric breakdown of ferromagnetic tunnel junctions. *Applied Physics Letters*, 73(16):2363–2365, October 1998.
- [24] Jianguo Wang and P. P. Freitas. Low-current blocking temperature writing of double barrier magnetic random access memory cells. *Applied Physics Letters*, 84(6):945–947, February 2004.
- [25] R. C. Sousa, M. Kerekes, I. L. Prejbeanu, O. Redon, B. Dieny, J. P. Nozières, and P. P. Freitas. Crossover in heating regimes of thermally assisted magnetic memories. *Journal of Applied Physics*, 99(8):08N904, April 2006.
- [26] William Brown. Thermal Fluctuations of a Single-Domain Particle. *Physical Review*, 130(5):1677–1686, June 1963.
- [27] E. Fulcomer and S. H. Charap. Thermal fluctuation aftereffect model for some systems with ferromagnetic and antiferromagnetic coupling. *Journal of Applied Physics*, 43(10):4190–4199, October 1972.
- [28] L. Lombard, E. Gapihan, R. C. Sousa, Y. Dahmane, Y. Conraux, C. Portemont, C. Ducruet, C. Papiusoi, I. L. Prejbeanu, J. P. Nozières, B. Dieny, and A. Schuhl. IrMn and FeMn blocking temperature dependence on heating pulse width. *Journal of Applied Physics*, 107(9):09D728, 2010.
- [29] R. H. Koch, J. A. Katine, and J. Z. Sun. Time-Resolved Reversal of Spin-Transfer Switching in a Nanomagnet. *Physical Review Letters*, 92(8), February 2004.
- [30] D. Bedau, H. Liu, J. Z. Sun, J. A. Katine, E. E. Fullerton, S. Mangin, and A. D. Kent. Spin-transfer pulse switching: From the dynamic to the thermally activated regime. *Applied Physics Letters*, 97(26):262502, 2010.
- [31] M. P. Sharrock. Time dependence of switching fields in magnetic recording media (invited). *Journal of Applied Physics*, 76(10):6413, 1994.
- [32] V. Giraud, J. Cluzel, V. Sousa, A. Jacquot, A. Dauscher, B. Lenoir, H. Scherrer, and S. Romer. Thermal characterization and analysis of phase change random access memory. *Journal of Applied Physics*, 98(1):013520, July 2005.
- [33] S. Cardoso, R. Ferreira, F. Silva, P. P. Freitas, L. V. Melo, R. C. Sousa, O. Redon, M. MacKenzie, and J. N. Chapman. Double-barrier magnetic tunnel junctions with GeSbTe thermal barriers for improved thermally assisted magnetoresistive random access memory cells. *Journal of Applied Physics*, 99(8):08N901, April 2006.
- [34] C. Papiusoi, R. Sousa, J. Hérault, I. L. Prejbeanu, and B. Dieny. Probing fast heating in magnetic tunnel junction structures with exchange bias. *New J. Phys.*, 10(10):103006, 2008.
- [35] P. Bruno. Theory of interlayer magnetic coupling. *Phys. Rev. B*, 52:411–439, Jul 1995.
- [36] D. C. Worledge. Spin flop switching for magnetic random access memory. *Applied Physics Letters*, 84(22):4559, 2004.

- [37] A. Chavent, C. Ducruet, C. Portemont, C. Creuzet, L. Vila, J. Alvarez-Hérault, R. C. Sousa, I. L. Prejbeanu, and B. Dieny. Controlled pulse shape cooling in planar TAS-STT-MRAM for improved writeability. In *2015 IEEE Magnetics Conference (INTERMAG)*, pages 1–1, May 2015.
- [38] J. Hayakawa, S. Ikeda, K. Miura, M. Yamanouchi, Y. M. Lee, R. Sasaki, M. Ichimura, K. Ito, T. Kawahara, R. Takemura, T. Meguro, F. Matsukura, H. Takahashi, H. Matsuoka, and H. Ohno. Current-Induced Magnetization Switching in MgO Barrier Magnetic Tunnel Junctions With CoFeB-Based Synthetic Ferrimagnetic Free Layers. *IEEE Transactions on Magnetics*, 44(7):1962–1967, July 2008.
- [39] Z. Li and S. Zhang. Thermally assisted magnetization reversal in the presence of a spin-transfer torque. *Physical Review B*, 69(13), April 2004.
- [40] Charles Kittel. On the theory of ferromagnetic resonance absorption. *Phys. Rev.*, 73:155–161, Jan 1948.
- [41] C. H. Back, D. Weller, J. Heidmann, D. Mauri, D. Guarisco, E. L. Garwin, and H. C. Siegmann. Magnetization reversal in ultrashort magnetic field pulses. *Physical Review Letters*, 81(15):3251, 1998.
- [42] Martin Bauer, Jörg Fassbender, Burkard Hillebrands, and R. L. Stamps. Switching behavior of a Stoner particle beyond the relaxation time limit. *Physical Review B*, 61(5):3410, 2000.
- [43] H. W. Schumacher, C. Chappert, P. Crozat, R. C. Sousa, P. P. Freitas, J. Miltat, J. Fassbender, and B. Hillebrands. Phase Coherent Precessional Magnetization Reversal in Microscopic Spin Valve Elements. *Phys. Rev. Lett.*, 90(1):017201, January 2003.
- [44] H. W. Schumacher, C. Chappert, R. C. Sousa, P. P. Freitas, and J. Miltat. Quasiballistic Magnetization Reversal. *Phys. Rev. Lett.*, 90(1):017204, January 2003.
- [45] A. D. Kent, B. Özyilmaz, and E. del Barco. Spin-transfer-induced precessional magnetization reversal. *Appl. Phys. Lett.*, 84(19):3897–3899, April 2004.
- [46] T. Devolder, J. Hayakawa, K. Ito, H. Takahashi, S. Ikeda, P. Crozat, N. Zerounian, Joo-Von Kim, C. Chappert, and H. Ohno. Single-Shot Time-Resolved Measurements of Nanosecond-Scale Spin-Transfer Induced Switching: Stochastic Versus Deterministic Aspects. *Physical Review Letters*, 100(5), February 2008.
- [47] S. Wiebel, J.-P. Jamet, N. Vernier, A. Mougin, J. FerrÀ©, V. Baltz, B. Rodmacq, and B. Dieny. Domain decoration in dipolar coupled ferromagnetic stacks with perpendicular anisotropy. *Applied Physics Letters*, 86(14):142502, April 2005.
- [48] Bernard Rodmacq, Vincent Baltz, and Bernard Dieny. Macroscopic probing of domain configurations in interacting bilayers with perpendicular magnetic anisotropy. *Physical Review B*, 73(9), March 2006.
- [49] S. Yuasa and D. D. Djayaprawira. Giant tunnel magnetoresistance in magnetic tunnel junctions with a crystalline MgO(0 0 1) barrier. *J. Phys. D: Appl. Phys.*, 40(21):R337, 2007.

- [50] M. T. Johnson, P. J. H. Bloemen, F. J. A. den Broeder, and J. J. de Vries. Magnetic anisotropy in metallic multilayers. *Rep. Prog. Phys.*, 59(11):1409, 1996.
- [51] S. Bandiera, R. C. Sousa, B. Rodmacq, and B. Dieny. Asymmetric Interfacial Perpendicular Magnetic Anisotropy in Pt/Co/Pt Trilayers. *IEEE Magnetics Letters*, 2:3000504–3000504, 2011.
- [52] S. Bandiera, R. C. Sousa, B. Rodmacq, L. Lechevallier, and B. Dieny. Effect of a Cu spacer between Co and Pt layers on the structural and magnetic properties in (Co/Cu/Pt) 5 /Pt type multilayers. *J. Phys. D: Appl. Phys.*, 46(48):485003, 2013.
- [53] A. Vaysset, C. Papusoi, L. D. Buda-Prejbeanu, S. Bandiera, M. Marins de Castro, Y. Dahmane, J.-C. Toussaint, U. Ebels, S. Auffret, R. Sousa, L. Vila, and B. Dieny. Improved coherence of ultrafast spin-transfer-driven precessional switching with synthetic antiferromagnet perpendicular polarizer. *Applied Physics Letters*, 98(24):242511, June 2011.
- [54] S. Bandiera, R. C. Sousa, Y. Dahmane, C. Ducruet, C. Portemont, V. Baltz, S. Auffret, I. L. Prejbeanu, and B. Dieny. Comparison of Synthetic Antiferromagnets and Hard Ferromagnets as Reference Layer in Magnetic Tunnel Junctions With Perpendicular Magnetic Anisotropy. *IEEE Magnetics Letters*, 1:3000204–3000204, 2010.
- [55] M. Marins de Castro, R. C. Sousa, S. Bandiera, C. Ducruet, A. Chavent, S. Auffret, C. Papusoi, I. L. Prejbeanu, C. Portemont, L. Vila, U. Ebels, B. Rodmacq, and B. Dieny. Precessional spin-transfer switching in a magnetic tunnel junction with a synthetic antiferromagnetic perpendicular polarizer. *Journal of Applied Physics*, 111(7):07C912, April 2012.
- [56] K. J. Lee, O. Redon, and B. Dieny. Analytical investigation of spin-transfer dynamics using a perpendicular-to-plane polarizer. *Appl. Phys. Lett.*, 86(2):022505, January 2005.
- [57] Kyung-Jin Lee, Alina Deac, Olivier Redon, Jean-Pierre Nozieres, and Bernard Dieny. Excitations of incoherent spin-waves due to spin-transfer torque. *Nat Mater*, 3(12):877–881, December 2004.
- [58] U. Ebels, D. Houssameddine, I. Firastrau, D. Gusakova, C. Thirion, B. Dieny, and L. D. Buda-Prejbeanu. Macrospin description of the perpendicular polarizer-planar free-layer spin-torque oscillator. *Physical Review B*, 78(2), July 2008.
- [59] B. Lacoste, M. Marins de Castro, T. Devolder, R. C. Sousa, L. D. Buda-Prejbeanu, S. Auffret, U. Ebels, C. Ducruet, I. L. Prejbeanu, L. Vila, B. Rodmacq, and B. Dieny. Modulating spin transfer torque switching dynamics with two orthogonal spin-polarizers by varying the cell aspect ratio. *Phys. Rev. B*, 90(22):224404, December 2014.
- [60] J. Das, R. Degraeve, H. Boeve, L. Lagae, G. Groeseneken, G. Borghs, and J. de Broek. Tunnel barrier properties of stressed ferromagnetic tunnel junctions. *Electronics Letters*, 37(6):356–358, March 2001.
- [61] Antoine Demolliens. *Transmission electron microscopy contribution to the examination of non volatile emergent memories*. Theses, Université du Sud Toulon Var, December 2009.

- [62] Keiji Hosotani, Makoto Nagamine, Tomomasa Ueda, Hisanori Aikawa, Sumio Ikegawa, Yoshiaki Asao, Hiroaki Yoda, and Akihiro Nitayama. Effect of Self-Heating on Time-Dependent Dielectric Breakdown in Ultrathin MgO Magnetic Tunnel Junctions for Spin Torque Transfer Switching Magnetic Random Access Memory. *Japanese Journal of Applied Physics*, 49(4):04DD15, April 2010.
- [63] Lorène Courtade. *Développement, mécanismes de programmation et fiabilité de mémoires non volatiles à commutation de résistance MRAM et OxRRAM*. PhD thesis, Université du Sud Toulon Var, 2009.
- [64] J. Akerman, P. Brown, M. DeHerrera, M. Durlam, E. Fuchs, D. Gajewski, M. Griswold, J. Janesky, J. J. Nahas, and S. Tehrani. Demonstrated reliability of 4-mb MRAM. *IEEE Transactions on Device and Materials Reliability*, 4(3):428–435, September 2004.
- [65] R. Moazzami, J. C. Lee, and C. Hu. Temperature acceleration of time-dependent dielectric breakdown. *IEEE Transactions on Electron Devices*, 36(11):2462–2465, November 1989.
- [66] J. Hérault, R. C. Sousa, C. Papusoi, Y. Conraux, C. Maunoury, I. L. Prejbeanu, K. Mackay, B. Delaet, J. P. Nozieres, and B. Dieny. Pulsewidth Dependence of Barrier Breakdown in MgO Magnetic Tunnel Junctions. *IEEE Transactions on Magnetics*, 44(11):2581–2584, November 2008.
- [67] D. Herranz, F. Bonell, A. Gomez-Ibarlucea, S. Andrieu, F. Montaigne, R. Villar, C. Tiusan, and F. G. Aliev. Strongly suppressed $1/f$ noise and enhanced magnetoresistance in epitaxial Fe-V/MgO/Fe magnetic tunnel junctions. *Applied Physics Letters*, 96(20):202501, May 2010.
- [68] H. Polovy, R. Guerrero, J. Scola, M. Pannetier-Lecoeur, C. Fermon, G. Feng, K. Fahy, S. Cardoso, J. Almeida, and P. P. Freitas. Noise of MgO-based magnetic tunnel junctions. *Journal of Magnetism and Magnetic Materials*, 322(9–12):1624–1627, May 2010.
- [69] S. Amara-Dababi, H. Béa, R. C. Sousa, C. Baraduc, and B. Dieny. Correlation between write endurance and electrical low frequency noise in MgO based magnetic tunnel junctions. *Applied Physics Letters*, 102(5):052404, February 2013.
- [70] Thibaut Devolder. Scalability of Magnetic Random Access Memories Based on an In-Plane Magnetized Free Layer. *Applied Physics Express*, 4(9):093001, August 2011.
- [71] S. Mangin, D. Ravelosona, J. A. Katine, M. J. Carey, B. D. Terris, and Eric E. Fullerton. Current-induced magnetization reversal in nanopillars with perpendicular anisotropy. *Nature Materials*, 5(3):210–215, March 2006.
- [72] K. Bernert, V. Sluka, C. Fowley, J. Lindner, J. Fassbender, and A. M. Deac. Phase diagrams of MgO magnetic tunnel junctions including the perpendicular spin-transfer torque in different geometries. *Physical Review B*, 89(13), April 2014.
- [73] A. A. Timopheev, R. Sousa, M. Chshiev, L. D. Buda-Prejbeanu, and B. Dieny. Respective influence of in-plane and out-of-plane spin-transfer torques in magnetization switching of perpendicular magnetic tunnel junctions. *Phys. Rev. B*, 92(10):104430, September 2015.

- [74] W. Wernsdorfer, E. Bonet Orozco, K. Hasselbach, A. Benoit, B. Barbara, N. Demoncy, A. Loiseau, H. Pascard, and D. Mailly. Experimental evidence of the Néel-Brown model of magnetization reversal. *Physical Review Letters*, 78(9):1791, 1997.
- [75] I. N. Krivorotov, N. C. Emley, A. G. F. Garcia, J. C. Sankey, S. I. Kiselev, D. C. Ralph, and R. A. Buhrman. Temperature Dependence of Spin-Transfer-Induced Switching of Nanomagnets. *Physical Review Letters*, 93(16), October 2004.
- [76] Yiming Huai, M. Pakala, Zhitao Diao, and Yunfei Ding. Spin-transfer switching current distribution and reduction in magnetic tunneling junction-based structures. *IEEE Transactions on Magnetics*, 41(10):2621–2626, October 2005.
- [77] Y. Higo, K. Yamane, K. Ohba, H. Narisawa, K. Bessho, M. Hosomi, and H. Kano. Thermal activation effect on spin transfer switching in magnetic tunnel junctions. *Applied Physics Letters*, 87(8):082502, August 2005.
- [78] R. Heindl, W. H. Rippard, S. E. Russek, M. R. Pufall, and A. B. Kos. Validity of the thermal activation model for spin-transfer torque switching in magnetic tunnel junctions. *Journal of Applied Physics*, 109(7):073910, 2011.
- [79] Xuebing Feng and P. B. Visscher. Sweep-rate-dependent coercivity simulation of fept particle arrays. *Journal of Applied Physics*, 95(11):7043–7045, 2004.
- [80] S. Ikeda, J. Hayakawa, Y. M. Lee, F. Matsukura, Y. Ohno, T. Hanyu, and H. Ohno. Magnetic Tunnel Junctions for Spintronic Memories and Beyond. *IEEE Transactions on Electron Devices*, 54(5):991–1002, May 2007.
- [81] Shinji Yuasa, Taro Nagahama, Akio Fukushima, Yoshishige Suzuki, and Koji Ando. Giant room-temperature magnetoresistance in single-crystal Fe/MgO/Fe magnetic tunnel junctions. *Nat Mater*, 3(12):868–871, December 2004.
- [82] Stuart S. P. Parkin, Christian Kaiser, Alex Panchula, Philip M. Rice, Brian Hughes, Mahesh Samant, and See-Hun Yang. Giant tunnelling magnetoresistance at room temperature with MgO (100) tunnel barriers. *Nat Mater*, 3(12):862–867, December 2004.
- [83] Léa Cuchet, Bernard Rodmacq, Stéphane Auffret, Ricardo C. Sousa, Clarisse Ducruet, and Bernard Dieny. Influence of a Ta spacer on the magnetic and transport properties of perpendicular magnetic tunnel junctions. *Applied Physics Letters*, 103(5):052402, 2013.
- [84] C. Bordel, S. Pizzini, J. Vogel, K. Mackay, J. Voiron, R. M. Galera, A. Fontaine, P. Auric, J. B. Goedkoop, and N. B. Brookes. Microscopic origin of the macroscopic magnetic properties of TbFeCoN amorphous thin films. *Physical Review B*, 56(13):8149, 1997.
- [85] T. Ueno, N. Inami, R. Sagayama, Z. Wen, M. Hayashi, S. Mitani, R. Kumai, and K. Ono. Relation between electronic structure and magnetic anisotropy in amorphous TbCo films probed by x-ray magnetic circular dichroism. *J. Phys. D: Appl. Phys.*, 49(20):205001, 2016.
- [86] L. You, R. C. Sousa, S. Bandiera, B. Rodmacq, and B. Dieny. Co/Ni multilayers with perpendicular anisotropy for spintronic device applications. *Applied Physics Letters*, 100(17):172411, 2012.

- [87] G. S. Kar, W. Kim, T. Tahmasebi, J. Swerts, S. Mertens, N. Heylen, and T. Min. Co/Ni based p-MTJ stack for sub-20nm high density stand alone and high performance embedded memory application. In *2014 IEEE International Electron Devices Meeting*, pages 19.1.1–19.1.4, December 2014.
- [88] S. Monso, B. Rodmacq, S. Auffret, G. Casali, F. Fettar, B. Gilles, B. Dieny, and P. Boyer. Crossover from in-plane to perpendicular anisotropy in Pt/CoFe/AlOx sandwiches as a function of Al oxidation: A very accurate control of the oxidation of tunnel barriers. *Applied Physics Letters*, 80(22):4157–4159, June 2002.
- [89] S. Ikeda, K. Miura, H. Yamamoto, K. Mizunuma, H. D. Gan, M. Endo, S. Kanai, J. Hayakawa, F. Matsukura, and H. Ohno. A perpendicular anisotropy CoFeB/MgO magnetic tunnel junction. *Nat Mater*, 9(9):721–724, September 2010.
- [90] Léa Cuchet, Bernard Rodmacq, Stéphane Auffret, Ricardo C. Sousa, and Bernard Dieny. Influence of magnetic electrodes thicknesses on the transport properties of magnetic tunnel junctions with perpendicular anisotropy. *Applied Physics Letters*, 105(5):052408, August 2014.
- [91] X. H. Xiang, T. Zhu, Z. P. Zhang, T. P. Beebe, and John Q. Xiao. Bulk contribution to magneto-resistance In Co-based magnetic tunnel junction. *Journal of Magnetism and Magnetic Materials*, 272-276, Part 3:1818–1820, May 2004.
- [92] T. Liu, J. W. Cai, and Li Sun. Large enhanced perpendicular magnetic anisotropy in CoFeB/MgO system with the typical Ta buffer replaced by an Hf layer. *AIP Advances*, 2(3):032151, 2012.
- [93] L. Cuchet, R. C. Sousa, L. Vila, S. Auffret, B. Rodmacq, and B. Dieny. Field Dependence of Spin-Transfer Torque Switching Current in Perpendicular Magnetic Tunnel Junctions. *IEEE Transactions on Magnetics*, 50(11):1–4, November 2014.
- [94] T. Devolder, P.-H. Ducrot, J.-P. Adam, I. Barisic, N. Vernier, Joo-Von Kim, B. Ockert, and D. Ravelosona. Damping of $\text{Co}_x\text{Fe}_{80-x}\text{B}_{20}$ ultrathin films with perpendicular magnetic anisotropy. *Applied Physics Letters*, 102(2):022407, 2013.
- [95] T. Devolder, T. Tahmasebi, S. Eimer, T. Hauet, and S. Andrieu. Compositional dependence of the magnetic properties of epitaxial FeV/MgO thin films. *Applied Physics Letters*, 103(24):242410, 2013.
- [96] Olivier Fruchart and André Thiaville. Magnetism in reduced dimensions. *Comptes Rendus Physique*, 6(9):921–933, November 2005.
- [97] M. Farle, W. Platow, A. N. Anisimov, B. Schulz, and K. Baberschke. The temperature dependence of magnetic anisotropy in ultra-thin films. *Journal of Magnetism and Magnetic Materials*, 165(1):74–77, January 1997.
- [98] R. Skomski, O. N. Mryasov, J. Zhou, and D. J. Sellmyer. Finite-temperature anisotropy of magnetic alloys. *Journal of Applied Physics*, 99(8):08E916, April 2006.

- [99] S. Bandiera, R. C. Sousa, M. Marins de Castro, C. Ducruet, C. Portemont, S. Auffret, L. Vila, I. L. Prejbeanu, B. Rodmacq, and B. Dieny. Spin transfer torque switching assisted by thermally induced anisotropy reorientation in perpendicular magnetic tunnel junctions. *Applied Physics Letters*, 99(20):202507, November 2011.
- [100] E. P. Sajitha, J. Walowski, D. Watanabe, S. Mizukami, F. Wu, H. Naganuma, M. Oogane, Y. Ando, and T. Miyazaki. Magnetization Dynamics in CoFeB Buffered Perpendicularly Magnetized Co/Pd Multilayer. *IEEE Transactions on Magnetism*, 46(6):2056–2059, June 2010.
- [101] J. Z. Sun, M. C. Gaidis, G. Hu, E. J. OSullivan, S. L. Brown, J. J. Nowak, P. L. Trouilloud, and D. C. Worledge. High-bias backhopping in nanosecond time-domain spin-torque switches of MgO-based magnetic tunnel junctions. *Journal of Applied Physics*, 105(7):07D109, 2009.
- [102] ITRS, the international technology roadmap for semiconductors, December 2010. http://www.itrs.net/Links/2010ITRS/2010Update/ToPost/2010_Update_Overview.pdf.